Stability Analysis of a Large Span Timber Dome

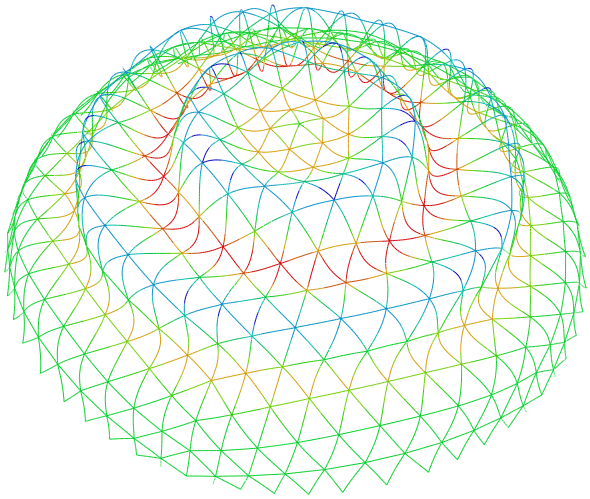

Gustav Fredriksson and Markus Herrström

Division of Structural Engineering
Faculty of Engineering, LTH
Lund University, 2017

Avdelningen för Konstruktionsteknik
Lunds Tekniska Högskola
221 00 LUND

Department of Structural Engineering
Faculty of Engineering LTH
Box 118
S-221 00 LUND
Sweden

Stability Analysis of a Large Span Timber Dome

Stabilitetsanalys av en träkupol

Master's dissertation by
Gustav Fredriksson and Markus Herrström
2017

supervised by

Roberto Crocetti
Professor at Division of Structural Engineering
Lund University

Silas Nørager
Senior Civil Engineer
Ove Arup & Partners Danmark A/S

Rapport TVBK-5258
ISSN 0349-4969
ISRN: LUTVDG/TVBK-17/5258+122p

Abstract

The aim of this thesis is to study the feasibility of building a timber dome with a span of 300 metres, concerning elastic stability. The load-bearing members were modelled with the properties of glued laminated timber GL30c with the dimensions 0.8×1.6 m^2. The design loads were 2 kN/m^2 and 4 kN/m^2 in symmetrical and asymmetrical load cases, respectively. The numerical calculations were performed using the software Abaqus FEA, and compared with analytical equations, modified using empirical data.

There are many ways to arrange the surface members in a braced dome. Common arrangements include Ribbed, Schwedler, Lattice, Kiewitt, Geodesic and Three-way grid. The three latter arrangements were compared in terms of global linear elastic stability, constructability and stiffness, in order to find the pattern most suitable to span 300 metres. It was concluded that the Geodesic geometry had the most suitable arrangement, primarily due to the slightly higher critical load in symmetrical and asymmetrical load scenarios, fewer number of unique elements lengths, and smaller deviation in the member length distribution.

The non-linear global elastic stability was studied concerning initial geometrical imperfections using linear buckling mode shapes and creep was studied by reducing the Young's modulus for permanent loads. These two phenomena were also looked studied in combination. The effect of radial and differential settlements on elastic stability, both in combination with initial geometrical imperfections, was also studied.

It was found that the structure was highly sensitive to initial imperfections with a lower bound critical value of only $0.135\frac{q}{q_{cr}}$, corresponding to a uniformly distributed load equal to 8.9 kN/m^2, when the structure was loaded symmetrically. This critical load value represents an outlier, over 95 % of the critical loads were above 15 kN/m^2. This was compared to the empirical formula, only applicable in the symmetrical load case, which estimated the global failure load to 19.6 kN/m^2.

Creep reduced the capacity down to $0.394\frac{q}{q_{cr}}$ of the linear buckling load in an asymmetrical load case covering 20 % of the dome area in the xy-plane. This corresponded to a uniformly distributed load of 29.9 kN/m^2. Neither radial nor differential settlements caused any decrease of the critical load. Combining creep and initial imperfections reduced the capacity further, from a lower bound value of $0.135\frac{q}{q_{cr}}$ to $0.081\frac{q}{q_{cr}}$, the latter corresponding to 5.4 kN/m^2. No synergistic effect was found. It was therefore concluded that global stability likely will not cause the dome to collapse, given that the design loads were significantly lower that the stability critical failure loads.

Material failure was also investigated in relation to initial geometrical imperfections as well as the combined effect of creep and imperfections. It was found that the stress level in the most critical beam would cause material failure if the maximum imperfection was larger than 0.8 metres, or $D/375$, leading to the conclusion that, perhaps, the primary cause for concern would be imperfection induced stresses, not imperfection induced global stability failure.

Sammanfattning

Denna rapport avser en stabilitetsanalys för att undersöka möjligheten att bygga en kupol i trä med en spännvidd på 300 meter. Alla lastbärande delar har modellerats med limträ av klassen GL30c och med dimensionerna 0.8×1.6 m^2. Lastfallen valdes till 2 kN/m^2 respektive 4 kN/m^2 för symmetriska och asymmetriska snölaster. De numeriska beräkningarna utfördes i finita element-mjukvaran Abaqus FEA och har jämförts med analytiska ekvationer, som modifierats med experimentell data.

Det diskreta skalet av kupolen kan bestå av en mängd olika mönster. Namnen på några vanliga mönster är Ribbed, Schwedler, Lattice, Kiewitt, Geodesic och Three-way grid, varav de tre sistnämnda jämfördes inom områdena elastisk stabilitet, styvhet och fördelar kring tillverkning och byggnation. Det fastställdes att kupolmönstret av typ Geodesic var mest fördelaktig och valdes därför för en vidare analys. Anledningarna till valet var den högre instabilitetslasten detta mönster hade vid både symmetriskt och asymmetriskt lastfall, färre antal unika balklängder och en mindre spridning på balkarnas längder.

Den olinjära globala elastiska stabiliteten studerades genom att ansätta modformer, med olika skalfaktorer, för att modellera imperfektioner. Krypning modellerades genom att reducera elasticitetsmodulen för permanenta laster. Sättningar undersöktes, både som en vertikal differenssättning och som en radiell sättning av en eftergivlig dragring. Den elastiska stabiliteten vid krypning och sättningar undersöktes också i kombination med imperfektioner.

Analysen visade att kupolen var väldigt känslig för imperfektioner, varav den olinjära knäckningslasten visade en undre gräns på $0.135\frac{q}{q_{cr}}$, vilket motsvarar en jämt utbredd symmetrisk snölast på 8.9 kN/m^2. Detta antogs vara ett avvikande värde då 95 % av imperfektionerna som undersöktes hade knäckningslaster på över 15 kN/m^2. Detta jämfördes med knäcklasten som beräknades analytiskt, vilket uppskattade denna till 19.6 kN/m^2, för ett symmetriskt lastfall.

Krypningen i trämaterialet reducerade knäcklasten som mest till $0.394\frac{q}{q_{cr}}$ i ett asymmetriskt lastfall där endast 1/5 av kupolens area var täckt. Detta motsvarade jämt utbredd snölast på 29.9 kN/m^2. Varken radiell sättning eller vertikal differenssättning påverkade den elastiska stabiliteten avsevärt. Kombinationen av krypning och imperfektioner reducerade knäckningslasten ytterligare, från $0.135\frac{q}{q_{cr}}$ till $0.081\frac{q}{q_{cr}}$ vid den undre gränsen, där den senare motsvarar en last på 5.4 kN/m^2. Någon synergieffekt mellan imperfektioner och krypning kunde dock inte urskiljas. Analysen av den globala elastiska stabiliteten sammanfattades därmed att kupolen inte utgjorde någon risk för instabilitet, då den dimensionerande brottlasten var avsevärt lägre än knäckningslasten.

Materialbrottet undersöktes i samband med initiala imperfektioner samt kombination av imperfektioner och krypning. Det observerades att spänningsnivåerna i den mest utsatta balken skulle genomgå materialbrott om imperfektionerna skulle utgöras av en maximal förskjutning på 0.8 meter, motsvarande $D/375$. Slutsatsen drogs att en större vikt av analysen på kupolen bör möjligen läggas på spänningar som uppstår av imperfektioner, framför stabilitetsbrott orsakad av imperfektioner.

Acknowledgements

This thesis was carried out at Lund University, faculty of Engineering, as a concluding part of the Master of Science in Civil Engineer programme. The thesis was written for the division of Structural Analysis and Design under the supervision of Ove Arup & Partners in Copenhagen.

We would like to thank our supervisor Roberto Crocetti from division of Structural analysis and design for helping us realise this project and helping us in contacts with the industry. Cooperation and synergy is the key for a successful project and we hope to see a continuation of this work in a near future.

We would also like to thank our second supervisor Silas Nørager from Arup for pushing us in the right direction and providing additional motivation throughout the months of hard work. Your involvement has given us another perspective on how to tackle problems.

Gustav Fredriksson & Markus Herrström
Lund 2017

Contents

Chapter 1

Introduction

The aim of this thesis is to study the feasibility of building a timber dome with a span of 300 metres, concerning non-linear elastic stability. The numerical calculations were performed using the software Abaqus FEA, and compared with analytic equations.

1.1 Background

Domes are half-spherical structures that can offer a very large span. The technique date back to 700 BC with masonry structures[1], and in AD 120-124, the Pantheon dome in Rome was built. While the diameter of 44 metres is today an outdated record, it turned out to be the largest dome in the world for almost 1800 years[1].

In modern times, continuous domes of concrete have been replaced with more efficient reticulated domes of lighter materials, primarily steel but also timber, making it possible to span longer distances. The domes are usually no longer governed by their self-weight, but by sensitivity to imperfections and asymmetrical loads. These two aforementioned "phenomena" led to the January 1963 collapse of the large span dome in Bucharest, the roof structure of the National Economy Exhibition Pavilion[2]. The failure was due to local accumulation of snow, causing local buckling of the thin reticulated dome which quickly propagated, leading to global failure.

While most domes use steel as the load-bearing material, several large spanning timber domes have been built. Four are listed below in order of their span[3].

- Superior dome - 163 metres - completed 1991
- Tacoma dome 161.5 metres - completed 1982
- Odate Jukai dome - 157 metres wide and 178 metres long - completed 1997
- Walkup Skydome - 153 metres - completed 1977

A timber dome with a span of 300 metres was considered to be built in China. This would nearly double the current world record: the Superior dome, with a free span of 163 meters. The current status of the project is unknown at this time, but the idea has raised interest in the feasibility of such a structure. This is also the main question of this thesis.

1.2 Purpose

The main purpose of this thesis is to investigate the non-linear elastic stability of a 300 metre span timber dome.

Question formulation

- Which dome geometry is most suitable to cover a span of 300 metres?
- How sensitive is a timber dome to imperfections applied in the shape of eigenmodes?
- If so, is there an easy/fast way to determine the non-linear elastic stability capacity, or does it require the study of several mode shapes?
- Can hand calculations accurately estimate the stability load?
- Can hand calculations accurately estimate the forces and the bending moments?
- How does creep influence the non-linear elastic stability capacity?
- How does the combined effect of creep and imperfections influence the non-linear elastic stability capacity?
- How does radial ring displacement/settlement negatively affect the elastic stability?
- How does differential vertical settlement negatively affect the elastic stability?
- **Is it feasible to build a timber dome with a span of 300 metres when non-linear elastic stability and material failure is taken into account**?

1.3 Limitations

The primary focus will be on the effect imperfection and creep has on the stability of the dome. Dynamic loads such as, but not limited to, earthquakes will not be studied. Nor will the effect of wind, rise and span ratio, and connection rigidity be included in the analysis, due to time constraints, which otherwise would have been interesting to study. Other areas outside the scope, perhaps not directly related to elastic stability, is the erection procedure as well as a potential optimisation of the dome geometry.

Chapter 2

Timber as a structural material

The following chapter concerns timber, both its properties as well as its use as a structural material. The material compounds will be described, which in turn will explain its behaviour in terms of strength, stiffness and movement due to creep. Engineering products like Glulam and trusses will be presented. Their properties and dimensional limitations concerning delivery and production are important factors to consider when designing a timber dome.

2.1 Why timber?

There are many reasons for using timber. As trends are ever-changing,the concept of building environmentally friendly is on the rise[4]. Sustainability and climate change are common arguments when discussing upcoming projects, and it is no doubt that timber has an advantage in that regard when comparing it to other commonly used structural materials.

Apart from the environmental argument, timber has fire resistant advantages as well. Despite being used as fuel in fireplaces, timber behaves seemingly favourably in terms of fire resistance. During combustion, timber decomposes and provides a layer of charring wood, which will slow down the temperature progression from reaching further in the section[5].

Another important advantage of using timber is its performance to carry its self weight. Consider the example of the column seen in fig. 2.1 to be loaded by its self weight. By use of the equations 2.1-2.4[6][7], it can be shown that the critical length l_{crit} is higher for a timber material than for steel, when same cross section area considered. This is summarised in table 2.1. This is because the ratio between stiffness and density of timber is favourable[8].

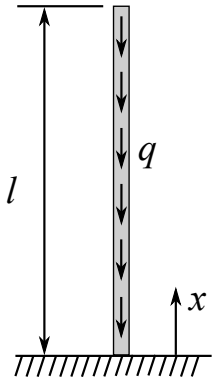

Figure 2.1: Column loaded by self weight, inspired by T. Wierzbicki[6].

$$l_{cr} = \sqrt[3]{\frac{7.84EI}{q}} \tag{2.1}$$

$$q = A \cdot \rho g \tag{2.2}$$

$$A = \pi r^2 \tag{2.3}$$

$$l_{cr} = 1.25\sqrt[3]{\frac{Er^2}{\rho g}} \tag{2.4}$$

Table 2.1: The self-weight buckling length of a steel and timber column, respectively

Material	MOE [MPa]	Density [kg/m^3]	Radius [m]	l_{cr} [m]	$\frac{E}{\rho g}$
Steel S355	210000	7850	0.1	37.4	2.68
Glulam GL30c[9]	13000	390	0.1	40.2	3.33

2.2 Strength and stiffness properties

Wood is an orthotropic material[10], which means that the material properties show a unique behaviour perpendicularly to each other in the three directions: Longitudinal, tangential and radial[11]. In the case of timber, the direction of the fibres are set as the reference when defining the three axis. The distinction between radial and tangential directions is usually disregarded and the stress is instead related to the orientations parallel $\sigma_{//}$ or perpendicular to the grain $\sigma_{\perp}$[10].

Likewise, the stiffness properties, modulus of elasticity E, shear modulus G and Poisson's ratio v, all have different values depending on the direction. Again, the radial direction is disregarded, which leaves six variables: $E_{//}, E_{\perp}, G_{//}, G_{\perp}, v_{//}, v_{\perp}$[10].

2.2.1 Tension and compression parallel to the grain

Tension along the fibre is where timber reaches its peak in terms of ultimate strength[10]. Compression in the same direction is close or only slightly less[10]. A tension-strain-curve shows an almost linear elastic curve, followed by a brittle failure when the limit is reached. The failure is caused either when the lamella between the fibres, or fibres themselves reach the limit[10], see fig. 2.2a.

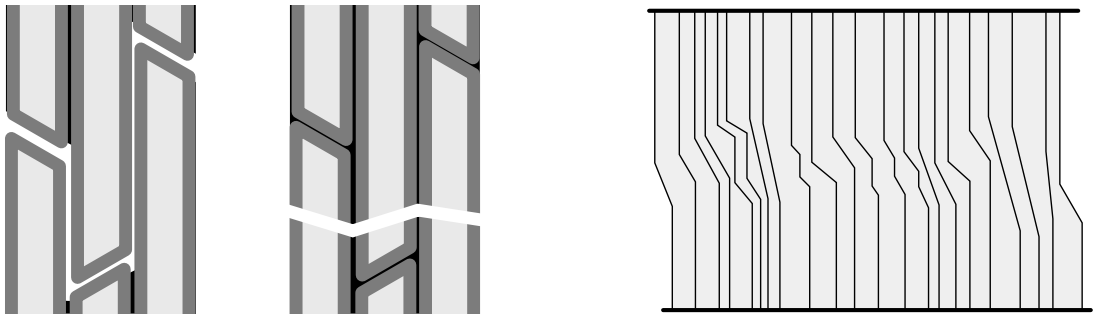

(a) Two failure modes in tension **(b)** Failure in compression

Figure 2.2: Failure behaviour due to tension and compression parallel to the grain, inspired by M. Johansson[10].

Compression parallel to the grain on the other hand shows a more non-linear behaviour. That is due to the local buckling of the fibres which causes local plasticity to develop[10], as seen in fig. 2.2b. Once the strength reaches its peak, the deflection will continue to approximately 3 times the strain level during strength limit. Compared to tension, compressing a timber member causes a slightly less brittle failure.

2.2.2 Tension and compression perpendicular to the grain

Unlike the strength properties along the longitudinal axis, strength limits perpendicular to the grain are significantly smaller than strength parallel to the grain. When subjected to tension, it does not take much until the fibres are cut open and reach failure. Although linear, the modulus of elasticity shows a stiffness of a considerably smaller value[10].

When the grain is compressed perpendicularly, it is harder to determine a strength limit. The fibre tubes will be crushed, but it does not necessarily result in a direct failure. Depending on the rest of the cross section, the stress levels might rise again prior to ultimate failure, and it is therefore difficult to determine an exact failure mode. The ultimate strength is still low, just as for tension in the same direction. The stiffness behaves more non-linearly in this case, but the initial modulus of elasticity is not much different from the one in tension[10].

2.2.3 Shear

The shear strength is higher in cases when planes are parallel to the grain, whereas the plane perpendicular to the fibres has a strength level of about half[10]. The latter case is also known as rolling shear and means that failure behaves in a manner where the fibres are rolling instead of direct breaking. This phenomena is however rarely governing and is seldom taken into consideration. There are a few cases where it is necessary to examine, like in the case of a glulaminated I-beam for instance[10].

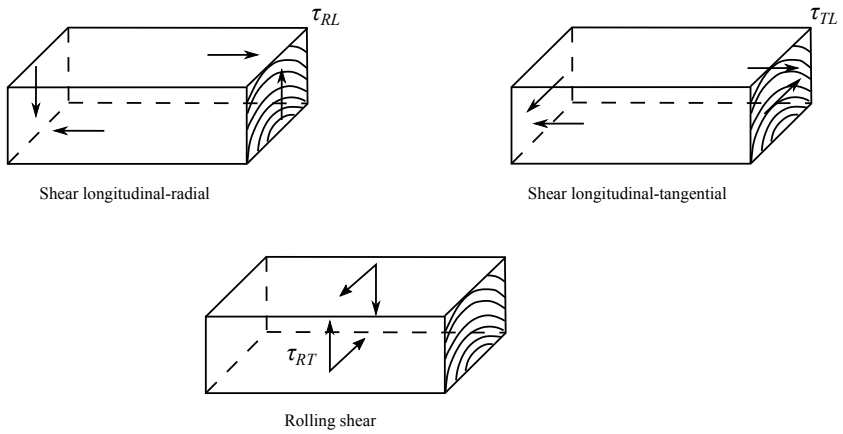

Figure 2.3: The three directions of shear, inspired by M. Johansson[10].

Out of the two other cases, the tangential-longitudinal stress, τ_{TL}, is slightly lower than the radial-longitudinal, τ_{RL}. This is due to the direction of the plane, where τ_{RL} is going right through layers of both early and late wood, while τ_{TL} has layers of only weaker early wood. It is not motivated to distinguish the two cases during the design phase, meaning it is only necessary to control the latter[10].

2.3 Creep

When a wooden member is subjected to a constant load for a prolonged time, the member will not only become instantly stretched due to linear elastic strain theory, but the strain will also increase over time. The time dependent deformation is non-linear and the rate decreases gradually[12]. This is explained by timber being defined as a viscoelastic material, and the behaviour is called creep[12].

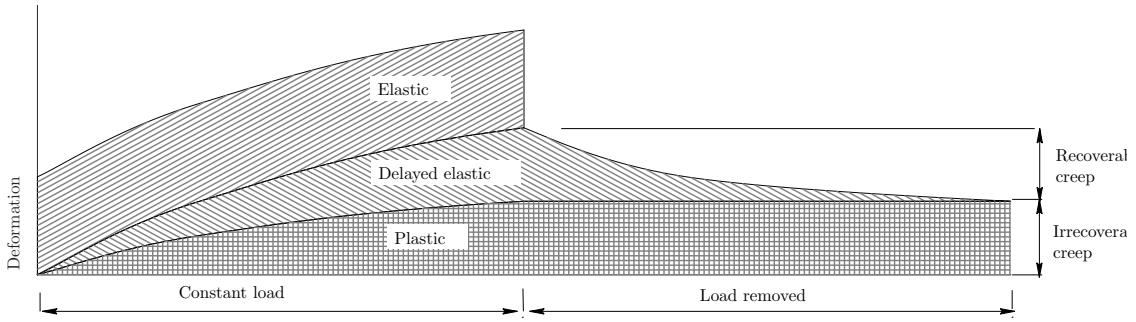

Figure 2.4: Load over time-deformation curve due to creep, inspired by J.M. Dinwoodie[12].

As seen in fig. 2.4, the effects of creep cause the deformation curve to split into three sections: instant elastic, delayed elastic and plastic. The instant elastic part is explained by the fact

that the load will cause the cross section to deflect according to Hooke's law, meaning it will also retract completely when unloaded. The other two components are due to creep, where the delayed elastic part is gradually recoverable after unloading, and the plastic zone is irrecoverable[12].

By limiting the scope to elastic compression, it can be seen in a load-deflection curve how the deflection starts increasing linearly with an increasing load. The linear manner will later transition into a non-linear, gradually decreasing, stiffness. The point of transition is known as the limit of proportionality[12]. The slope of a load-deflection curve is also known as Young's modulus (MOE, modulus of elasticity). When designing timber members, Young's modulus is usually approximated, either by taking the tangent of the linear section, or by drawing a straight line starting from zero stretching to the end of the curve, known as the secant modulus, as seen in fig. 2.5.

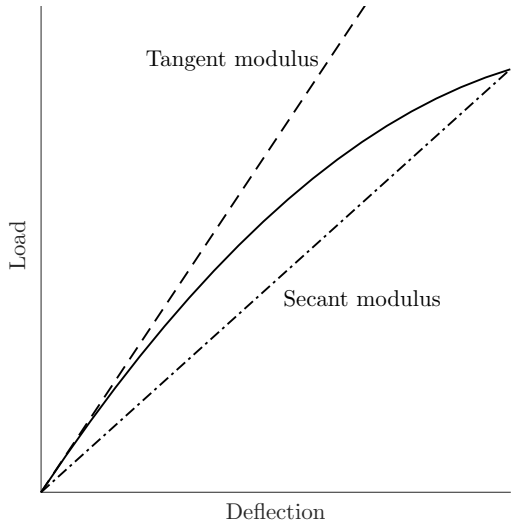

Figure 2.5: Load-deflection curve under compression, inspired by J.M. Dinwoodie[12].

It should be noted that these approximations are viable if the material response is truly elastic. This is however not exactly the case, as it was stated earlier that a part of the creep consists of a permanent plastic deformation. Fortunately, the degree of divergence is sufficiently small to still accept these approximations[12].

There are several governing factors when determining the creep magnitude, caused by the material itself and the surrounding environment. The behaviour is governed by the material stiffness, occurrence of knots, temperature, moisture and the load direction[10][12].

Eurocode treats creep as a factor added to the Young's modulus, to compensate for the extended non-linear long term deformation[10]. The method defines the creep factor k_{def} as deformation due to loading for an extended time. Equation (2.5) shows how the modulus is reduced[13]. Note that the modulus of elasticity does not decrease due to creep, but it is lowered to represent the reduced stiffness during permanent loads, meaning that the initial

stiffness is used for imposed loads.

$$E_{mean,fin} = \frac{E_{mean}}{1 + k_{def}} \tag{2.5}$$

2.4 Strength grading

Just like for any other material, the characteristic strength properties of timber are defined as the 5th percentile in a normal distribution, which is the point where 5 % of the samples are weaker. The normal distribution curve of timber is of special concern considering the large deviations of strengths timber tends to have due to properties reviewed above. In addition, the occurrence of knots in a member plays a significant role, as it has been shown in tests of Norway spruce that 90 % of the failures are caused by knots[10].

Grading and classification of timber is, according to most standards, carried out based on its characteristic bending strength[10]. Softwood of class C20 for instance, has a characteristic bending strength of 20 MPa.

2.5 Glulam - Glued laminated timber

Glulam was used as early as 1906, patented by Otto Hetzer, and it consists of a number of wood laminations glued together[14]. The purpose is to allow for a greater variety in the section geometry, as well as reducing the frequency of defects in order to achieve a high quality structural element[14].

2.5.1 Strength

While tests show that glulam is not significantly different than structural timber in terms of mean strength, its primary advantage is the smaller width of the Gaussian distribution curve. This makes the characteristic value significantly higher for glulam than for structural timber, as seen in fig. 2.6[10][14].

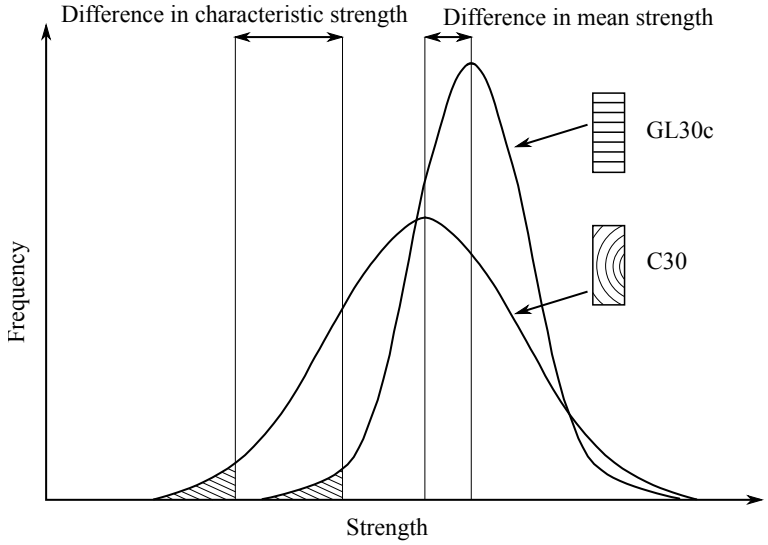

Figure 2.6: Comparison of distribution of strength between glulam and structural timber, inspired by M. Johansson[10] and Svenskt trä[14].

This is known as the lamination effect, which counteracts the influence of local weaknesses[14]. This results in a lower risk of knots appearing in the same section, thus preventing cases of bad timber samples. It is also possible, if desired, to vary members of different classes within a cross section. Having stronger classes in the upper and lower lamellas is beneficial in situations where stronger bending strength is important, but it is of lesser significance in case of pure compression.

2.5.2 Limitations of members

Dimensions of glulam members have few geometrical limitiations, and these are usually governed by machinery or transportation[14]. It is possible to achieve a greater variety of cross-sections, such as I- or box-sections, when comparing to conventional timber elements[14]. The longitudinal shape can be altered by initial curvature of a member[14].

In Sweden, the ordinary rectangular shapes usually have a limit in width of 215 millimetres, but gluing two beams side-by-side would allow for a larger width. The height is governed by the machinery limitations, which is approximately 2 meters[14]. The length is also restricted by transportation method and traffic regulations. Members up to 30 metres are acceptable in Sweden, while longer members require special permission[14].

2.6 Timber trusses

In a structural system, such as a roof structure, there are various methods to manufacture engineered members as a substitute to massive beams. The idea is to optimise the element to be able to reach a longer span. One alternative to massive beams is using timber trusses, which not only allows for very large spans, but also saves on the use of material[14].

Timber trusses replace massive structures with smaller elements, considered as bars. These bars are connected in a triangular pattern, with joints considered as pinned in design, making the web members of the trusses free from bending moment[15]. This is not entirely true however, due to imperfections, eccentricities and partially stiff joints, meaning that a perfect ideal truss system is seldom achieved[15]. This raises challenges in terms of design, and a method is to consider two cases: one with perfect pinned and one with rigid joints[15].

When replacing a massive beam, parallel trusses are commonly the equivalent to use. These consist of one straight upper chord and one lower, connected to each other with web members. The web members can either be loaded in compression or tension, depending on how they are configured[15]. Usually, diagonals in compression offer easier design of the connections, since the forces can be distributed through contact of each member[15]. The drawback of using longer diagonals in compression is the risk of member buckling[15].

As a general rule, use of trusses is usually a financial advantage as long as the span is over roughly 25-30 metres[15], but there are several issues to consider. First of all, the amount of connections should be limited to the least possible amount[15]. Secondly, in order to achieve a feasible optimum, the angles of the truss members should be close to 45 degrees[15]. And lastly, the bars should not be too slender and receive as little bending moment as possible[15].

In terms of transportation, truss members have the same restrictions as for ordinary members, as described earlier. The advantage found in a truss system is that it can be transported in several parts and be assembled on site[15].

Chapter 3

Shell Theory

This chapter introduces shells as an element and describes shell structures, primarily domes. The theory concerns both continuous and reticulated shell structures, and will begin by describing the mechanical use of shells.

3.1 Shells in general

Structural member are often described by straight lines, curved lines or surfaces, where examples of these are beams, arcs and plates[16]. A shell element is described by a curved surface, where the curvature can be in several directions, like a cooling tower, or a single direction, like a tube[16]. By the geometrical definition, a shell structure is also able to withstand tension forces, where a sail or a balloon are examples of such geometries[16]. Members in pure tension are, however, left out of the study since shell structures primarily use combined tension and compression.

3.1.1 Plate analogy

A shell element functions through *membrane* and *bending* action[16]. Describing these phenomena is best executed by using plate analogy. Therefore, consider the plate shown in fig. 3.1 as an example. The loads are acting both in and out of its plane, and an equilibrium involving the normal stresses σ_x, σ_y and shear stresses $\tau_{xy} = \tau_{yx}$ is shown in eq. (3.1)[16].

$$\begin{cases} \frac{\partial \sigma_x}{\partial x} + \frac{\partial \tau_{yx}}{\partial y} = q_x \\ \frac{\partial \tau_{xy}}{\partial x} + \frac{\partial \sigma_y}{\partial y} = q_y \end{cases} \tag{3.1}$$

Where q_x and q_y are out of plane external forces per unit area. Three variables and two equations make plane stress statically indeterminate[16], but if only plane stress is regarded, fig. 3.1a, q_x and q_y equals zero and the quantities can instead be expressed by the Airy stress function ϕ, see eq. (3.2)[16].

$$\sigma_x = \frac{\partial^2 \phi}{\partial y^2}, \qquad \sigma_y = \frac{\partial^2 \phi}{\partial x^2}, \qquad \tau_{xy} = \tau_{yx} = \frac{\partial^2 \phi}{\partial x \partial y} \tag{3.2}$$

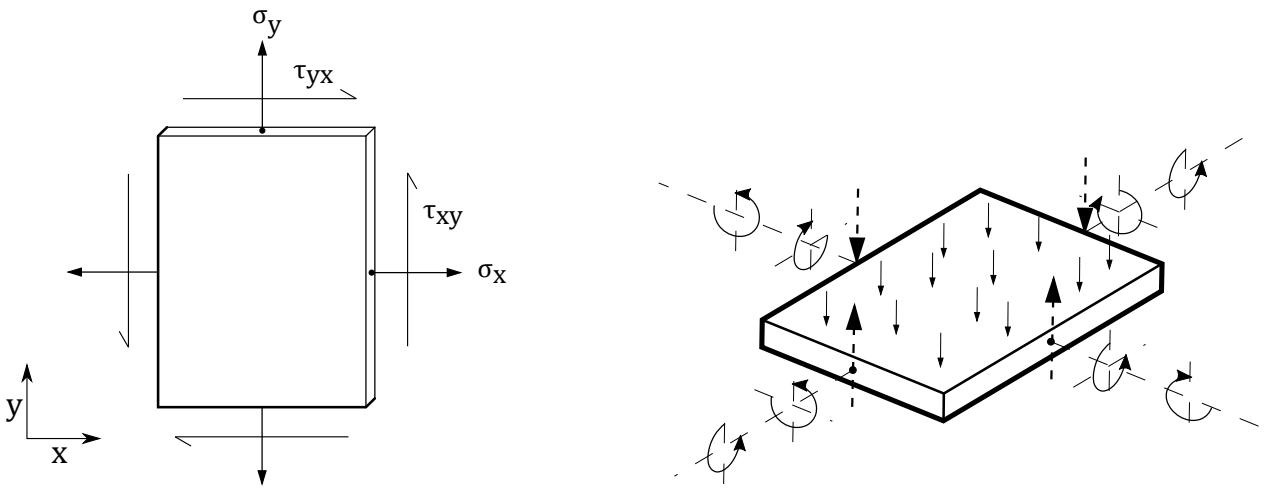

(a) Plane stress **(b)** Plate bending

Figure 3.1: Physical principles of a plate, inspired by C. Williams[16].

Inserting the relations from eq. (3.2) into eq. (3.1) shows that the equilibrium is indeed satisfied for any function ϕ. The basic stress-strain relationships for plane stress are introduced in eq. (3.3).

$$\begin{aligned} \varepsilon_x &= \frac{\partial u_x}{\partial x} &&= \frac{1}{E}(\sigma_x - v\sigma_y) \\ \varepsilon_y &= \frac{\partial u_y}{\partial y} &&= \frac{1}{E}(\sigma_y - v\sigma_x) \\ \gamma_{xy} &= \frac{\partial u_y}{\partial x} + \frac{\partial u_x}{\partial y} &&= \frac{2(1-v)\tau_{xy}}{E} \end{aligned} \tag{3.3}$$

where u_x and u_y are the displacements in each direction, E is Young's modulus and v is Poisson's ratio. The relations between the strains can be set up by the compatibility equation in eq. (3.4).

$$\frac{\partial^2 \varepsilon_x}{\partial x^2} - \frac{\partial^2 \gamma_{xy}}{\partial x \partial y} + \frac{\partial^2 \varepsilon_y}{\partial y^2} = 0 \tag{3.4}$$

Combining all the equations, 3.1 to 3.4 yields the biharmonic equation, seen in eq. (3.5)[16].

$$\nabla^4\phi = \frac{\partial^4\phi}{\partial x^4} + 2\frac{\partial^4\phi}{\partial x^2\partial y^2} + \frac{\partial^4\phi}{\partial y^4} = 0 \tag{3.5}$$

Note that this biharmonic function is a general function for any plate and is essential for the membrane action of a shell.

3.1.2 Membrane action

A shell uses the same equilibrium equations as the plate in eq. (3.1), with the three variables σ_x, σ_y and τ_{xy}. However, considering the curvature given for a shell, a third equilibrium, perpendicular to the tangent of the shell, is needed in order to make it statically determined[16]. Based on the biharmonical equation given in eq. (3.5), the third equilibrium is defined in eq. (3.6)[16]. The quantity p is the load acting in a plane area and z is the third coordinate describing the height of the shell.

$$p = \frac{\partial^2\phi}{\partial x^2}\frac{\partial^2 z}{\partial y^2} - 2\frac{\partial^2\phi}{\partial x\partial y}\frac{\partial^2 z}{\partial x\partial y} + \frac{\partial^2\phi}{\partial y^2}\frac{\partial^2 z}{\partial x^2} \tag{3.6}$$

The concern with membrane action in a structure is that it is largely depending on the shape and the boundary conditions. If the function ϕ is unsolvable for a desired shape, the shell is likely a mechanism, as long as only membrane action is regarded[16]. Domes and cooling towers are, by their geometry, examples of viable shapes for pure membrane action. A dome with a hole at its apex, however, cannot fulfill the conditions for membrane action and the structure might undergo inextensional deformations[16].

Despite the involved differential equation presented in eq. (3.6), domes in particular become seemingly easy to analyse in terms of membrane action. Methods for calculating forces in reticulated domes are reviewed in section 3.3.

3.1.3 Bending action

In situations where membrane action is insufficient to satisfy equilibrium, bending stiffness is necessary[16]. In practice however, due to geometrical imperfections and asymmetrical load cases such as wind and snow, bending action will always be present, regardless of geometry[16].

Bending action also takes a central role when considering buckling[16]. Particularly, due to the optimised shapes of shells, buckling needs to be analysed thoroughly[16]. The efficient geometry results in tiny, and in most cases, negligible deformations prior to sudden buckling collapse[16]. Buckling and instability in general is discussed in more detail in chapter 4.

In comparison to the membrane action, bending action is far more complicated and thus important to consider in a shell structure[16]. Since hand calculations of this kind are difficult, if not even impossible in practice, it leaves no other choice but to use computer analysis including large deformation analysis[16], also known as third order theory, which will be discussed in chapter 4. Even the results of a computer software should be treated with care and, if possible, should also be compared with various sources and perhaps even with a physical model.

3.2 Dome structures

The shape of a dome is defined as synclastic with a positive Gaussian curvature[16], meaning the curved surface is bent to the same side in every direction. By its definition, a dome is not necessarily accompanied with a circular bottom surface and might as well have an oval shape. When the outer shape of a dome is following a hemisphere, it is known as a spherical dome. The following section will primarily regard spherical domes.

3.2.1 Reticulated dome structures

As development progressed, new materials and new methods were created[17]. Domes made of timber and aluminium do not only weigh less, but also optimise the skeleton of the shell using a reticulated grid to mimic the behaviour of a continuous shell. The development of these types of domes turned out to be attractive as they offered an economic solution lowering the material use in relation to the open floor space, which in turn made them suitable for sports complexes of different kinds[1]. While the design of masonry domes is governed by self-weight, reticulated domes are instead challenged by asymmetrical loads as they may cause instability[17][1].

3.2.2 Dome patterns

There are several ways on how the grid of the dome can be performed. The dome patterns covered in this report are: Ribbed, Schwedler, Three-way grids, Kiewitt, Lattice and Geodesic. They can be seen below in fig. 3.2.

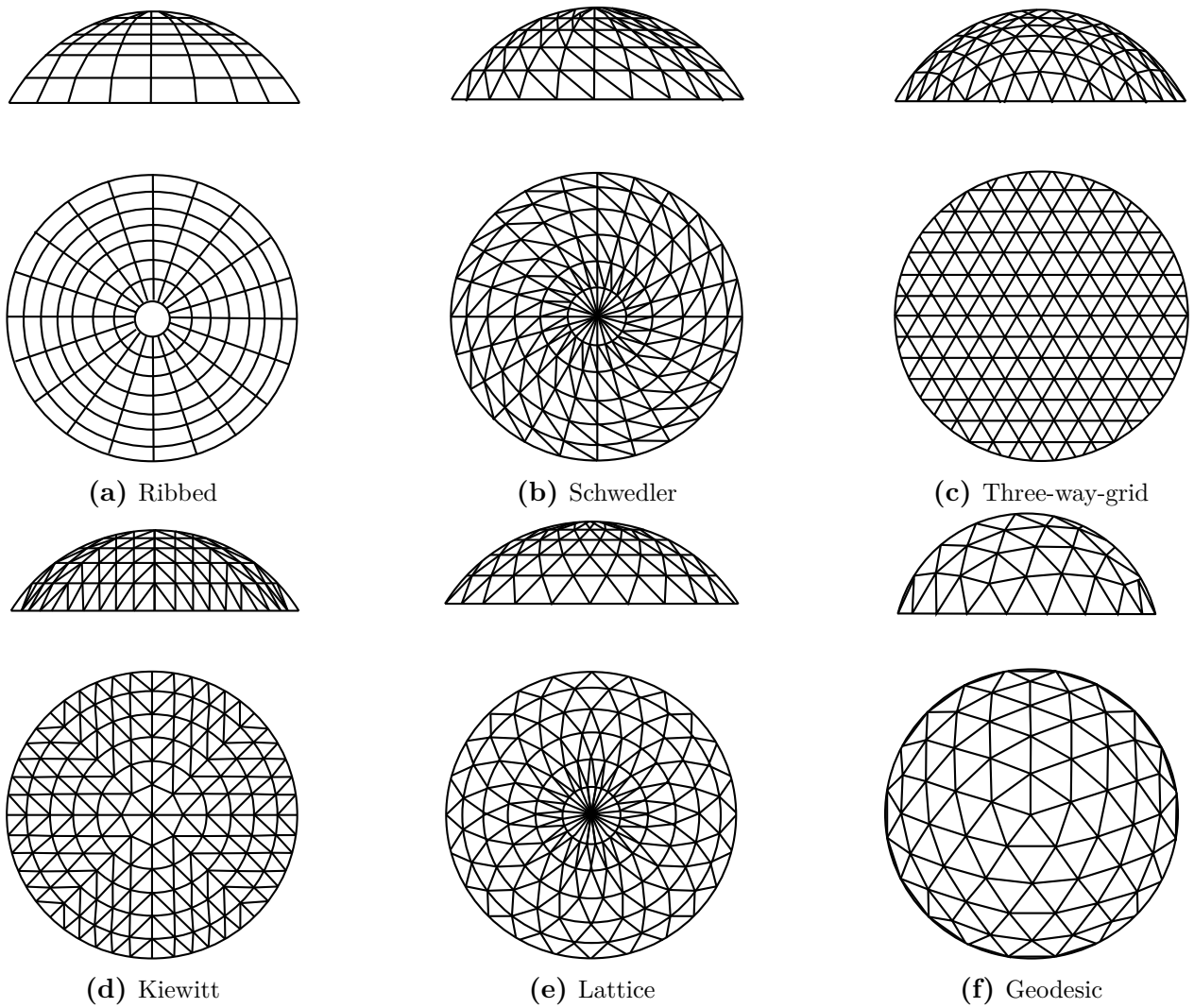

(a) Ribbed **(b)** Schwedler **(c)** Three-way-grid

(d) Kiewitt **(e)** Lattice **(f)** Geodesic

Figure 3.2: Different dome geometries, inspired by W.F Chen, and E.M. Lui[18].

The ribbed dome, fig. 3.2a, is built by a set of rotated meridional members and a ring-structure[18]. The Schwedler pattern seen in fig. 3.2a, introduced by the German engineer J.W. Schwedler, is a continuation of the ribbed pattern, with the addition of diagonals in the trapezoidal spaces of the ribbed dome[18].

The three-way grid shown in fig. 3.2c consists of an equilateral triangular plane which is projected onto the spherical surface. According to theoretical analysis, this pattern distributes forces seemingly well, even during asymmetrical loading, thus making three-way-grid economical[18].

The configuration shown fig. 3.2d is a lamella pattern, usually called Kiewitt, after its founder G. R. Kiewitt[19][18]. Much like the ribbed and the Schwedler configurations, the lamella patterns are based on rings. The Kiewitt pattern consists of several sectors, normally six or eight, in its circular plan[18]. In each sector, the stiffness is enhanced by additional two-way

rib system, creating the pattern shown in fig. 3.2d[18].

The lamella pattern shown in fig. 3.2e is sometimes referred to as lattice dome[17]. A way to obtain the geometry of such pattern is to start by rotating circles, both counter clockwise and clockwise, that are tangent to the center-point of the dome. This will generate the curved lines seen in fig. 3.2e. Adding circles in the horizontal plane will complete the generation of the nodes. According to the dome construction company Geometrica[20], the location of the rings can be changed such that equilateral triangles are created on each level.

Lastly, in fig. 3.2f, is the Geodesic grid, patented by Buckminister Fuller[21]. The Geodesic grid can be created in at least two ways: By use of an icosahedron[21] and by tilting planes[22][17]. The former method uses a platonic solid icosahedron which is a polyhedron with 12 vertexes, 20 faces and 30 edges, as seen in fig. 3.3a. Every face can be sub-divided into smaller faces, which is then exploded to the sphere in which the icosahedron is encapsulated[21]. The result becomes the spherical pattern shown in Fuller's patent in fig. 3.3b.

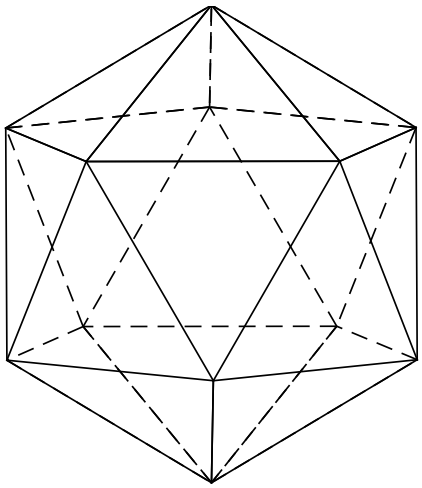

(a) Regular Icosahedron.

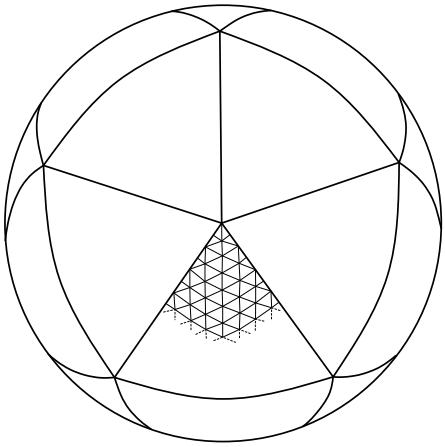

(b) Fuller's patent of a Geodesic dome, inspired by R.B. Fuller[21].

Figure 3.3: Construction of an icosahedron based dome geometry

The second way to create the geometry is based on tilting planes. According to Lüning[22], this is done by dividing a circle in the xy-plane into six sectors and drawing extended lines from those sectors, as seen in fig. 3.4a. Three great circles are drawn from these locations as a first step. The next step is to repeatedly tilt two great circles from each of the initial three. The intersections generated will be the node locations. A thorough definition of the node location of the Geodesic, Lace and Kiewitt domes is performed in section 6.3. The Geodesic dome created by means of tilting planes will, however, not be discussed further.

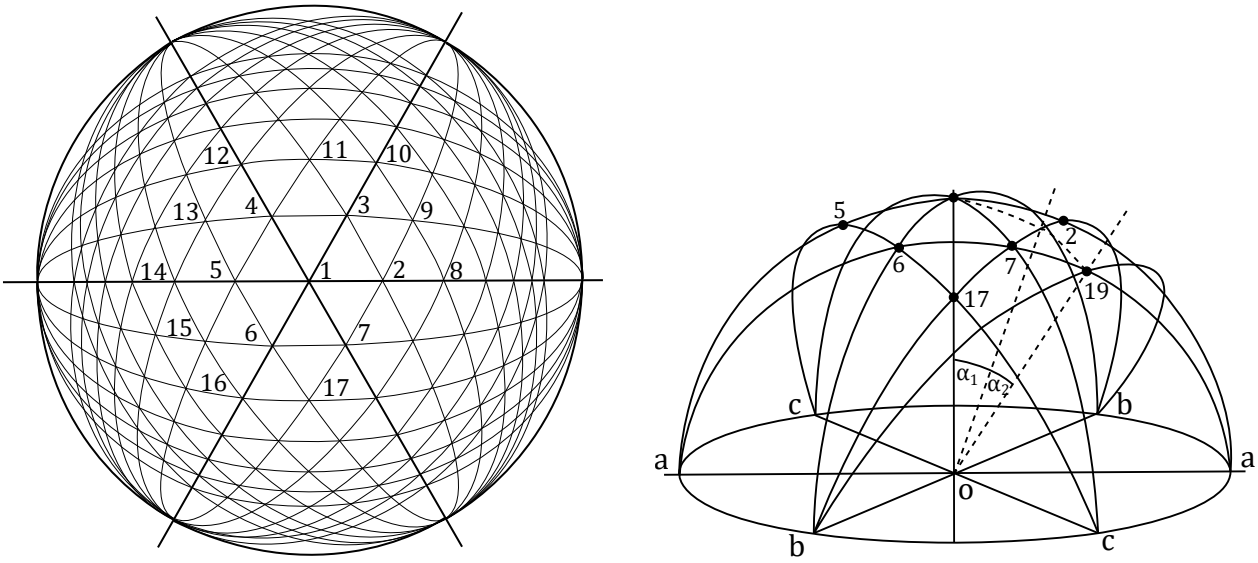

(a) Tilting planes seen from above **(b)** Great circles intersecting each other

Figure 3.4: Creation of geodesic dome by use of tilting planes, inspired by E. Lüning[22].

Despite new designs appearing as years have passed, some of the older models are still being used as they might offer advantages of their own. In general, the factors to consider are as following:

- design[22]
  - The number of members of different lengths[17].
  - The number of unique connections needed[17].
  - The complexity of jointing[17].
- production energy[22]
- assembly[22]
- transport[22]
- fire resistance[22]
- strength[22]
- rigidity[22]

3.2.3 Rise and span

The rise to span ratio is an important factor that needs to be considered in the design stage. The ratio plays an important role concerning deflection, axial force, and buckling[23]. The

latter is discussed in section 4.4. To get a sense of suitable height to span ratio, one can start by looking at large span timber domes that have already been built. Table 3.1 shows that the ratio is close to 0.3 for most large timber domes, the Oulu dome in Finland being the only outlier with a ratio close to 0.2.

Table 3.1: Height to span ratio for large timber domes

Dome Name	Location	Height [m]	Span [m]	H/D
Tacoma Dome[3]	Tacoma, USA	48	161.5	0.30
Federico II (1)[24]	Brindisi, Italy	46	143	0.31
Federico II (2)[24]	Brindisi, Italy	49	143	0.34
Superior Dome[3]	Marquette, USA	49	163	0.30
Izumo Dome[3]	Izumo, Japan	49	143	0.34
Konohana Dome[25]	Miyazaki, Japan	38	122	0.31
Odate Jukai Dome[3]	Oguni, Japan	52	178	0.29
Oulu Dome[3]	Oulu, Finland	23.9	115	0.21
Walkup Skydome[3]	Flagstaff, USA	43.3	153	0.28

Pan and Girhammar[23] show that the 0.3 ratio will result in a low relative deflection value as well as a normal force that is trending downwards, fig. 3.5a fig. 3.5b, respectively. The 0.30 ratio is also close, although not at a minimum point, when regarding the maximum relative bending moment.

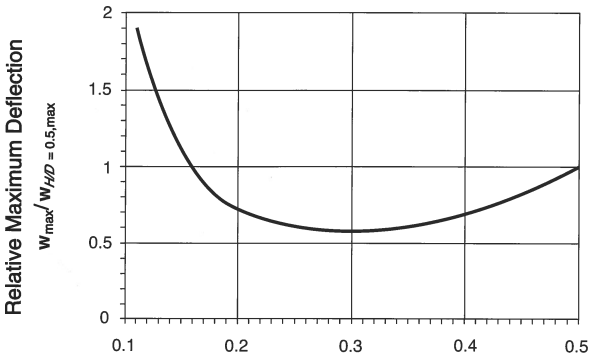

(a) Relative maximum deflection versus height to span ratio

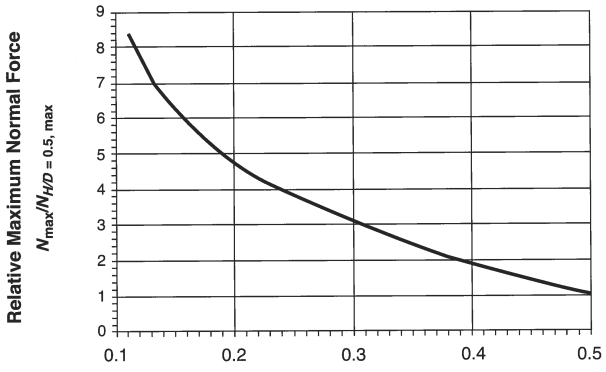

(b) Relative maximum normal force versus height to span ratio

Figure 3.5: Relative maximum displacement and normal force as a function of the height to span ratio (H/D), figure from D.H. Pan and U.A. Girhammar[23].

$w_{max}/w_{H/D=0.5,max}$	Deflection ratio depending on rise versus span
$w_{H/D=0.5,max}$	Maximum deflection when $H/D = 0.5$
$N_{max}/N_{H/D=0.5,max}$	Deflection ratio depending on rise versus span
$N_{H/D=0.5,max}$	Maximum normal force when $H/D = 0.5$
D	Dome span

H	Height(rise) of the dome

3.3 Analysis of reticulated domes

When analysing a reticulated dome, there are mainly two approaches: The equivalent continuous shell analogy and the discrete structure method[26]. The first method is suited for the preliminary design, as it is relatively easy to use and allows for hand calculations. This method involves using the properties of a continuous shell in membrane action, whereas its computed forces are translated into the reticulated grid thanks to the similar behaviour of the grid shell.

The latter method, the discrete structure method, regards computational finite element calculations of a model containing every single member in a reticulated structure[26]. This approach goes directly onto analysis of the actual structure and is able to thoroughly determine stresses in terms of both membrane and bending action which makes it a useful tool to compare and complete the preliminary design gained from the first method. The computer calculation is also able to trace the non-linear behaviour of domes and determine buckling, which is often a critical case for domes[26]. Since buckling is the main topic of this thesis, it will be more thoroughly described in chapter 4.

Although the computer method is supposedly superior in every regard when analysing domes, it is important to highlight how the hand calculation approach can be used to validate the output gained from computers. The following section presents the formulas needed for the preliminary design.

3.3.1 Membrane forces in a continuous shell element

Consider a small continuous shell element seen in fig. 3.6. The element has a thickness t and is arbitrarily located in a general shell structure. The geometrical parameters are accompanied by two radii, R_φ and R_θ, defined in the same direction as dS_φ and dS_θ. Depending on the structural shape, the radii can vary differently and independently from each other. A cylinder, for instance, has the radii $R_\varphi = \infty$ and $R_\theta = constant$ and a spherical surface has two equal radii $R_\varphi = R_\theta$[27].

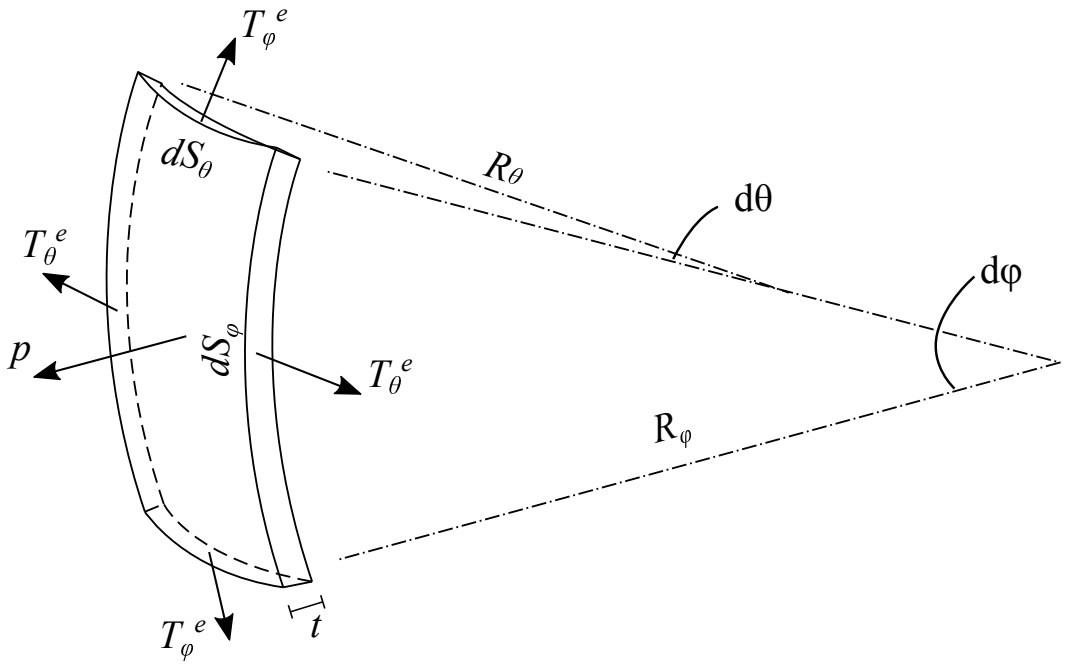

Figure 3.6: Shell element, inspired by Mukhanov K.K.[27].

With the geometrical parameters presented, the element is subjected to a uniformly distributed load p directed perpendicularly to the surface, which is taken by axial reaction forces, T_φ^e and T_θ^e. Based on all of the external forces, an equilibrium can be set up according to eq. (3.7).

$$2T_\varphi^e \sin\frac{d\varphi}{2} + 2T_\theta^e \sin\frac{d\theta}{2} - pdA = 0 \tag{3.7}$$

$$T_\varphi^e = \sigma_\varphi dS_\theta t, \qquad T_\theta^e = \sigma_\theta dS_\varphi t \qquad [\mathrm{N}] \tag{3.8}$$

The forces T_φ^e and T_θ^e are from the membrane stresses acting on the sections in each direction, described in eq. (3.8). The angles $d\varphi$ and $d\theta$ are considered infinitesimal, therefore $\sin\frac{d\varphi}{2} = \frac{d\varphi}{2}$ and $\sin\frac{d\theta}{2} = \frac{d\theta}{2}$. Finally, by expressing the angles in terms of the ratios $d\varphi = dS_\varphi/R_\varphi$ and $d\theta = dS_\theta/R_\theta$ yields the relation given in eq. (3.9)[27].

$$p = \frac{T_\varphi^e}{R_\varphi\, dS_\theta} + \frac{T_\theta^e}{R_\theta\, dS_\varphi} \tag{3.9}$$

The relation can also be expressed in terms of stresses by using eq. (3.8), resulting in eq. (3.10)[27].

$$\frac{\sigma_\varphi}{R_\varphi} + \frac{\sigma_\theta}{R_\theta} = \frac{p}{t} \tag{3.10}$$

3.3.2 Loads and forces in domes

Force distributions

For a spherical dome, two directions are used when describing the internal force distribution: The meridian and the hoop directions[27]. The meridian direction goes from its apex to the base, whereas the remaining hoop or annular direction, goes in a horizontal line around the dome[27].

A typical force distribution of a dome is shown in fig. 3.7 when uniformly load applied. The meridional force increases as it reaches the base, and are withstood by the hoop forces in tension[27]. Consequently, this ends up in a relatively large tension force along the base, which is usually taken by a larger tension ring that needs to be designed[27].

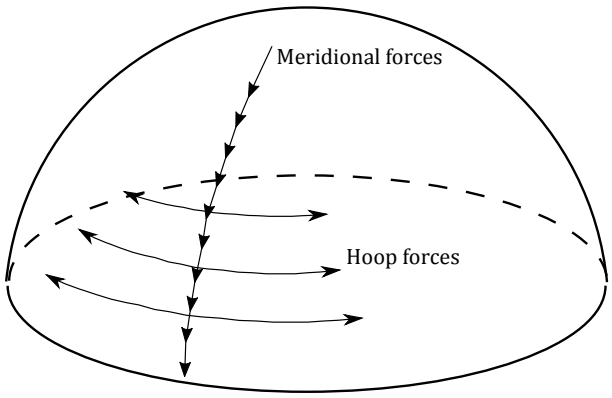

Figure 3.7: Force distribution in meridian and hoop of a dome

The force equilibrium of a dome is assembled by eq. (3.9) and by making use of the equal radii, $R_\varphi = R_\theta = R$. Let T_φ and T_θ denote the meridional and annular forces in the dome respectively. Note that these forces are now defined as force per metre, thus the element length dS is no longer necessary. The new relation is found in eq. (3.11)[27].

$$T_\varphi + T_\theta = pR \tag{3.11}$$

In the case of a perpendicular pressure p, T_φ and T_θ are equal, which means that the relation in terms of stress is written according to eq. (3.12)[27][28][29].

$$\sigma_\varphi = \sigma_\theta = \frac{pR}{2t} \tag{3.12}$$

This expression is, however, not useful for cases concerning vertical loads, such as dead load

or snow load, nor is it compatible with wind loads. The formula will instead remain useful presenting the buckling pressure of a spherical shell in section 4.2.

Dead load

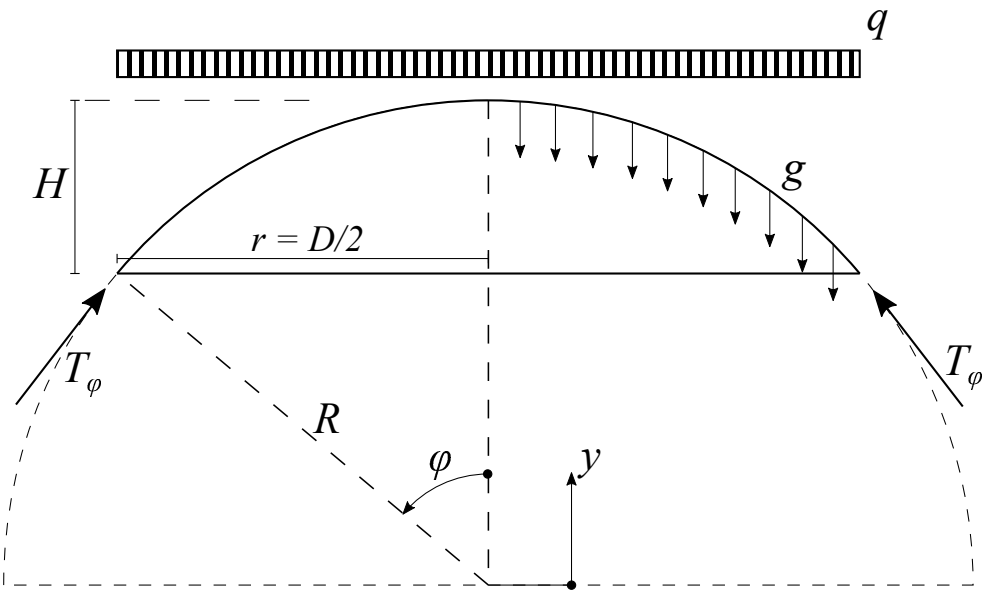

Figure 3.8: Dome subjected to dead load and uniformly distributed load, inspired by K.K Mukhanov[27].

When the dome is subjected to a dead load g, the equation describing the total load by a function starting from the apex is defined by Mukhanov[27] as in eq. (3.13), with y given as the vertical distance from the apex. The total load G is given in kN.

$$G = -g2\pi R(R - y) \tag{3.13}$$

The reaction force of the dead load must be taken vertically by reaction forces. This is balanced by T_φ as seen in eq. (3.14).

$$T_\varphi \ 2 \ \pi \ r \ \ \sin\varphi = G \tag{3.14}$$

Where φ is the latitudinal angle from the centre of origin. Thus, a relation of the meridional force in terms of dead load is found as shown in eq. (3.14). The rightmost part is obtained when translating the Cartesian coordinate y to a spherical: $y = R\cos\varphi$.

$$T_\varphi = \frac{G}{2 \ \pi \ r \ \ \sin\varphi} = -g\frac{R^2}{R+y} = -g\frac{R}{1+\cos\varphi} \tag{3.15}$$

Likewise, going back to the equilibrium in eq. (3.11) yields T_θ in terms of either a distance y or angle φ, shown in eq. (3.16).

$$T_\theta = -Rg\left(\cos\varphi - \frac{1}{1+\cos\varphi}\right) = -g\frac{y^2 + yR - R^2}{y+R} \tag{3.16}$$

A verification of these formulas can be made. Shown in eq. (3.17) in the case at the apex of the dome, $y = R$ or $\cos\varphi = 0$ yields in equal compression for both T_φ and T_θ. The bottom of the dome, $y = 0$, results in an equal magnitude in force for T_φ and T_θ, but in different direction, where T_φ will remain in compression.

$$\begin{aligned} y = R, \quad \cos\varphi = 1 \qquad &\longrightarrow \quad T_\varphi \quad = T_\theta = -g\frac{R}{2} \\ y = 0, \quad \cos\varphi = 0 \qquad &\longrightarrow \quad T_\varphi \quad = -T_\theta = -gR \end{aligned} \tag{3.17}$$

Uniformly distributed load

Similar to the dead load, uniformly distributed load q is in this case independent on the height and therefore described as in eq. (3.18)[27].

$$G = -q\pi r \tag{3.18}$$

Again, the meridional and annular forces T_φ and T_θ are obtained through eq. (3.13) and eq. (3.11). These are presented in eq. (3.19).

$$\begin{aligned} T_\varphi &= -\frac{qR}{2} \\ T_\theta &= -\frac{qR}{2}\cos 2\varphi \end{aligned} \tag{3.19}$$

This makes the meridional force constant throughout the section, while the annular goes from compression at the apex to tension with same magnitude at the bottom of the half sphere.

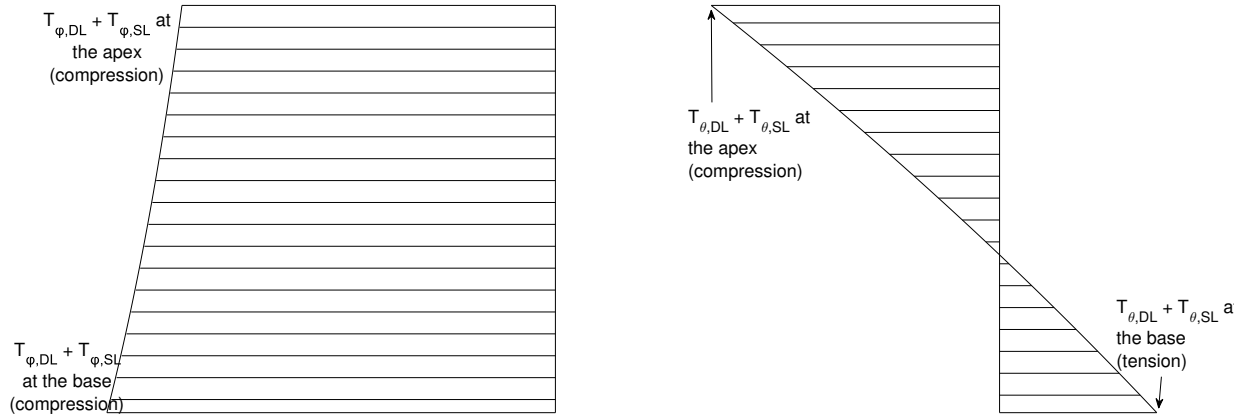

(a) Meridional force **(b)** Hoop force

Figure 3.9: Theoretical force variation vs height using formulas found in this secion.

Wind load

Considering the case described by Mukhanov[27], the wind pressure q_w is based on the vertical design wind load $q_{w,v}$. The wind pressure is written,

$$q_w = q_{w,v} = \sin\varphi \sin\theta \tag{3.20}$$

and the meridional and annular forces become as in eq. (3.21) and eq. (3.22), respectively.

$$T_\varphi = q_{w,v} R \frac{\cos\varphi}{\sin^3\varphi}\left(\frac{2}{3} - \cos\varphi + \frac{1}{3}\cos^3\varphi\right)\sin\theta \tag{3.21}$$

$$T_\theta = q_{w,v} R \left[\sin\varphi - \frac{\cos\varphi}{\sin^3\varphi}\left(\frac{2}{3} - \cos\varphi + \frac{1}{3}\cos^3\varphi\right)\right]\sin\theta \tag{3.22}$$

Forces in reticulated members

Reticulated domes are, by their geometry, indeterminate structures of a high degree[30]. Doing repetitive calculations with varying sections could end up in a cumbersome process, which makes shell analogy a useful tool when estimating forces in the early design stage. This theory is based on a few conditions listed below.

- The reticulated dome pattern is of a regular uniform mesh[30].
- The members of the dome should all be equal in both section and length[30].
- The dome does not have any large openings or any other discontinuity in its pattern[30].

Even if all these conditions are seldom fulfilled, comparisons by hand calculations and experiments shows that they in most cases give a fairly accurate result[30].

With the given meridional and annular forces derived in the previous sections, it is possible to estimate actual forces in a reticulated system, if the members of interest follow either the meridian or the hoop. Starting from a geodesic icosahedron dome seen in fig. 3.10 for instance, five lines extend from the apex downwards to the circle. The forces in these members are determined by the meridional force T_φ multiplied by the effective width, a, found in the mesh density. Likewise, the force in any member that coincides with the annular direction can be determined similarly by multiplying the annular force T_θ with its effective width b[27].

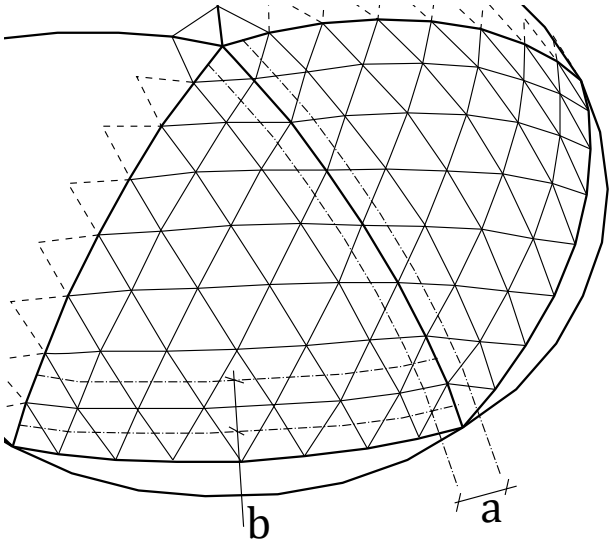

Figure 3.10: Influence width to be multiplied with the meridian and hoop forces, K.K Mukhanov[27].

Chapter 4

Stability

4.1 General stability

According to Samuelson[28], the instability phenomena can be described using the simple examples of a ball representing the equilibrium condition in a system. The ball can be located in a stable, indifferent or unstable condition, where fig. 4.1a-c would be stable, indifferent and unstable respectively. This is explained by considering a disturbance in the system, which would cause the ball to move out of position. The concave surface in fig. 4.1a would cause the ball to fall back to its original position, thus ensuring stability. If the curve on the other hand is convex, as shown in fig. 4.1c, a disturbance would cause the ball to move even further, resulting in large deformations. The indifferent condition means that the potential energy for moving the ball is equal to zero, as presented in fig. 4.1b.

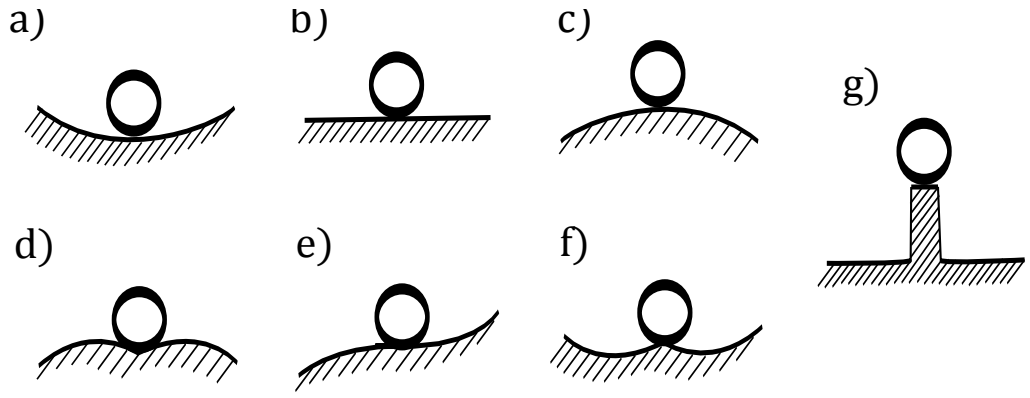

Figure 4.1: Example of a ball representing equilibrium conditions, inspired by L.A. Samuelson, and S. Eggwertz[28].

The shape of the curve is widely depending on the structural system and it is not always as simple as concluding a collapse in a single unstable case. As can be seen in fig. 4.1f for instance, a small disturbance in equilibrium causes a displacement followed by a new stable condition. As for shell structures in particular, their sensitivity to buckling is described in fig. 4.1g, explaining that a small disturbance in the system could cause a sudden change in

position[28].

Having the equilibrium and instability phenomena introduced, they can in practice often be used as the definition of structural collapse[31]. The reason is that instability tends to lead to very large deformations, which in turn either reach the material strength limit, or it changes the structural shape to such a degree that the building is unserviceable. Runesson et al.[31] point out the importance of instability as it usually occurs instantaneously, without any cautionary displacement for instance.

Second order theory

First order theory in mechanics regards simple linear elastic analysis with displacements direct proportional to the subjected force, while second order theory also takes small deflections in geometry into consideration. Although the change is small, it could be significant in the equilibrium as it adds additional loads to the system[31].

An example is shown by considering a beam as seen in fig. 4.2. The beam, with the length L, is pinned in one end and supported by a spring with the stiffness k in the other, while being subjected to a transverse force F and an axial force P according to fig. 4.2a. The equilibrium equation around point A, with respect to the deformed shape beam in fig. 4.2b, can be seen in eq. (4.1). As opposed to a first order analysis, the stiffness of the system is reduced due to the compression force[32]. As stated before, second order theory assumed that the angle θ is small. Meaning, $cos\theta \approx 1$, and $sin\theta \approx \theta$.

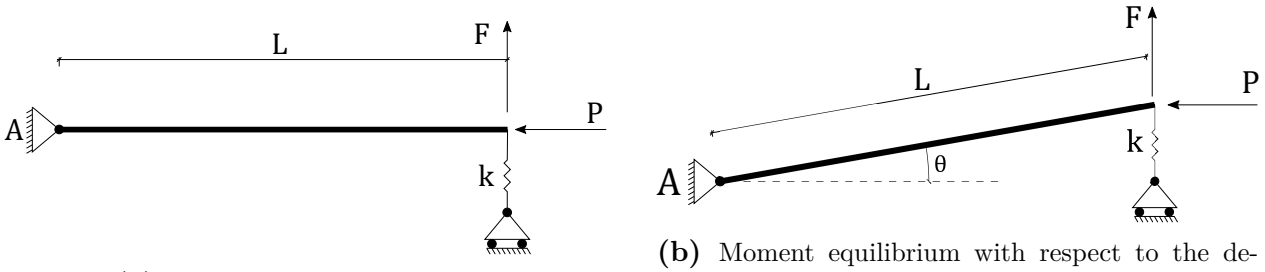

(a) Beam supported by a spring

(b) Moment equilibrium with respect to the deformed shape

Figure 4.2: Example of second order theory, inspired by Gustafsson[32]

.

$$\curvearrowleft A : FL + Pu - kuL = 0 \quad \Longrightarrow \quad F = \left(k - \frac{P}{L}\right) u \tag{4.1}$$

Third order theory

Based on second order theory, third order theory takes into account that the displacements may no longer be small. This leaves a non-linear behaviour of forces and displacements, which are calculated iteratively, in small increments, to find an equilibrium path[31].

Figure 4.3 used to illustrate third order theory and it is a continuation of the previous example seen in fig. 4.2. Large deformations are assumed, thus the horizontal length l is introduced such that $l = \sqrt{L^2 - u^2}$. The equilibrium around A can be seen in eq. (4.2).

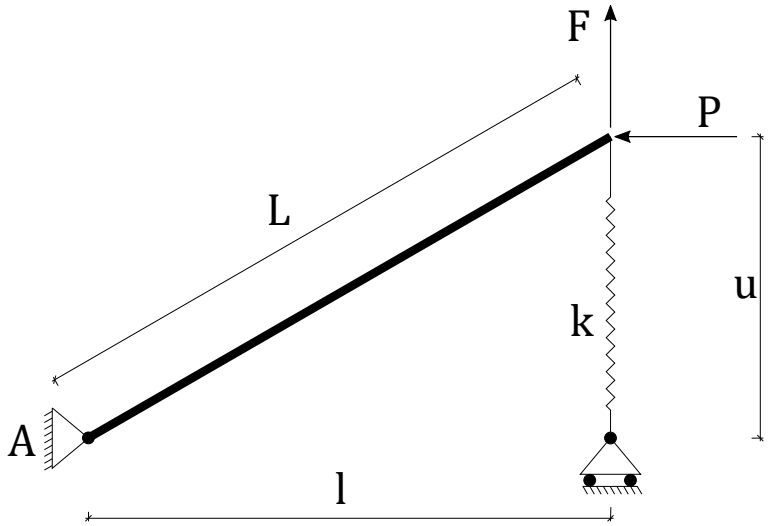

Figure 4.3: Equilibrium assuming large deformations, inspired by Gustafsson[32].

$$\overset{\curvearrowleft}{A} : Fl + Pu - kul = 0 \quad \Rightarrow \quad F = ku - P\frac{u}{l} \quad \Rightarrow \quad F = \left(k - \frac{P}{L}\frac{1}{\sqrt{1-(u/L)^2}}\right)u \quad (4.2)$$

In comparison to the second order equilibrium shown in eq. (4.1), the third order results in a non-linear stiffness, $\frac{P}{L}\frac{1}{\sqrt{1-(u/L)^2}}$, governed by the deformation u[32].

4.1.1 Buckling of columns - Euler's formula

Consider a single two-pinned column of a length l, as seen in fig. 4.4a. When loaded with a concentrated force P, only axial strain will be present as long as first order theory is concerned. If the critical buckling load is reached, the column might undergo lateral displacement, thus going from a stable to an unstable condition[29]. In order to understand this

behaviour, a small lateral imperfection y must be considered at the midpoint of the same column. An equilibrium in terms of the moment is set up according to eq. (4.3)[33].

$$\sum M(0) = 0 \Rightarrow P \cdot y - M_S = 0 \tag{4.3}$$

$$M_R = EIy'' \tag{4.4}$$

where

M_S Destabilising moment
M_R Stabilising moment
y'' The second derivative of y with respect to x
EI Bending stiffness

By setting the destabilising moment M_S equal to the stabilising moment M_R from eq. (4.4), and let then α^2 to represent $\frac{P}{EI}$, a differential equation is set up according to eq. (4.5)[33].

$$y'' + \alpha^2 \cdot y = 0 \tag{4.5}$$

The equation is solved by use of a general solution $y = A\sin\alpha x + B\cos\alpha x$, which in this case gives the solution $\alpha = \pi/l$ as the lowest value[33]. The buckling load is determined in eq. (4.6).

$$\alpha^2 = \frac{\pi^2}{l^2} = \frac{P}{EI} \Rightarrow P = P_{cr} = \frac{\pi^2 EI}{l^2} \tag{4.6}$$

By assuming different boundary conditions, Euler's buckling formula can be expressed in more general terms as in eq. (4.7), where β is chosen according to the cases seen in fig. 4.4[33][29][31].

$$P_{cr} = \frac{\pi EI}{(\beta l)^2} \tag{4.7}$$

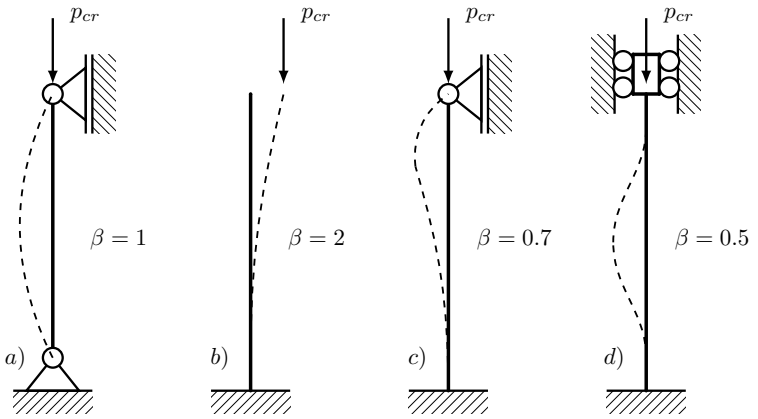

Figure 4.4: Euler column buckling shapes, inspired by K. Runesson et al.[31].

Despite Euler's column buckling formula being related to simple columns, it can be utilised in more advanced structural systems as well[31]. When analysing frameworks or continuous

beams, the buckling formula can be used on a single member extracted from the larger system.

4.1.2 Instability of a structure in 2D

The following section introduces the non-linear instability phenomenon in a two-dimensional system[34]. The system involves two bars in a low rise two-pinned triangle structure, as seen in fig. 4.5a, where the distance a is considerably smaller than b. The stiffness of the bars is equal to EA, and the system is subjected to a load f downwards, causing compression stress in the bars. Whilst in compression, the node subjected to the load will be displaced vertically by a distance u. Let l_0 and l denote the initial and the current length of a bar, respectively. The non-dimensional engineering strain ε_E is defined in eq. (4.8)[34].

$$\varepsilon_E = \frac{l - l_0}{l_0} \simeq \frac{a}{l_0}\frac{u}{l_0} + \frac{1}{2}\left(\frac{u}{l_0}\right)^2 \tag{4.8}$$

The right-hand side of the equation consists of one linear and one non-linear term, which makes the function of strain behave non-linearly in relation to the displacement. The expression also shows that if the displacement u is much smaller than the length l_0, a linear approximation is viable, but the fact that the structure behaves in a non-linear manner is clear[34].

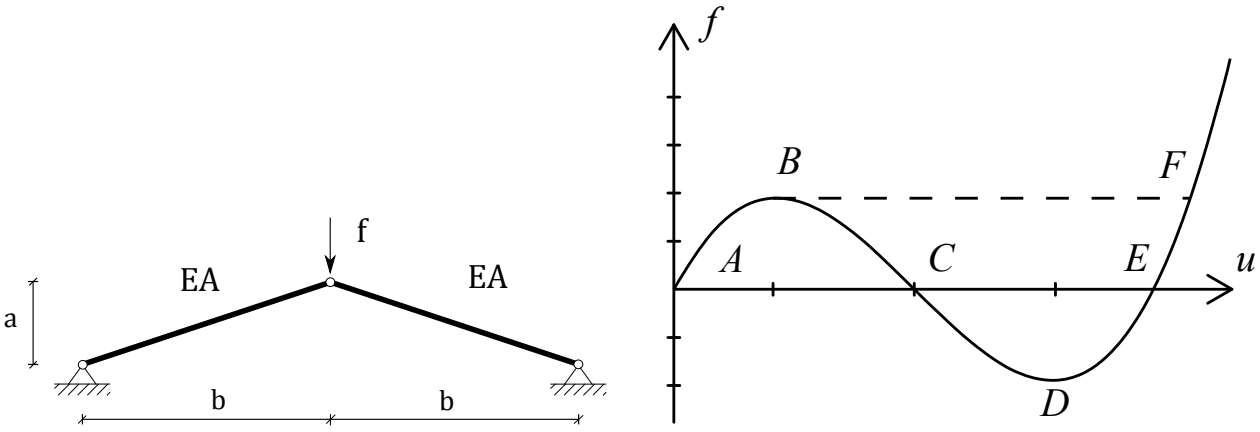

(a) 2D bar system **(b)** Force-displacement curve

Figure 4.5: Example of a 2D bar system with corresponding response curve, inspired by S. Krenk[34].

With the non-linear behaviour introduced, the entire displacement history in terms of force is presented in fig. 4.5b. The non-linearity is prominent, but what is even more interesting is the limit point B, where the load starts decreasing. The structure is losing its stiffness which allows for increasing deformations. At point C, the structure is horizontal and will continue to deform to a downwards inverted shape with stretched bars.

By looking at this behaviour in practice, this means that the load on the structure will continue deform the geometry without any greater effort until it reaches point F. This instability phenomena is known as a snap-through, i.e. the change in geometry is sudden as can be recalled from fig. 4.1g. Particularly, these types of instability issues involving a limit point are of greater significance in shell structures[31].

4.1.3 Instability of a structure in 3D

The previous section explained instability in 2D by introducing the limit point and snap-through phenomena. When looking in a 3-dimensional space, new challenges arise regarding structural imperfection. To explain this, a similar triangular structure is introduced as in fig. 4.6, but this time, the length a is no longer significantly smaller than b, which reduces the risk of snap-through. The top node needs to be stabilised laterally by an arbitrary stiffness in order to avoid a direct mechanism, explaining the spring shown in fig. 4.6. An initial lateral imperfection c is introduced, but is initially equal to zero.

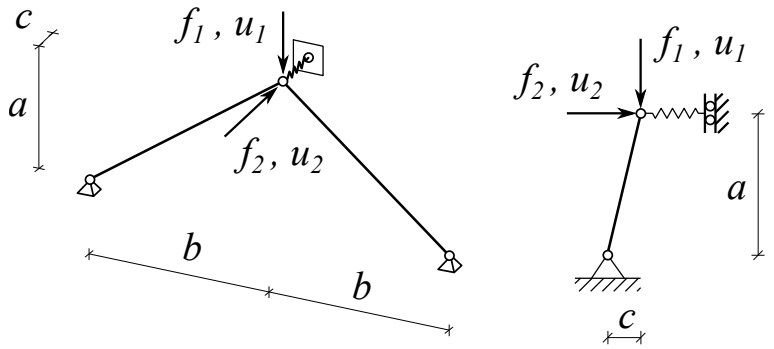

Figure 4.6: Two-elemement truss in 3D, inspired by S. Krenk[34].

$$(2\varepsilon_G + \kappa)v_2 = 0 \tag{4.9}$$

A new state of equilibrium in terms of strain is derived and shown in eq. (4.9)[34], which leaves two solutions: either the lateral displacement v_2 or the parenthesis $(2\varepsilon_G + \kappa)$ is equal to zero. The first case corresponds to a perfect symmetry and causes the snap-through behaviour reviewed earlier. The second case corresponds to a non-symmetric solution and means that the structure undergoes a lateral displacement[34]. The various possible paths are shown in fig. 4.7, where point B to D' and D" corresponds to the paths for the non-symmetric solution.

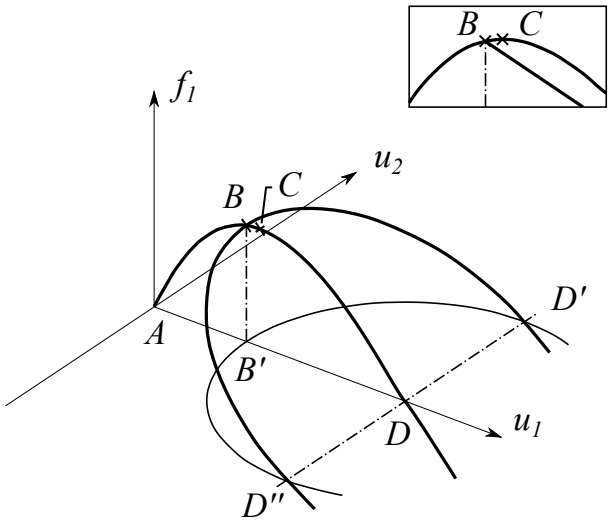

Figure 4.7: Load paths in a 3D-system, inspired by S. Krenk[34].

The point where the structure undergoes lateral displacement is known as the bifurcation point and can, depending on the stiffness, be located before or after the limit point[34]. This concludes the instability of a perfect 3D-dimensional bar structure, i.e. $c = 0$. If the top node is displaced initially, the limit point cannot be reached[34], but with smaller imperfections, close to perfect symmetry, the paths are similar to those presented in fig. 4.7, which is why the perfect symmetry gives useful information of a stability issue in 3D[34].

4.2 Buckling of continuous shells

The following section regards buckling of a continuous shell structure, based on shell formulas previously presented. A shell element with thickness t and curvature R will, according to elastic buckling theory, undergo buckling at the stress level given in eq. (4.10), with the corresponding buckling pressure load equation p_{cr}. The equation was originally derived by Zoelly back in 1915 and is in fact the same buckling stress formula given for cylindrical shells under axial pressure[29][28][35].

$$\sigma_{cr} = \frac{E}{\sqrt{3(1-v^2)}} \frac{t}{R} \tag{4.10}$$

Samuelson and Eggwertz[28] ensure the validity to be within certain limits: the ratio R/t should be below 3000 and a parameter β, defined in eq. (4.11), should be in the interval 7 to 50. The angle φ_0 in the equation is the maximum central angle of the dome, i.e. the angle from its apex to the supports.

$$\beta = \sqrt{2\varphi_0 \frac{R}{t}} \tag{4.11}$$

The corresponding buckling pressure, p_{cr}, is derived using the relation found in eq. (3.12) back in the previous chapter, and gives the expression found in eq. (4.12).

$$p_{cr} = \frac{2E}{\sqrt{3(1-v^2)}} \left(\frac{t}{R}\right)^2 = k \cdot E \left(\frac{t}{R}\right)^2 \tag{4.12}$$

If linear buckling is considered, the buckling load is determined according to eq. (4.12). Timoshenko[29] and Samuelson et al.[28] further state that the value gained from the elastic buckling pressure formula is significantly overestimated and therefore unsafe, as this seldom or never will be the case in reality. This statement is also emphasised by Williams[16], as was mentioned back in the previous chapter. The reason is due to its extreme sensitivity to imperfections, which results in a sudden collapse[29]. Several experiments also seem to be widely scattered along a spectra of critical pressures.

In order to deal with non-linear behaviour of shells, suggestions, based on experiments, have been made on how the buckling formula can be adjusted. A simple modification is made by altering the variable k in eq. (4.12). Douglas Wright has provided a collection of results from old experiments, primarily based on smaller spherical caps made of steel and aluminium. Some experiments performed by von Karman/Tsien suggest a lower bound of $k = 0.366$[2]. Some data has shown even lower results, which according to Wright, consists of samples with clear initial imperfections[2]. Results regarding almost perfect shaped shells show an average of $k = 0.7$[2].

In addition, Timoshenko[29] suggests a modified equation of the buckling pressure, presented in eq. (4.13).

$$p_{cr} = \left(1 - 0.175\frac{\varphi^\circ - 20^\circ}{20^\circ}\right)\left(1 - \frac{0.07R/t}{400}\right) 0.3E \left(\frac{t}{R}\right)^2 \tag{4.13}$$

4.3 Buckling analysis and numerical methods

With the theory of the general instability and buckling reviewed, this section introduces the methods used when analysing these behaviours. Before doing so, it should be noted that the software Abaqus, a finite element software with numerical solution methods, was used in the analysis. The major part of the theory behind finite element method is outside the scope of

this thesis, but the analysis depends heavily on the stiffness matrices, and therefore, a brief introduction to the finite element method is necessary.

A state of equilibrium in terms of loads $\boldsymbol{f}$, displacements $\boldsymbol{a}$ and stiffness $\boldsymbol{K_t}$ is expressed in eq. (4.14). The first order theory only involves the stiffness of the initial system ($\boldsymbol{K_t} = \boldsymbol{K_0}$), i.e. it is independent of both forces and deformation, and instead relies on the material properties and geometry of the structure. The stiffness matrix, $\boldsymbol{K_t}$, will continue to develop when the effects of the other levels of theory are introduced.

$$\boldsymbol{K_t a} = \boldsymbol{f} \tag{4.14}$$

4.3.1 Methods of second order theory

This short theory introduction is, if nothing else is mentioned, based on the works of Persson[36] and Krenk[34]. The second order theory includes the impact of the loads on the structure, which is done by introducing the matrix $\boldsymbol{K_\sigma}$. The total stiffness of the second order system is written,

$$\boldsymbol{K_t} = \boldsymbol{K_0} + \boldsymbol{K_\sigma} \tag{4.15}$$

where $\boldsymbol{K_t}$ is the tangential stiffness matrix. The point of second order theory is to calculate the loads that cause the structural instability, and the buckling mode shape associated with each corresponding load case. This is done by calculating the displacements, $\boldsymbol{a}$, when the tangent stiffness becomes zero according to eq. (4.16)

$$\boldsymbol{K_t a} = \boldsymbol{0} \tag{4.16}$$

The buckling loads are solved by formulating this as an eigenvalue problem,

$$(\boldsymbol{K_0} + \lambda_i \boldsymbol{K_\sigma})\boldsymbol{x}_i = \boldsymbol{0} \tag{4.17}$$

where λ_i is the eigenvalue, or the load multiplier. The buckling load, calculated in Abaqus, will therefore be the eigenvalue multiplied by the initial load. The vector $\boldsymbol{x}_i$ contains the buckling mode shape of each corresponding eigenvalue. Finding the eigenvalue and its mode shape is an iterative process, and one of the methods Abaqus uses is Lanczos Algorithm[37].

4.3.2 Methods of third order theory

Finally, third order theory includes the impact of the deformations as well. This is done by increasing the load in small steps until failure is reached, updating the stiffness of the system to account for the changes created by the deformation. This is done to calculate the actual load-bearing capacity, and it is written

$$\boldsymbol{K_t} = \boldsymbol{K_0} + \boldsymbol{K_\sigma} + \boldsymbol{K_u} \tag{4.18}$$

Several algorithms can be used to trace the non-linear equilibrium path. A common method is Newton-Raphson, which is based on iterations of small load- or displacement-increments[34]. There are several problems with this method, the most significant being that it tends to miss important points, such as the limit point or the bifurcation point[34][38].

In order to deal with this issue, various arc-methods have been developed, originally introduced by Riks[34]. The idea is to combine the iterative equilibrium of Newton-Raphson method with additional constraint that limits the distance to the next step on the equilibrium path. A version of the Riks method is implemented in Abaqus, defined as the *modified Riks* algorithm[39].

4.4 Buckling of reticulated shells

4.4.1 Background

This section aims to review the current research into buckling of reticulated shells. The purpose is to reduce the scope of the analysis by removing buckling-prone dome geometries. The January 1963 collapse of the large span dome in Bucharest, the roof structure of the National Economy Exhibition Pavilion[2], sparked the interest of many researchers, but design guidelines are still limited in comparison to other, more commonly used, structural systems. It is thus necessary to conduct a thorough investigation into the possible modes of failure when designing a dome.

4.4.2 Instability modes

There are five distinct failure modes of reticulated shells as was outlined by Gioncu[38] and they are shown in figures 4.8a-4.8e. These are: member buckling, node instability, torsional node instability, general instability, as well as combined member and node buckling[38].

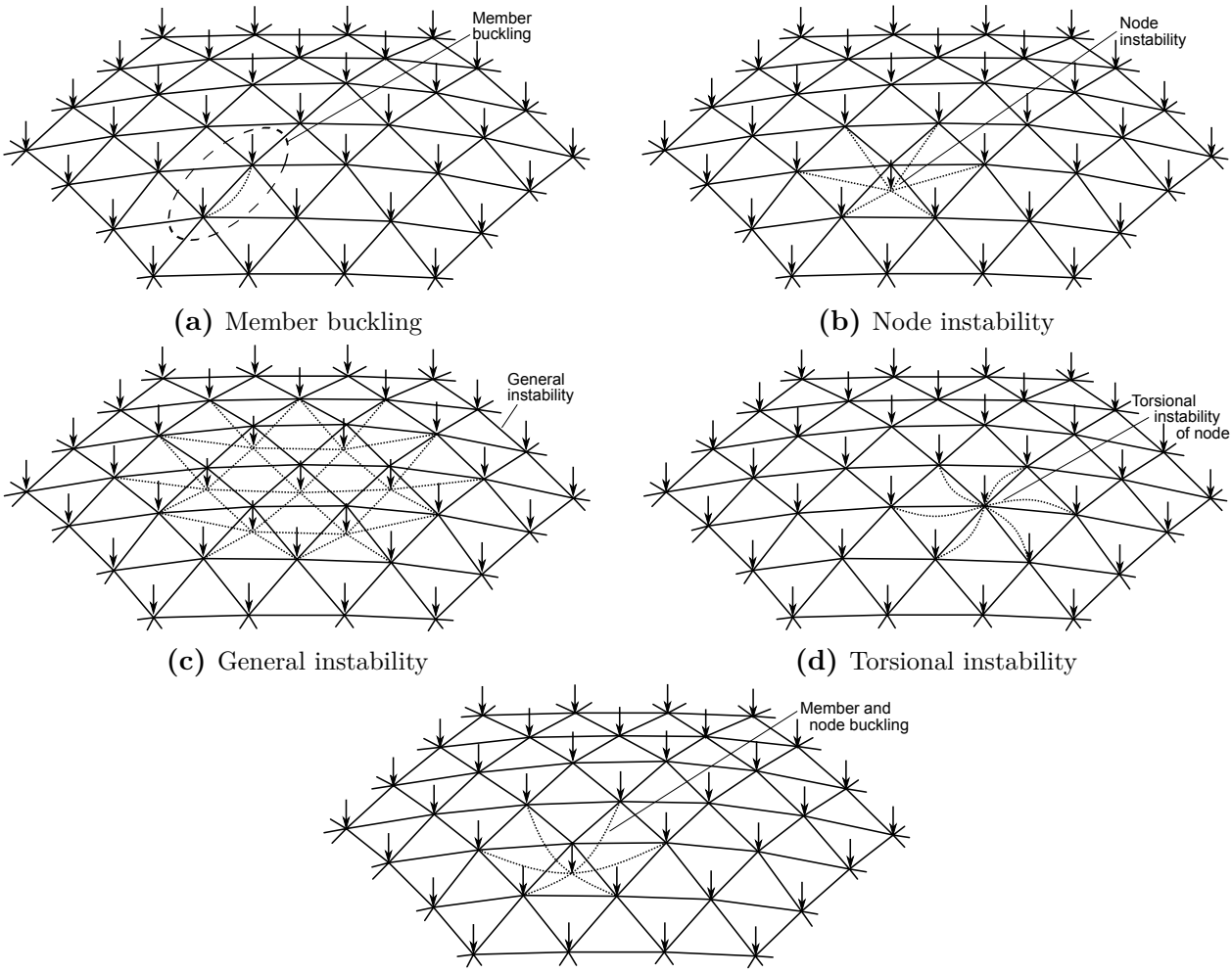

(a) Member buckling

(b) Node instability

(c) General instability

(d) Torsional instability

(e) Member and node buckling

Figure 4.8: The five distinct failure modes, inspired by V. Gioncu[38].

The seemingly most simple form of instability is member buckling, seen in fig. 4.8a, where a single member loses stability without affecting surrounding members. Gioncu[38] states that design of members still is a problem that remains, and the reason for this issue is the difficulty of identifying the most critical member given the large number of elements.

Node buckling initiates when the axial strain of all members connected to a node becomes too large, making them unable to carry any external load. This behaviour is seen in fig. 4.8b. Wright[2] argues that node buckling will only occur if the connection between members is pinned, stating that the phenomenon should disappear completely if the connection is fixed. Node instability can theoretically be studied in isolation, which can be seen in fig. 4.9. Elastic springs are introduced in figure a) to simulate the stiffness of the removed bars in b). Simplifying the structural system in that way should be avoided according to Gioncu[38], the reason why will be explained below.

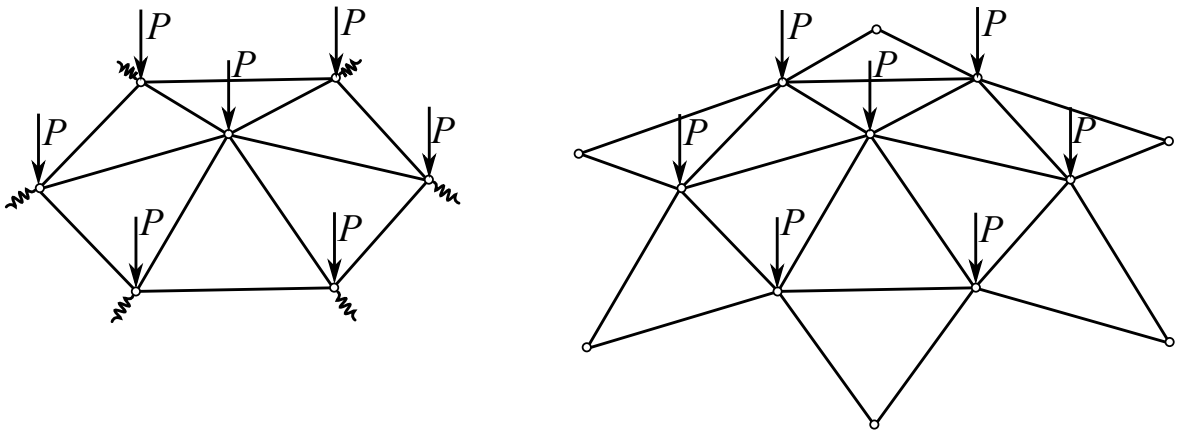

(a) Cell type with springs **(b)** Cell type without springs

Figure 4.9: Cell types, with and without elastic springs, inspired by V. Gioncu[38].

The nodes exhibit snap-through buckling. Figure 4.10 shows the different snap-through buckling modes depending on which type, and the size, of the cell analysed. Gioncu concluded that the larger cell is more susceptible to this buckling type[38]. If enough computational power exists, it is preferable to include as much of the reticulated shell in the analysis as possible. This should reduce the likelihood of error, as an introduction of elastic springs is dependent on the knowledge of their stiffness, and thus making it more likely to find the lower limit load for node buckling. The size effect can be seen in fig. 4.11.

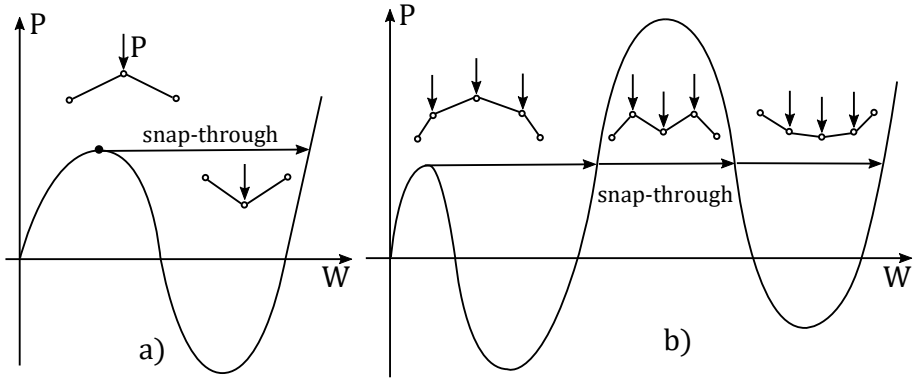

Figure 4.10: Snap-through buckling buckling modes for different cell sizes, inspired by V. Gioncu[38].

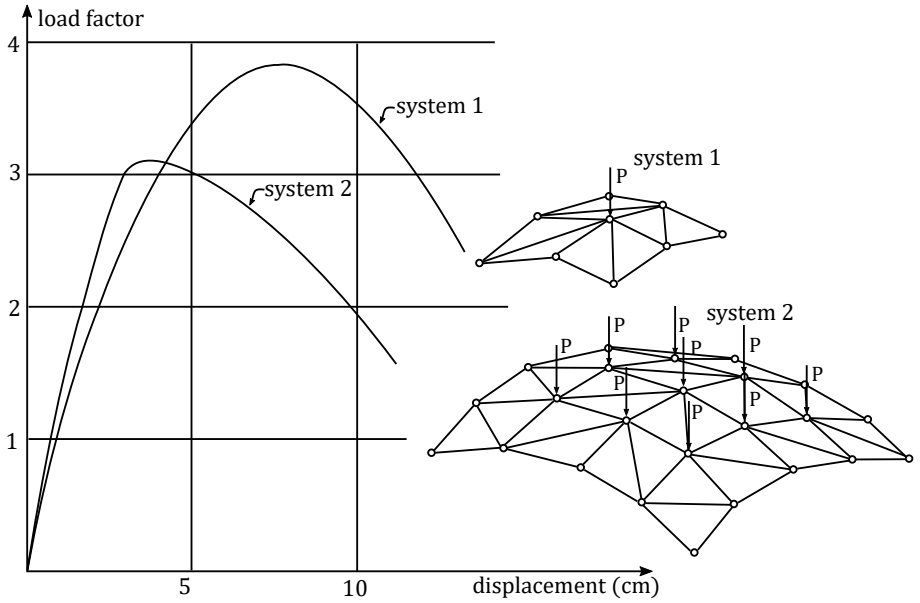

Figure 4.11: The decrease in load factor with network size, inspired by V. Gioncu[38].

Torsional instability, see fig. 4.8d, can be a problem if the joint itself is very rigid in bending around the principle axis in comparison to the out of plane direction rigidity of the members[40]. This can then cause the node to rotate and initiate torsional buckling[38][41].

The general instability mode occurs when all the nodes and members in a large section of the shell structure buckle simultaneously, see fig. 4.8c. This takes place when the critical length is greater than the individual length of each member involved[38].

The final mode is the member and node buckling that can be seen in fig. 4.8e, which is a coupled instability mode. This occurs if the member and node instability modes share critical values, or values that are in close proximity. The slenderness parameter S, defined in eq. (4.19), can also be used to determine whether the coupled instability phenomenon might occur[38]. The combined member and node instability is more likely to happen when S has a value close to 3. Gioncu[38] suggests that the designer should increase the stiffness of the hoop members, normally in tension, in dome structures to limit this interaction, even if the forces in those elements are quite low.

$$S = \frac{L}{\sqrt{R}} \cdot \sqrt[4]{\frac{K}{D}} \tag{4.19}$$

R Dome radius
L Typical member length
K Equivalent stretching rigidity
D Equivalent bending rigidity

4.4.3 Causes of failure modes

After concluding how a reticulated shell can fail, it then becomes important to discuss the causes for these failure modes. The next section covers the effect of geometrical imperfections, the dome pattern, height to span ratio, non-linear behaviour, network density, boundary conditions, and creep.

Imperfections

Only geometrical imperfections will be discussed below. Other types of structural imperfections include[42]:

- loading imperfections,
- structural imperfections, varying cross-section due to tolerances in production,
- system imperfections, different stiffness in connections than assumed e.g. semi-rigid joints instead of perfectly fixed

Gioncu states that solid shells are sensitive to geometric imperfections[38]. The question is whether this is true for reticulated shells as well, and how to model such imperfections appropriately if that is the case. As there is very little data available on the construction errors in dome-type structures, one must find a way to incorporate reasonable values into the model. Imperfections can be applied in many ways, a few of the available methods are listed below.

- **Random initial node imperfections**
  Random imperfections can be introduced at a global level following a Gaussian shape, using construction tolerances to scale the imperfections to size[43]. It can also be done at a member level to simulate initual curvature, where the member axis rotation can be randomly generated in combination with the size of the maximum deflection as proposed by Fan et al[44].
- **Scaling linear displacement**
  This is done by calculating the linear displacement of the studied load case, including the self-weight of the structure.[42].
- **Eigenmodes**
  A commonly used method is to impose the imperfection in the shape of an eigenmode. This can be done either using single modes, or combining several[43]. Many researchers[45][42][46] have found that the it is not always the first mode that yields the worst response, it could instead be the linear combination of several base shapes or simply a higher eigenmode. The eigenvalue problem is defined in section 4.3.1 eq. (4.17).

- **Displacement to a subset of the nodes**
  A simple method, proposed and studied by Gidófalvy and Katula[41], is to randomly introduce vertical displacement to a subset of the nodes. This method does however result in a lower reduction rate, and thus a higher remaining capacity, than all the other methods on this list.

In each of the methods the imperfection needs a metric value added to the dimensionless shape. However, there does not exist much guidance on the size of the geometrical imperfections in dome structures, apart from $3.0D/1000$ suggested in the Chinese code for reticulated steel shells according to Zhou et al[47]. It is thus often necessary to conduct a parameter study regarding the sensitivity to imperfections, which was done in the following articles:[41][42][48][46][47][44].

Dome pattern

The domes in table 4.1 are compared in terms of strength and rigidity. From the figure it appears that a geodesic member distribution is superior in both. However, the available research seldom includes any direct strength comparison between different geometries, even though these exact numbers, possibly from the same source, are present in several publications[22][17][49].

Table 4.1: Strength and rigidty for four types of domes[17]

Dome Type	Strength [-]	Rigidity [-]
Geodesic	100	100
Lattice	50	54
Kiewitt	70	100
Schwedler	30	5

Height to span ratio

It appears that a height to span ratio of 0.3 is the obvious choice after looking at table 3.1. But it is perhaps an overly simplistic conclusion, this because the different ways of creating the dome geometry are important when it comes to height to span ratio. Lüning[22] states that a ratio of 0.2 is preferable if the geodesic geometry is based on tilting planes. He states that it is better to use a geodesic configuration based on the icosahedron if the design requires an increased ratio above 0.2. Any strength comparison between different geodesic domes is not offered, hence further investigation is required. In contrast, Pan and Girhammar[23] state that a ratio between 0.23 and 0.38 is acceptable, 0.29 being ideal[23], and that the designer should avoid a relationship that falls below 0.16. This is when the relative buckling pressure falls below 1.0, seen in fig. 4.12.

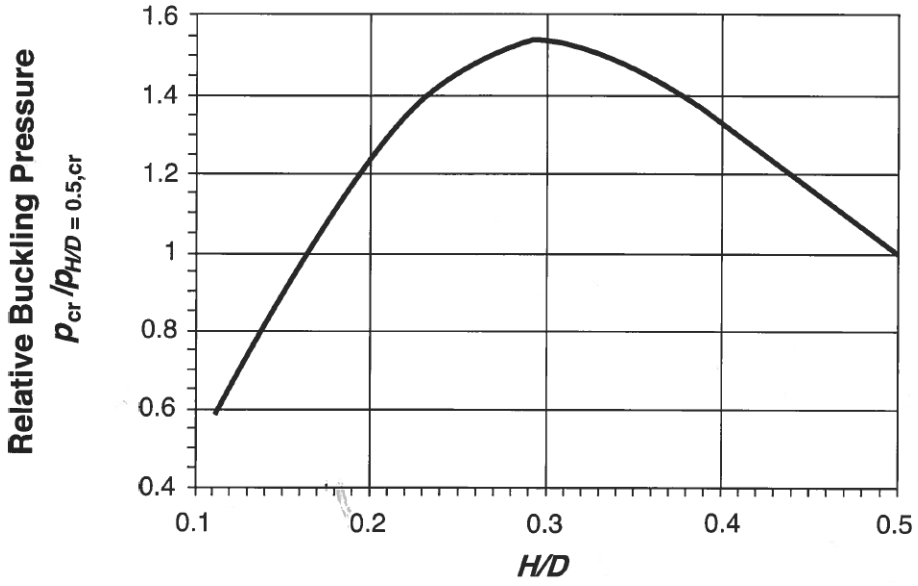

Figure 4.12: Height to diameter ratio and relative maximum buckling pressure, from D.H. and U.A. Girhammar[23].

Non-Linearity

In fig. 4.13 the sensitivity to material and geometrical non-linearity is shown on the x, and y axes, respectively. Notably, the analysis of single-layer reticulated shells needs to include geometric non-linearity, a point which is strongly emphasised by Gioncu[38]. The effect of geometrical non-linearity is also the dominating factor for larger spans, which certainly applies to a span of 300 meters.

The discrepancy between linear and non-linear analysis is shown in fig. 4.14 using the slenderness parameter S[50][38]. It can be seen that the ratio between the linear and non-linear buckling load is in the range of 1.3 to 1.6, depending on the value of S.

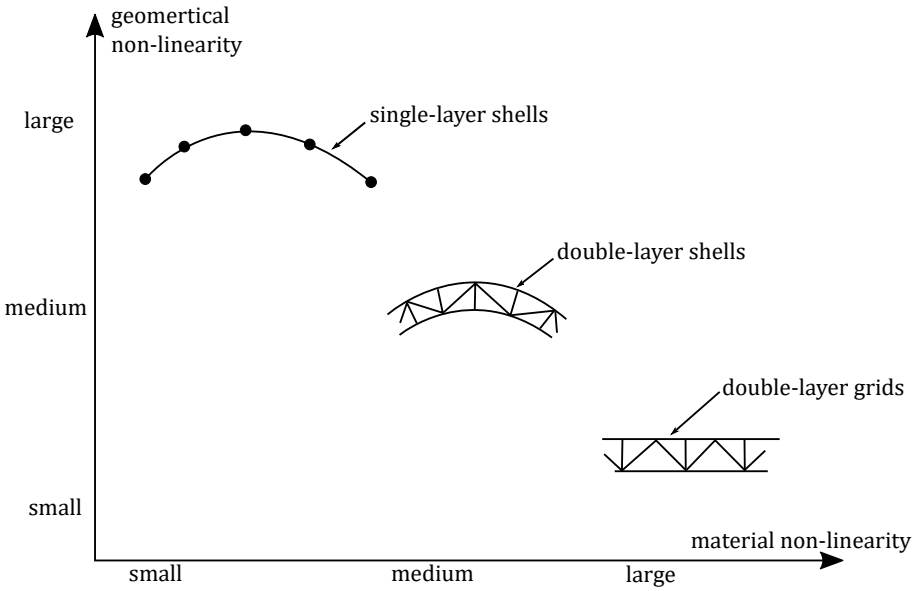

Figure 4.13: The effects of non-linearity depending type of shell, inspired by V. Gioncu[38].

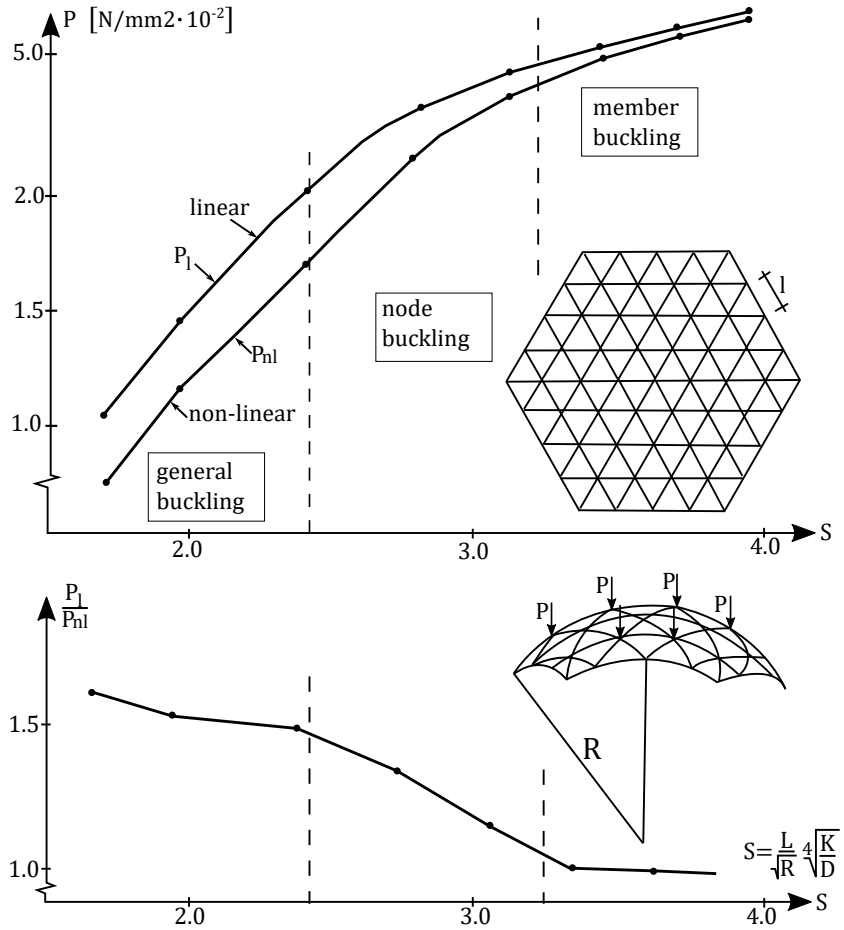

Figure 4.14: Linear elastic and geometric non-linearity compared, inspired by V. Gioncu[38].

The slenderness parameter also corresponds to different forms of buckling. Perhaps the limit point where S equals 3 is worth mentioning. Values above indicate member buckling, while a lower value suggests node or general buckling.

Mesh Density

Another important aspect when designing a dome structure is the maximum member length, or the mesh density of the shell. Gioncu[38] argues that the stiffness is reduced, which of course means the buckling load is reduced as well, if the network density is increased. The point is further emphasised by fig. 4.14, where one can see that the critical load increases with an increasing slenderness parameter (S). Meaning, the shell will increase the load-bearing capacity the more sparse the mesh.

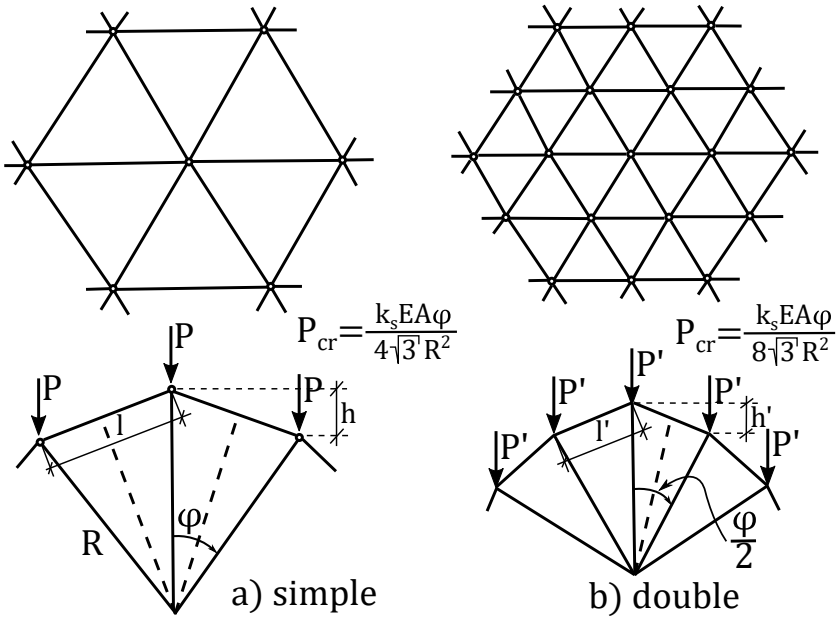

Figure 4.15: The effect of grid density, inspired by V. Gioncu[38].

The opposite is stated by Pan and Girhammar[23]. They introduce a relative timber volume parameter, defined as

$$V_{rel} = \frac{V_{n,m,k}}{V_{n,m,k=10}} \tag{4.20}$$

n	Number of sectors
m	Division of arc length
k	Division of bottom ring length
$V_{n,m,k}$	Volume of timber for a dome with a certain mesh density,

i.e., a combination of n, m and k
$V_{n,m,k=10}$ The maximum value of timber, when n=m=k=10

Using the relative timber volume parameter, V_{rel}, they showed that the buckling capacity increases with increasing mesh density. This relationship can be seen in fig. 4.16. They further conclude that an increase in mesh density improves the overall behaviour of the dome in terms of relative maximum deflection and bending moment.

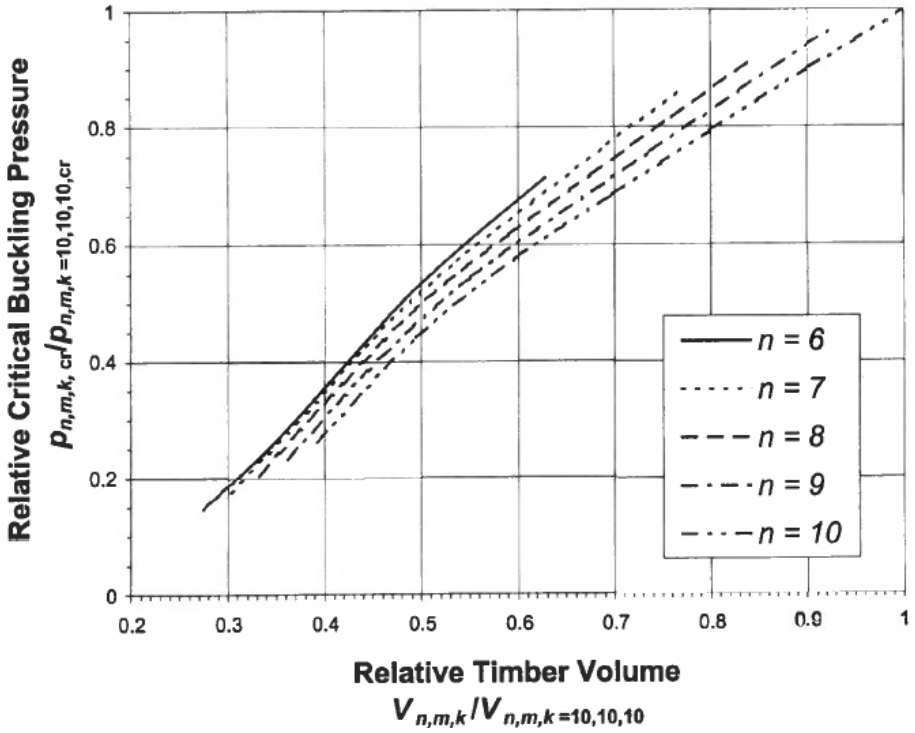

Figure 4.16: The relationship between the relative timber volume and the relative critical buckling pressure, from D.H. Pan and U.A. Girhammar[23].

The mesh density was studied in order to determine how it relates to the critical load and the maximum stress, see section 7.3.1.

Boundary Conditions

Boundary conditions also play a significant role on the buckling load and behaviour, see fig. 4.17. The shell with a full pinned boundary buckles globally, whereas the shell with roller supports buckles locally. However, the buckling loads are much larger when using pinned connections.

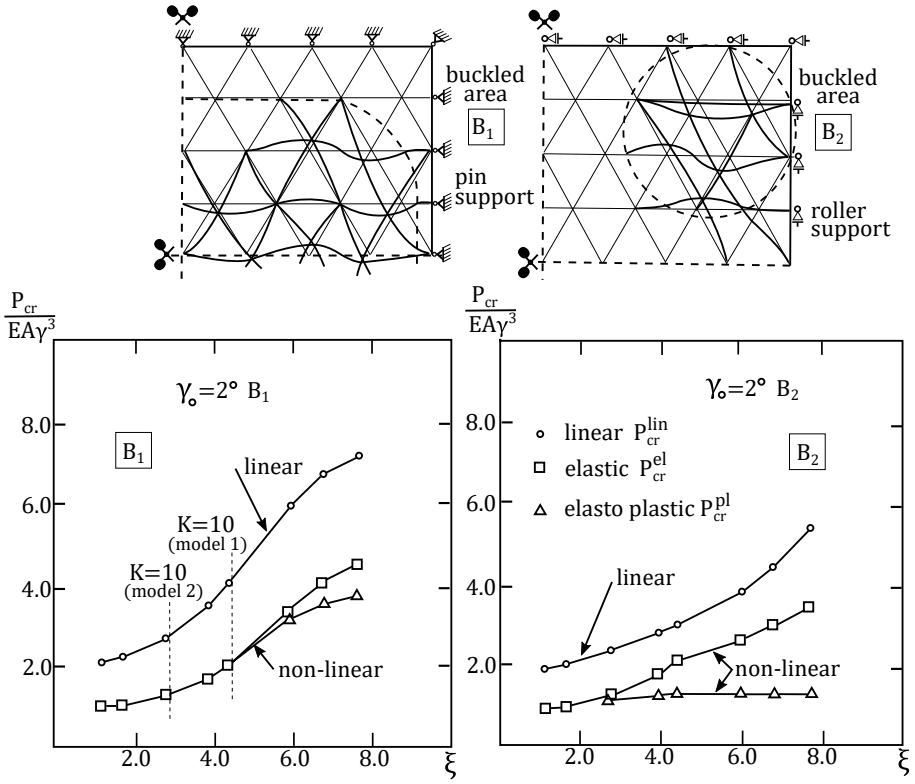

Figure 4.17: The effect of critical load when pinned or roller supports are used, inspired by V. Gioncu[38].

Creep

Creep reduces the buckling load of timber structures. Zhou et al.[47] show the effect of creep in relation to the load level, see fig. 4.18. The figure shows that the load level cannot exceed 35 % of the instant non-linear buckling load of the reticulated shell, if a service life of 50 years or more is intended.

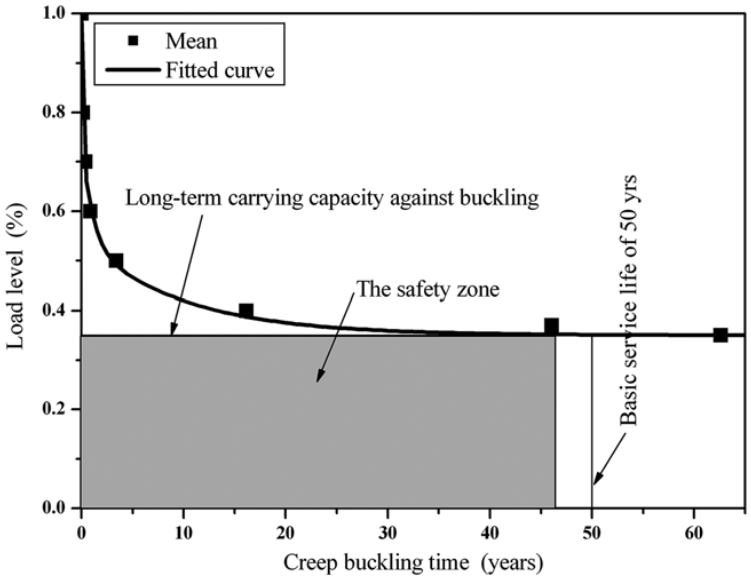

Figure 4.18: Buckling load level versus time, from H.Z. Zhou et al.[47].

4.4.4 How to analyse buckling of a reticulated dome

A method that is employed by many researchers is to study the load deflection curve [44][48][51][52][53][54][55][56][57][58][59], sometimes referred to as the nonlinear equilibrium path, of one or several nodes. This method allows one to clearly see when the structure loses stability, and it also allows the study into the effects of initial imperfections.

Software

A brief study of the software used by researchers has been performed. Many choose to implement their own finite element routine, while a few use commercially available software. The two most commonly used commercial programs were Abaqus[47][60][56][58] and ANSYS[51][48][44][57].

4.4.5 Determining buckling loads by hand calculation

The following section is a review of the hand approach of determining buckling loads in a reticulated dome. The formulae are derived by Douglas T. Wright[2].

Member buckling

The member buckling load is determined according to eq. (4.21), and works seemingly well even for rigid nodes[2]. Remark that the buckling load $p_{cr,member}$ is oriented radially, i.e. a pressure load. This may cause a small deviation in comparison to actual vertical load.

$$p_{cr,member} = \frac{2\sqrt{3} \cdot \pi^2 \cdot EI}{Rl^3} \quad [\mathrm{N/m^2}] \tag{4.21}$$

R	Spherical radius
l	Length of an individual member

Nodal buckling

The nodal buckling is limited within a bound, since it widely depends on the flexibility of the system as a whole.

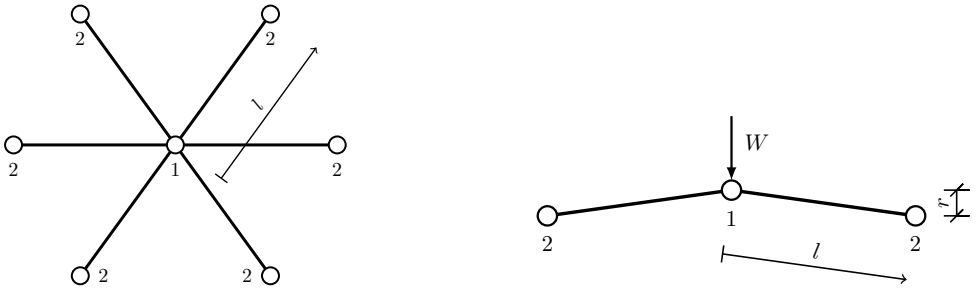

(a) Seen from above **(b)** Seen from the side

Figure 4.19: Elements involved in nodal buckling.

The upper bound is considering the pinned joints marked '2' in fig. 4.19 to all be inextensible for movement. The nodal buckling force, in terms of concentrated force, W_{cr}, is determined according to eq. (4.22).

$$W_{cr} = \frac{2AEr}{\sqrt{3}\ l^3}, \quad [\mathrm{N}] \tag{4.22}$$

The nodal load shown in eq. (4.22) corresponds to a uniformly distributed load seen in eq. (4.23).

$$p_{cr} = \frac{A\ E\ l}{6\ R^3} \quad [\mathrm{N/m^2}] \tag{4.23}$$

It is however inevitable that the nodal buckling will be lower, as long as only pinned connections are concerned[2]. A lower bound is introduced to take account for extensible members. The concentrated force needed is introduced in eq. (4.24).

$$W_{cr} = \frac{AEr}{\sqrt{3}\ l^3}, \quad [\mathrm{N}] \tag{4.24}$$

And thus the limit for the nodal buckling load is summarized in eq. (4.25).

$$\frac{AEl}{12R^3} \leq p_{cr,nodal} \leq \frac{AEl}{6R^3} \tag{4.25}$$

Global buckling

Determining the global buckling of a reticulated dome is done with help of continuous shell analogy. Therefore, the global buckling is based on the linear buckling formula for a continuous shell, seen in eq. (4.26).

$$p_{cr} = k \cdot E' \left(\frac{t'}{R}\right)^2 \tag{4.26}$$

While eq. (4.26) looks similar to its origin eq. (4.12), its thickness, t', and Young's modulus, E', are reduced to account for a reticulated shell. Young's modulus is reduced according to eq. (4.27)[2].

$$E' = \frac{2AE}{\sqrt{3}lt'} \tag{4.27}$$

Where the thickness t' is determined in eq. (4.28)[2]. Note that for massive cross sections, the thickness remains unchanged.

$$t' = 2\sqrt{3}\sqrt{\frac{I}{A}} \tag{4.28}$$

Just as for continuous shells, to account for non-linearity in elastic buckling load, the variable, k, should be adjusted. Without further research on reticulated shells specifically, Wright proposes a k-value of 0.4, based on an assumption that a reticulated shell should behave seemingly well[2].

Chapter 5

Preliminary Design

Prior to the analysis, a dome with a span of 300 m was preliminary designed using various calculation methods: One where the necessary cross section area was approximated by help of formulas of an arch, and the other by use of shell analogy. The capacity of the cross section was checked according to Eurocode 5: Design of timber structures – Part 1-1: General – Common rules and rules for buildings.

The estimations used should be applicable to any dome geometry. The formulas were however calculated with the Geodesic dome in mind, which made some geometrical parameters unique to this very case. The following assumptions were made prior to the calculations:

- Design load: $q_{d,tot} = g_d + q_d = 2 + 2 = 4$ kN/m^2
- Diameter, $D = 300$ m, rise, $H = 90$ m, spherical, radius $R = 170$ m
- The length of a beam in the grid was up to 20 m long. The median length was 18 m. See chapter 7 for a thorough member distribution comparison.
- Approximated influential width on reticulated surface: $a = 13.6$ m near apex and base. $a = 15.5$ m midway.
- Beams are braced laterally by the roof sheeting, i.e. restricted against bending in their weak axis
- Connections are assumed to be rigid

5.1 Arch stress relation

By using a stress formula based on the horizontal forces in an arch, a comparison with the coal depot dome in Brindisi was made. The formula is presented in eq. (5.1)[61].

$$\sigma = \frac{qD^2}{8HA} \tag{5.1}$$

q	uniformly distributed line load [kN/m]
D	span of an arch (Diameter of a dome) [m]
H	rise [m]
A	cross section area [m^2]

Based on information from the timber domes in Brindisi, a relation in terms of normal stress of an arch with similar geometry was performed.

Essential information about the Brindisi dome were as following:

- Design load: $q_{d,Brsi} = g_d + q_d = 1 + 0.6 = 1.6$ kN/m^2
- Diameter, $D_{Brsi} = 143$ m, rise, $H_{Brsi} = 39$ m
- Cross section: $A_{Brsi} = w \times h = 0.18 \cdot 1.13 = 0.2$ m^2

In order to achieve a similar stress level for a larger dome/arch, a relation based on eq. (5.1) was set up to determine the required cross-sectional area A, which was done in eq. (5.2) through (5.4).

$$\sigma = \sigma_{Brsi} \quad \longrightarrow \quad \frac{qD^2}{8HA} = \frac{q_{Brsi}D_{Brsi}^2}{8H_{Brsi}A_{Brsi}} \tag{5.2}$$

$$A = \frac{qD^2}{q_{Brsi}D_{Brsi}^2} \cdot \frac{H_{Brsi}A_{Brsi}}{H} \tag{5.3}$$

$$A = \frac{5 \cdot 300^2}{1.6 \cdot 143^2} \cdot \frac{39 \cdot 0.2}{90} = 1.19 \text{ m}^2 \tag{5.4}$$

The cross section area needed was estimated to 1.19 m^2. The massive beam dimension was chosen to $w \times h = 0.8 \times 1.6$ m^2, which corresponds to an area of 1.28 m^2. The increase in area was to create a safety margin.

5.2 Continuous shell analogy

5.2.1 Normal force estimation

The normal force was determined through the formulas regarding membrane forces in continuous shells found in section 3.3. The normal force in a member in its meridional direction is determined by equation eq. (5.5).

$$N = T_\varphi \cdot a \tag{5.5}$$

T_φ Force along the meridian [kN/m]
a Influential area in the reticulated grid = 13.6 [m]

T_φ was determined in terms of both dead load and snow load using eq. (5.6).

$$\begin{aligned} T_{\varphi,DL} = &\quad -g_d \frac{R^2}{R+y} \qquad 0 < y < H \\ T_{\varphi,SL} = &\quad -q_d \frac{R}{2} \end{aligned} \tag{5.6}$$

$T_{\varphi,DL}$ Meridional force due to dead load = 2 [kN/m]
$T_{\varphi,SL}$ Meridional force due to uniformly imposed load = 2 [kN/m]
y Vertical distance from spherical centroid [m]

Force at the base

$$T_{\varphi,base} = T_{\varphi,base,DL} + T_{\varphi,base,SL} \tag{5.7}$$

$$\longrightarrow \quad T_{\varphi,base} = -g_d \frac{R^2}{R+(R-H)} - q_d \frac{R}{2} = -231 - 170 = -401 \text{ kN/m} \tag{5.8}$$

$$N_{base} = T_{\varphi,base} \cdot a = -401 \cdot 13.6 = -5.4 \text{ MN} \tag{5.9}$$

Force at the apex

$$T_{\varphi,apex} = -g_d \frac{R^2}{R+(R-H)} - q_d \frac{R}{2} = -170 - 170 = -340 \text{ kN/m} \tag{5.10}$$

$$N_{apex} = T_{\varphi,apex} \cdot a = -340 \cdot 13.6 = -4.6 \text{ MN} \tag{5.11}$$

5.2.2 Buckling loads

The buckling loads were calculated for the three cases mentioned in section 4.4.5: Member, nodal and global buckling.

The buckling behaviour was predicted by using the equation for the slenderness parameter in eq. (4.19) in section 4.4.1. The stretching and bending rigidity given in eq. (4.19) were assumed to correspond to the axial stiffness, EA, and the bending stiffness, EI. Furthermore, the median length of a member for a Geodesic was determined to 18 metres, see fig. 7.1 in chapter 7. This length was used in this eq. (5.12).

$$S = \frac{l}{\sqrt{R}} \cdot \sqrt[4]{\frac{K}{D}} = \frac{l}{\sqrt{R}} \cdot \sqrt[4]{\frac{EA}{EI}} = \frac{l}{\sqrt{R}} \cdot \sqrt[4]{\frac{A}{I}} = \frac{18}{\sqrt{170}} \cdot \sqrt[4]{\frac{0.8 \cdot 1.6 \cdot 12}{0.8 \cdot 1.6^3}} = 2.0 \tag{5.12}$$

The slenderness parameter calculated in eq. (5.12) was determined to 2.0, which according to fig. 4.14 in section 4.4.3, means that the dome is prone to undergo a general/global buckling.

Member buckling load

Since member buckling only concerns a single member in the system, one of the longer members in the domes were chosen for calculation. For the case of the geodesic dome, the longest member was determined to 20 metres. The member buckling load is shown in eq. (5.13).

$$q_{cr,member} = \frac{2\sqrt{3} \cdot \pi^2 \cdot EI}{Rl^3} = \frac{2\sqrt{3} \cdot \pi^2 \cdot 10.8 \cdot 10^9 \cdot 0.8 \cdot 1.6^3}{170 \cdot 20^3 \cdot 12} = 73 \text{ kN/m}^2 \tag{5.13}$$

Nodal buckling load

The nodal buckling was calculated according to eq. (5.14). The ratio 5/6 is implemented due to the five beams that connect in the apex of a Geodesic dome, as opposed to the six beams related to the equation. This modifications is later confirmed to be accurate, seen in section 8.2.

$$\frac{AEl}{12R^3} \cdot \frac{5}{6} \leq q_{cr,nodal} \leq \frac{AEl}{6R^3} \cdot \frac{5}{6} \tag{5.14}$$

$$\frac{1.28 \cdot 10.8 \cdot 10^9 \cdot 18}{12 \cdot 170^3} \cdot \frac{5}{6} = 3.5 \text{ kN/m}^2 \leq q_{cr,nodal} \leq 7.0 \text{ kN/m}^2 = \frac{1.28 \cdot 10.8 \cdot 10^9 \cdot 18}{6 \cdot 170^3} \cdot \frac{5}{6} \quad (5.15)$$

While both the upper and lower bound yielded low buckling loads, it should be remarked that eq. (5.14) regards a dome with pin-jointed connections, whereas this particular dome has rigid connections. Nodal buckling for rigid nodes will, according to theory, not occur[2]. The results from the nodal buckling is therefore disregarded until further notice, and the analysis of nodal buckling is later reviewed in section 8.2.

Global buckling load

The global buckling load was calculated using the continuous shell analogy.

$$q_{cr,global} = k \cdot E' \cdot \left(\frac{t}{R}\right)^2 \text{ [kN/m}^2\text{]} \quad (5.16)$$

To account for the reticulated grid, the Young's modulus was modified according to eq. (5.17).

$$E' = \frac{2EA}{\sqrt{3}lh} = \frac{2 \cdot 10.8 \cdot 10^9 \cdot 1.28}{\sqrt{3} \cdot 18 \cdot 1.6} = 0.554 \text{ GPa} \quad (5.17)$$

$$q_{cr,global,linear} = 1.21 \cdot 0.55 \cdot 10^9 \cdot \left(\frac{1.6}{170}\right)^2 = 59.4 \text{ kN/m}^2 \quad (5.18)$$

To account for non-linearity, variable k was set to the recommended value of 0.4, thus giving the buckling load presented in eq. (5.19).

$$q_{cr,global,non} = 0.4 \cdot 0.55 \cdot 10^9 \cdot \left(\frac{1.6}{170}\right)^2 = 19.6 \text{ kN/m}^2 \quad (5.19)$$

By use of the latter calculated buckling load, the equivalent normal buckling force in a beam near the base was calculated to eq. (5.20).

$$N_{cr,global} = \frac{q_{cr,global} \cdot R}{2} \cdot a = \frac{19.6 \cdot 10^3 \cdot 170}{2} \cdot 13.6 = 22.7 \text{ MN} \quad (5.20)$$

5.2.3 Moment estimation

The formulas for membrane forces do not account for any bending moment in the dome, and bending action in shell structures is too complex to determine analytically, as stated in section 3.1.3. A method to estimate the bending moments had to be developed, as it was assumed that asymmetrical loads and rigid connections would inevitably lead to bending moments.

The estimation was instead primarily based on the simple elementary case of a rigidly supported beam. The second order moment was assumed by consideration of imperfections similar to the mode shape given in fig. 8.1 in chapter 8.

Moment from a fixed supported beam

By assuming that the connections between the discrete grid of members are rotationally stiff, the elementary loading case, seen in fig. 5.1, was used to estimate the bending moment. In this case, a beam of the median length of 18 m was used to determine the supporting moment given in eq. (5.21).

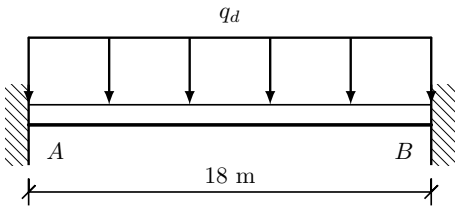

Figure 5.1: Elementary load case of fixed supports combined with line load.

$$M_A = -\frac{q_d L^2}{12} \tag{5.21}$$

An approximation of the line load along the beam was calculated by use of eq. (5.22) and was applied to eq. (5.21). The result can be seen in eq. (5.23).

$$q_d = (g + q) \cdot a = 4 \cdot 13.6 = 54.4 \text{ kN/m} \tag{5.22}$$

$$M_A = -\frac{54.4 \cdot 18^2}{12} = -1.47 \text{ MNm} \tag{5.23}$$

Second order moment due to imperfections

The normal forces near the base were estimated to 5.4 MN. A small initial imperfection will presumably add to the bending stresses. An estimation of the second order bending moment

was therefore performed. The mode shape obtained from chapter 5 in fig. 8.1 was used as the initial imperfection. A scaling factor of D/300 gives an imperfection of 0.2 metres near the base.

$$M'' = M_A + N_{Ed} \cdot e \quad [\text{MNm}] \tag{5.24}$$

$$e = e_0 \cdot \frac{1}{1 - \frac{N_{Ed}}{N_{cr}}} = 0.2 \cdot \frac{1}{1 - \frac{5.4}{22.7}} = 0.26 \text{ m} \tag{5.25}$$

$$M'' = M_A + N_{Ed} \cdot e = 1.47 + 5.4 \cdot 0.26 = 2.88 \text{ MNm} \tag{5.26}$$

5.3 Capacity

The design was made using two separate methods. The first method reduced the normal force capacity by taking the slenderness of the cross-section into account, and it also only considered the first order bending moment. The second method used the second order moment directly and it did not reduce the normal force capacity.

The dome was preliminary designed with capacity formulas from Eurocode 5[13].

Material strength

$$f_{md} = \frac{k_{mod} \cdot f_{m,k}}{\gamma_M} = \frac{0.8 \cdot 30}{1.25} = 19.2 \text{ [MPa]} \tag{5.27}$$

$$f_{cd} = \frac{k_{mod} \cdot f_{c,k}}{\gamma_M} = \frac{0.8 \cdot 24.5}{1.25} = 15.7 \text{ [MPa]} \tag{5.28}$$

$$f_{td} = \frac{k_{mod} \cdot f_{t,0,k}}{\gamma_M} = \frac{0.8 \cdot 19.5}{1.25} = 12.5 \text{ [MPa]} \tag{5.29}$$

f_d	Design value for strength parameter
$f_{m,k}$	Characteristic bending stress parallel to grain
$f_{c,k}$	Characteristic compression stress parallel to grain
$f_{t,0,k}$	Characteristic tension stress parallel to grain
k_{mod}	Modification factor taking into account the effect on

strength parameters of the duration of load and service class
γ_M Partial coefficient for material, 1.25 for glulam

Normal force capacity

$$N_{c,Rd} = f_{cd} A k_c \tag{5.30}$$

Normal force capacity without respect to slenderness reduction

$$N_{c,Rd} = 15.36 \cdot 0.8 \cdot 1.6 = 19.66 \text{ MN} \tag{5.31}$$

Normal force capacity with respect to slenderness reduction

$$\lambda_{rel} = \sqrt{\frac{f_{ck} \cdot A}{N_{cr}}} = \sqrt{\frac{24 \cdot 1.28}{22.7}} = 1.16 \tag{5.32}$$

$$k = 0.5(1 + \beta_c(\lambda_{rel} - 0.3) + \lambda_{rel}^2) = 0.5(1 + 0.1(1.16 - 0.3) + 1.16^2) = 1.22 \tag{5.33}$$

$$k_c = \frac{1}{k + \sqrt{k^2 - \lambda_{rel}^2}} = \frac{1}{1.22 + \sqrt{1.22^2 - 1.16^2}} = 0.63 \tag{5.34}$$

$$N_{c,Rd} = 15.36 \cdot 0.8 \cdot 1.6 \cdot 0.63 = 12.39 \text{ MN} \tag{5.35}$$

Moment capacity

$$M_{Rd} = f_{md} W \tag{5.36}$$

$$M_{Rd} = 19.2 \cdot \frac{0.8 \cdot 1.6^2}{6} = 6.55 \text{ MNm} \tag{5.37}$$

Combined action

The combined effect of bending moment and normal force was controlled using eq. (5.38) from Eurocode 5, both for first and second order theory.

$$\frac{M_{Ed}}{M_{Rd}} + \frac{N_{Ed}}{N_{Rd}} \leq 1 \tag{5.38}$$

First order moment regarded. Slenderness reduction taken into account:

$$\frac{1.47}{6.55} + \frac{5.4}{12.39} = 0.22 + 0.44 = 0.66 \leq 1 \tag{5.39}$$

Second order moment regarded. No slenderness reduction taken into account:

$$\frac{2.88}{6.55} + \frac{5.4}{19.66} = 0.44 + 0.27 = 0.71 \leq 1 \tag{5.40}$$

5.4 Summarised result of the preliminary design

By use of the shell analogy, the design normal force for a governing member in ultimate limit state was determined to 5.4 MN. Based on moment assumptions, the design moment for the same member was estimated to 1.5 MNm and 2.9 MNm, with and without respect to second order theory respectively.

The buckling loads were determined to 73 kN/m^2 for member buckling, 3.5-7.0 kN/m^2 for nodal and 19.6 kN/m^2 for global buckling, where the global buckling was considered to be the governing case of buckling.

The combined effect of normal force and moment showed a cross section utilisation of 0.66 and 0.71. The beam should therefore be OK in ultimate limit state, according to these hand calculations.

The chosen cross section and material properties are summarised in fig. 5.2 and table 5.1, and will be used for analysis in Dome comparison in chapter 7 and for the stability analysis in chapter 8.

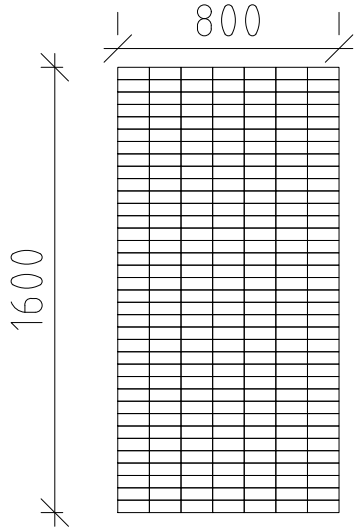

Figure 5.2: Beam dimensions 800×1600 ($w \times h$) [mm].

Table 5.1: Properties of the chosen beam cross section.

Width w [m]	0.80
Height h [m]	1.60
Area A [m^2]	1.28
Second moment of area I [m^4]	0.273
Section modulus W [m^3]	0.341
Material	GL30c
Young's modulus E [GPa]	10.8
Design strength in compression f_{cd} [MPa]	15.7
Design strength in bending f_{md} [MPa]	19.2
Design strength in tension f_{td} [MPa]	12.5

Chapter 6

Method of analysis

6.1 Geometry studied

Out of the dome patterns presented in fig. 3.2 in chapter 3, three were chosen for further study, seen in fig. 6.1.

- Kiewitt/lamella pattern with 8 sectors and 9 meridional members from the apex to the base
- Geodesic dome based on truncated icosahedron with a frequency of 11
- Three-way triangulated grid with a frequency of 10

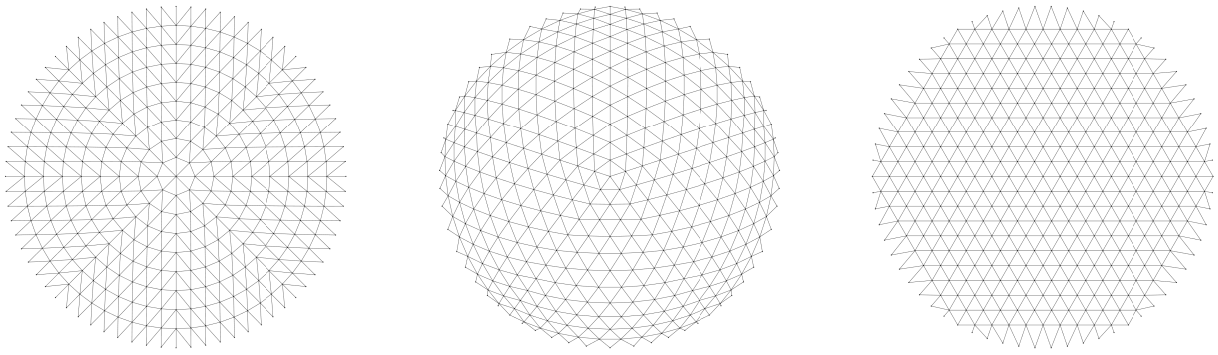

(a) Kiewitt **(b)** Geodesic **(c)** Three-way grid

Figure 6.1: Dome geometries studied.

The reasoning behind the choices of Kiewitt and Geodesic was primarily based on their strength and rigidity attributes, as presented in table 4.1. The third geometry, the three-way grid, was chosen due to lack of information about its performance.

The frequency and sectors of every pattern were chosen in order to make the comparison study between the patterns fair. Therefore, the patterns were made to make the median length of the member distribution, and their total member length nearly equal.

All domes were spherical, with a base diameter, D, of 300 meters. A rise-to-span-ratio of 0.3 was chosen based on the literature review in section 4.4.3. The height of the Kiewitt and the Three-way grid geometries was 90 metres. The Geodesic pattern had a height of 92.7 metres, due to inconvenience when projecting the surfaces from the icosahedron onto the sphere.

6.2 Analysis outline

6.2.1 Continuous shell analogy

A dome with a continuous shell was studied to understand the general behaviour of shell structures. Therefore, a numerical analysis of a continuous dome geometry was performed, and the result of the simulation was compared with hand calculations, to safeguard against numerical errors and thus increase the level of confidence in the result. The analysis was limited to studying linear and non-linear buckling.

The analysis was carried out on a shallow spherical dome with a continuous timber shell. The diameter D was set to 300 m with a rise H of 92.7 m and the thickness $t = 1.6$ m. Since the rise/span-ratio was 0.3, the spherical radius was calculated to 168.3, according to eq. (6.1).

$$R = \frac{H}{2} + \frac{D^2}{8 \cdot H} = \frac{92.7}{2} + \frac{300^2}{8 \cdot 92.7} = 167.71 \text{ m} \tag{6.1}$$

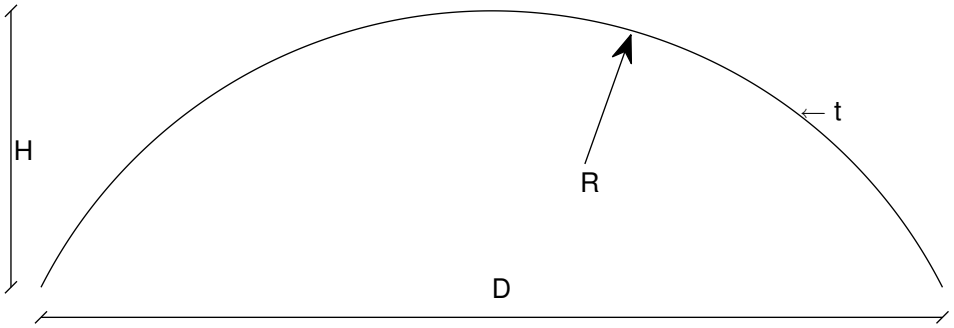

Figure 6.2: Dome geometry.

6.2.2 Local instability - snap through

One of the buckling load formulas provided by Wright[2] involved snap-through buckling of a pinned system. The buckling load formula was confirmed with numerical analysis, and checked numerically for other connection types and combinations, see fig. 6.3.

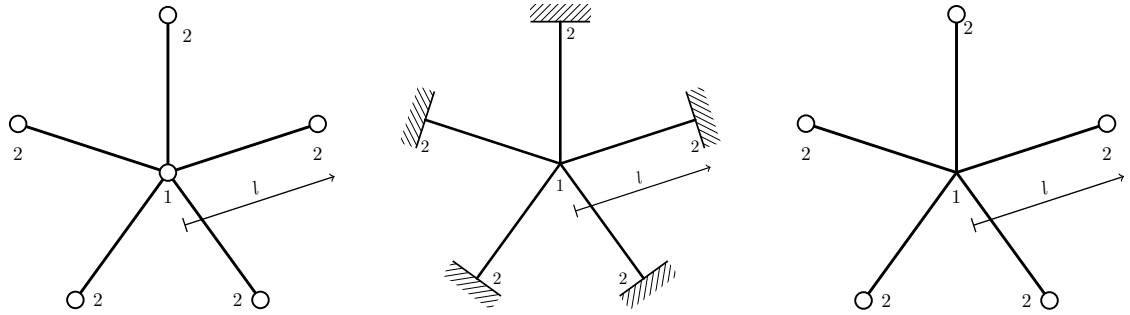

(a) Pinned connections

(b) Rigid/continuous connections

(c) Rigid mid point. Pinned base nodes.

Figure 6.3: Studied connection types at the apex of the Geodesic dome.

Consider the three cases of rigidity found in fig. 6.3. The first case consisted of only pins while the second was modelled with stiff joints. The third case was meant to represent the behaviour of the actual dome more accurately, where rotation in the pinned connection was allowed to simulate the movement of the cell within the global framework.

6.2.3 Comparing dome geometries

Three dome geometries, Kiewitt, Geodesic and the Three-way grid, were studied to find the best geometry. The comparison covered:

- distribution of member length,
- number of unique element lengths,
- linear buckling load in load cases one and two (see fig. 6.15),
- stiffness.

6.2.4 Suitable subdivision

Once the best geometry had been decided, a suitable subdivision was chosen based on the stresses developed. The subdivisions studied were: 9,10 and 11, where the subdivision number

indicates the number of elements from the apex to the base along a meridian. A second order moment induced by an initial imperfection of D/300 was used. The study included all three load cases, using a load of 2 kN/m^2 and 4 kN/m^2, for symmetrical and asymmetrical load cases, respectively.

6.2.5 Imperfections

The effect of initial imperfections on global elastic stability was studied in two ways. A broad analysis considering six imperfections in the range of D/150 to D/1000, see table 6.1, using positive and negative signs on the initial imperfection scaling factor, for the first 7 mode shapes of each load case was performed. The mode shapes used can be seen in fig. 8.5 and fig. 8.6. The aim was to study how much the linear buckling load was reduced due to the initial imperfection and the effect due to the initial imperfection and mode shape.

Table 6.1: Initial imperfections, ± indicates that each imperfection mode in fig. 8.5 and fig. 8.6 was inverted

Initial imperfection relative to span	D/150	D/300	D/375	D/500	D/750	D/1000
Initial maximum imperfection [m]	± 2.00	± 1.00	± 0.80	± 0.60	± 0.40	± 0.30

The effect of initial imperfections on the stiffness of the structure, adding the imperfection D/10000 corresponding to 0.03 metres and no imperfection to the imperfections in table 6.1, was also studied, using load-deflection curves.

6.2.6 Sensitivity to creep

The effect of creep on global elastic stability was studied by reducing the Young's modulus for permanent loads. Five Young's moduli were tested: 7,8,9,10 and 10.8 GPa, where the latter is the characteristic value for Gl30c glulam, and therefore provided an upper bound control value in each load case.

6.2.7 Combined effect of creep and imperfections

The combined effect of creep and imperfection was investigated by repeating the steps taken in section 6.2.5 reducing the Young's modulus to 7 GPa for permanent loads.

6.2.8 Sensitivity to settlements

The stability of the dome was studied for two cases of settlements: a radial settlement where the base was allowed to move outwards, and a differential settlement where half of the dome was displaced vertically.

Radial settlements

The dome was given a fictitious base tension ring that allowed for radial elongation of the base. While the Young's modulus of the ring was kept constant at 30 GPa, the cross section was changed from 0.25 to 25 according to A_{ring} in table 6.2

Table 6.2: Relative axial stiffness in relation to the largest cross section 5x5

Cross section, A_{ring}	0.5x0.5	0.8x0.8	1x1	1.5x1.5	2x2	3x3	5x5
Rel. axial stiffness	0.01	0.03	0.04	0.09	0.16	0.36	1.00

The radial settlement was analysed using only load case 1 as imposed load, see fig. 6.15 for load cases. The load was applied until elastic stability failure. Meanwhile, the load path was traced.

Differential settlement

A differential settlement was applied along half of the dome. Half of the base nodes were displaced vertically, linearly decreasing displacement from point A($u = \delta_{max}$) to B($u = 0$) and C($u = 0$) , seen in fig. 6.4. The value of δ_{max} was changed in the parameter study according to table 6.3.

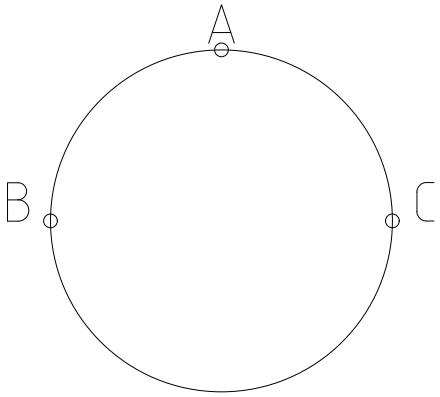

Figure 6.4: Differential settlement, δ_{max} at point A, zero displacement in B and C.

Table 6.3: Values of max vertical displacement δ_{max} at point A.

δ_{max} [m]
0.01
0.02
0.05
0.10
0.20
0.50
1.00
2.00

In every parameter study, both in radial and differential settlements, the structure was loaded with constant self weight and then imposed load until elastic stability failure. The load path was traced to study how the settlement could affect the elastic stability.

6.2.9 Stresses in ultimate limit state

The stresses of the structure had to be studied in order to know if the critical imposed loads, either caused by imperfections or creep or the combined effect of the two, occurred at stress levels above or below the maximum stress level of the material. The stresses were calculated using eq. (6.2).

$$\sigma = \frac{N_c}{A} + \frac{M''}{W} \tag{6.2}$$

6.3 Generating geometry

The node locations for the three dome patterns presented in section 6.1 will be defined below in detail. The description regards a general geometry for each pattern and not the exact pattern used in analysis. The geometries used for the comparison and analysis are found in MATLAB-scripts presented in appendix C.

6.3.1 Kiewitt

The Kiewitt nodes were created from equally spaced rings. The Kiewitt dome derived in this example has six sectors, which means that the first ring lies on a regular hexagon. The number of sectors is equal to number of nodes on the first ring, or the order of the polygon. The order of the polygon on the following ring increases with the number for the first. In other words, the number of nodes on the first three rings becomes: 6, 12 and 18, if based on a hexagon. In more general terms:

$$n_r = r \cdot s \tag{6.3}$$

n_r Number of nodes on ring number r
r ring number

s Number of sectors

The relationship in eq. (6.3) was used to calculate the initial angle for the first node on each ring, see eq. (6.4).

$$\alpha_r = \frac{2\pi}{n_r} \tag{6.4}$$

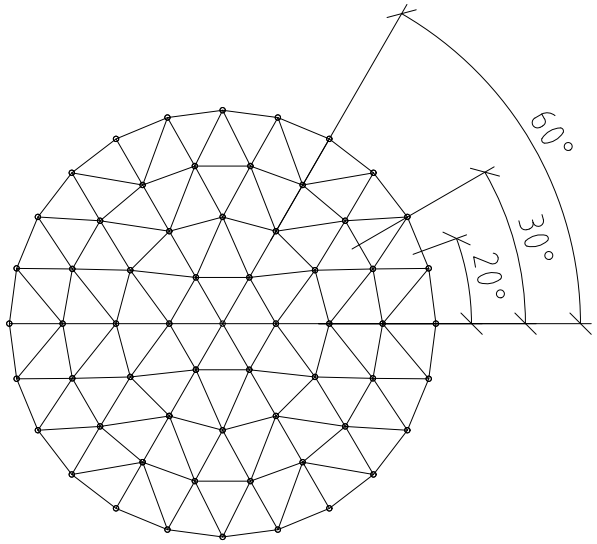

Figure 6.5: Kiewitt$_{6s,4r}$ 6 with 4 rings. The angles 60, 30, 20 correspond to $\alpha_1, \alpha_2, \alpha_3$.

The coordinates were calculated according to:

$$x_{i,r} = \frac{D \cdot r}{2 \cdot r_t} \cdot cos(\alpha_i \cdot n_{i,r}) \tag{6.5}$$

$$y_{i,r} = \frac{D \cdot r}{2 \cdot r_t} \cdot sin(\alpha_i \cdot n_{i,r}) \tag{6.6}$$

D Span
r_t total number of rings
$n_{i,r}$ node i on ring r
$\frac{D \cdot r}{2 \cdot r_t}$ the radius for ring r

The z-coordinates were calculated according to eq. (6.7).

$$z_{i,r} = \sqrt{R^2 - x_{i,r}^2 - y_{i,r}^2} \tag{6.7}$$

6.3.2 Geodesic

The geodesic geometry was defined by using an icosahedron, which consists of 12 vertices and 20 faces/triangles. The number of subdivisions of each triangle, other times referred to as the frequency, had to be decided in order to define a sphere, or a dome, from the icosahedron. An example of a 3-frequency subdivision is shown in fig. 6.8. The number of subdivisions indicate how many times each triangular face of the icosahedron has been divided, shown in fig. 6.6. This only serves as an introduction, the frequency in the studied dome was increased to obtain suitable element lengths. An attempt was made to describe subdivisions of higher order in more general terms.

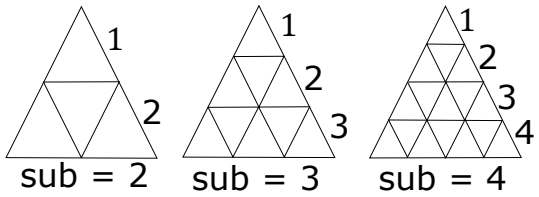

Figure 6.6: Subdivision 2 to 4.

The nodes in the icosahedron were placed such that the crown(point a) was in the position $\{0, 0, 1\}$. The variables used to define the icosahedron include the angles $\alpha_1 - \alpha_4$, the lengths $H_1 - H_3, R, S$, and the x and y coordinates of point c.

$S = 2$	Side length of the icosahedron inscribed the unit sphere
$R = \frac{S}{2\sin(\alpha_4)}$	Radius of the sphere, fig. 6.7c
$H_1 = R\cos(\alpha_4)$	fig. 6.7c
$H_2 = \sqrt{S^2 - R^2}$	fig. 6.7d
$H_3 = \sqrt{(H_1 + R)^2 - H_1^2}$	fig. 6.7c
$Z_1 = (H_3 - H_2)/2$	fig. 6.7e
$Z_2 = Z_1 + H_2$	fig. 6.7
$\alpha_1 = 2\pi/5$	The angle between nodes b and c
$\alpha_2 = \pi/10$	The angle between the x-axis and node c
$\alpha_3 = -3\pi/10$	The angle between the x-axis and node d
$\alpha_4 = \pi/5$	The angle between node d and the y-axis
$c_x = R\cos(\alpha_2)$	x coordinate of point c
$c_y = R\sin(\alpha_2)$	y coordinate of point c

The twelve vertices can be defined, see fig. 6.7 and fig. 6.7a especially.

$a = \{0, 0, Z_1\}$	$e = \{-S/2, -H_1, Z_2\}$
$b = \{0, R, Z_2\}$	$f = \{-c_x, c_y, Z_2\}$
$c = \{c_x, c_y, Z_2\}$	$g = \{0, -R, -Z_2\}$
$d = \{S/2, -H_1, Z_2\}$	$h = \{-c_x, -c_y, -Z_2\}$

$i = \{-S/2, H_1, -Z_2\}$ $k = \{c_x, -c_y, -Z_2\}$
$j = \{S/2, H_1, -Z_2\}$ $l = \{0, 0, -Z_1\}$

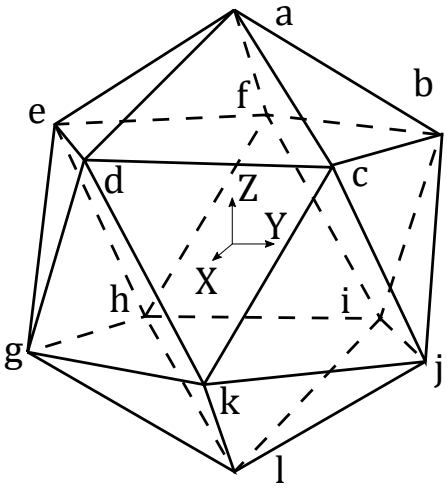

(a) An icosahedron with nodes labeled[62].

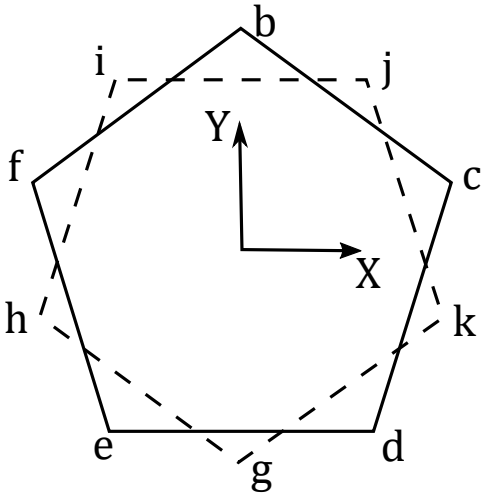

(b) An icosahedron viewed from the top[62].

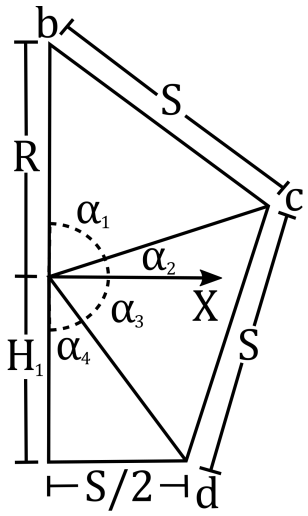

(c) Calculating the X and Y coordinates for points b, c, and d[62].

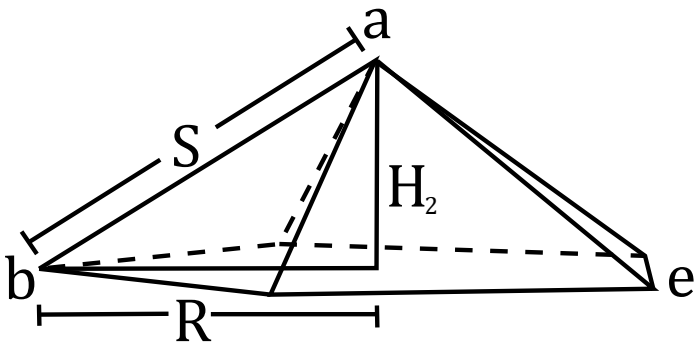

(d) The top of an icosahedron[62].

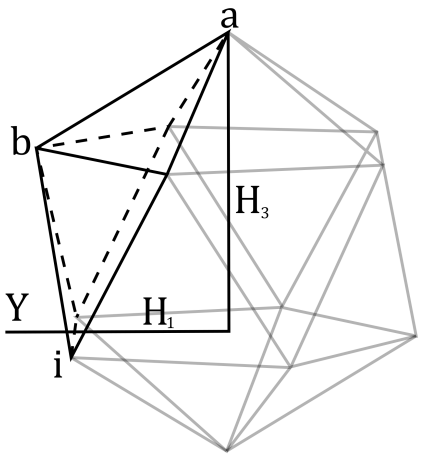

(e) The side of an icosahedron[62].

Figure 6.7: Icosahedron.

In order to obtain the coordinate locations, for a 3-frequency subdivision, the intermediate nodes along the triangle boundary had to be calculated first[63]. Vectors were defined starting from the origin $\vec{O} = \{0, 0, 0\}$. The equations 6.8-6.10 uses the vectors $\vec{A}_i$ and $\vec{J}_i$.

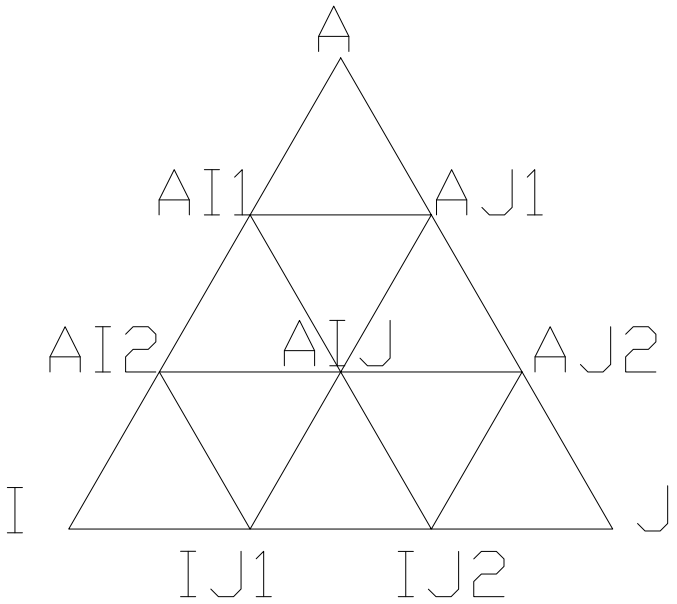

Figure 6.8: A 3 subdivision (3-frequency) icosahedron triangle, inspired by D. Bertels[63].

$$\frac{1}{3}\vec{AB}_i = \frac{2\vec{I}_i + \vec{J}_i}{3} \tag{6.8}$$

$$\frac{2}{3}\vec{AB}_i = \frac{\vec{I}_i + 2\vec{J}_i}{3} \tag{6.9}$$

The location of a central node was calculated according to

$$\frac{1}{2}\vec{AB}_i = \frac{\vec{I}_i + \vec{J}_i}{2} \tag{6.10}$$

The calculations for the node locations shown in fig. 6.8 are presented below in table 6.4. The coordinates for $\vec{A}$, $\vec{I}$ and $\vec{J}$ belong to the icosahedron and therefore also the sphere.

Table 6.4: Node locations in fig. 6.8

Node Name	$A\vec{I}1$	$A\vec{I}2$	$A\vec{J}1$	$A\vec{J}2$	$I\vec{J}1$	$I\vec{J}2$	$A\vec{I}J$
Equation	$\frac{2\vec{A}+\vec{I}}{3}$	$\frac{\vec{A}+2\vec{I}}{3}$	$\frac{2\vec{A}+\vec{J}}{3}$	$\frac{\vec{A}+2\vec{J}}{3}$	$\frac{2\vec{I}+\vec{J}}{3}$	$\frac{\vec{I}+2\vec{J}}{3}$	$\frac{A\vec{I}2+A\vec{J}2}{2}$

The same principle was applied to subdivisions of higher frequency, by using the general formulation in eq. (6.11)[63].

$$\frac{v}{w}\vec{AB} = \frac{(w-v)\vec{A} + v\vec{B}}{w} \tag{6.11}$$

v The number of steps from the first node
w Number of subdivisions
$\vec{A}$ The vector from the origin to a node on the icosahedron
$\vec{B}$ The vector from the origin to a node on the icosahedron

The projection of the nodes onto the sphere was done by dividing each coordinate with its corresponding radius[63], and thus normalising the coordinate. The radius was calculated according to eq. (6.12).

$$R_{\frac{v}{w}\vec{AB}} = \sqrt{x^2_{\frac{v}{w}\vec{AB}} + y^2_{\frac{v}{w}\vec{AB}} + z^2_{\frac{v}{w}\vec{AB}}} \tag{6.12}$$

Normalising the coordinates and projecting them onto the sphere:

$$\frac{v}{w}\vec{AB}_{norm} = \frac{(w-v)\vec{A} + v\vec{B}}{w \cdot R_{\frac{v}{w}\vec{AB}}} \tag{6.13}$$

The triangle consists of the three corner nodes, the boundary nodes, and the interior nodes. The number of nodes can be expressed according to eq. (6.14)-(6.15) and are valid for a frequency 3 and above.

$$n_c = 3 \qquad n_b = 3(f-1) \qquad n_i = \sum_{f=3}^{f_{tot}} (f-2) \tag{6.14}$$

$$n_{total} = 3f + \sum_{f=3}^{f_{tot}} (f-2) \tag{6.15}$$

The process of defining the node locations based on an icosahedron can be summed up as follows:

1. Determine the frequency
2. Calculate the nodes based on eq. (6.11)

3. Project the nodes onto the sphere by dividing the vector, coordinate, by its radius defined in eq. (6.12)
4. Copy and rotate the nodes of the one original triangle
5. Removing the redundant nodes below the level of the supports
6. Complete the dome by adding nodes to get a circular base

6.3.3 Three-way grid

The three-way grid was constructed using a hexagon as the base polygon, but it can be done with several other regular polygons as well. Thus, in this example, the nodes were obtained by generating equally spaced hexagons, which then were subdivided seven times. The subdivision process was identical to the one mentioned in section 6.3.2.

This process generated a hexagonal shape in the xy-plane. Nodes were placed radially from the origin, equal to the number of subdivisions, to get a circular base and the coordinate locations of the intermediate supports. The z-coordinates were then obtained using eq. (6.7).

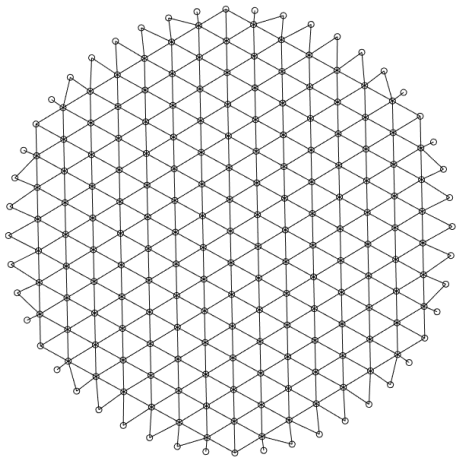

Figure 6.9: Three-way grid with hexagonal polygonal pattern and 7 elements from the apex to the base.

6.4 Finite element modelling

6.4.1 Continuous shell

The continuous shell dome was modelled in Abaqus/CAE, using rectangular shell elements. The continuous dome was intended to represent the analogy of the reticulated dome. Therefore, the shell thickness was set to 1.6, equal to the beam height.

The material was defined using the *property*-module in Abaqus. The material was modelled as isotropic with a modulus of elasticity(E) of 0.55 GPa, and Poisson's ratio equal to 0.3, which was the same used in the reticulated domes. The section was defined as *shell, homogeneous*.

The mesh was generated using rectangular elements of type S4R with an approximate global size equal to 1. Second-order accuracy was turned on. A pressure load of magnitude 1 was applied, i.e. uniformly distributed load perpendicular to the surface. The boundary conditions were set to pinned along the base ring.

In the *step*-module, *linear perturbation, buckle* were chosen with Lanczos algorithm. The result output gave an eigenvalue for the corresponding mode shape which corresponded to the computed linear buckling load of the dome.

After running the linear buckling analysis, a *Static, Riks*-procedure was set up to analyse any non-linear response according to third order theory. A pressure load equal to the eigenvalue obtained in the linear buckling analysis step was set. An upper bound non-linear critical pressure was established using a geometry without any imperfections. Next, a parameter study was performed using imperfections based on the first mode shape. The scaling factors are listed in table 6.1.

6.4.2 Modelling of local snap-through

Snap through was modeled in Abaqus by looking at a five member cell in isolation, see fig. 6.3. The beam element B31 was used and the cross-section was set to 0.8x1.6 m^2. The beams were 14.31 meters long, the same length as the members connected to the apex, and were assembled according to fig. 6.3. The midpoint rise was set to 0.6 metres.

Snap through was studied by looking at three scenarios in fig. 6.3. The connection was modelled using multi point constraint, *MPC*. The settings used were: *pin* for a pinned connection and *tie* for a fixed/rigid node. The boundary conditions for the five supports were: *pinned, fixed encastre, pinned*, in Case 1, 2, and 3, respectively. Encastre is the boundary condition equivalent to fixed in Abaqus. The beams were braced, see section 6.4.7.

A concentrated force was applied at the midpoint node, and increased incrementally to take non-linearity into account.

6.4.3 Elements

The entire model was modeled by discrete beam elements of type B31[64] according to Abaqus standard, meaning linear beam elements in 3-dimensional space. Each beam in the dome was modelled as 20 B31 beam elements in order to properly simulate the bending behaviour.

6.4.4 Material

Despite timber being an orthotropic material, it was not motivated to model a detailed material property on such a large scale structure, using line elements. The material setting only included the stiffness, Young's modulus equal to 10.8 GPa, and the Poisson's ratio set to 0.3.

6.4.5 Beam section and orientation

In Abaqus, a generalised beam section was chosen with the following input parameters:

A	Cross sectional area
I_{11} & I_{22}	Moment of inertia in each primary axis
I_{12}	Product of inertia
J	Torsion constant

The parameters are all independent from each other, meaning that adjusting the cross sectional area does not automatically change any other parameter. The parameters were instead calculated by a Matlab sub-routine prior to model implementation. The torsion constant, J, was determined according to eq. (6.16).

$$J = hw^3 \left(\frac{1}{3} - 0.21 \frac{w}{h} \left(1 - \frac{w^4}{12h^4} \right) \right) \tag{6.16}$$

h	Height of the cross section
w	Width of the cross section

The members were also oriented such that they followed the normal of the enclosing sphere. This is shown schematically in fig. 6.10, where n_1 is a beam close to the apex and n_2 show a beam closer to the base.

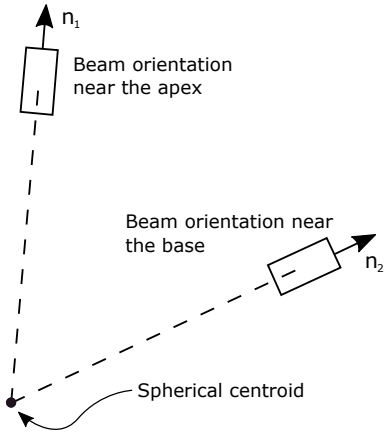

Figure 6.10: Beam orientation rotated around the spherical centroid.

6.4.6 Boundary conditions and node rigidity

Beams connected to the base were modelled with fixed supports. The tension ring was assumed to be infinitely stiff and it was therefore not included in the initial model. It was, however, introduced when radial settlement was studied, see section 6.4.10. The use of encastre supports over pinned was chosen as a result of the assumed cantilever erection procedure. The nodes were assumed to be fixed for the same reason. The model was created as one entire part, resulting in rigidly connected members.

6.4.7 Simulating roof bracing

To avoid global torsional failure, see fig. 4.8d, and control lateral torsional buckling, the lattice structure was assumed to be restrained by the secondary roof structure carried by the dome. The presumed roof bracing was modelled by prohibiting rotation of five intermediate nodes and the ends of every beam, see fig. 6.11.

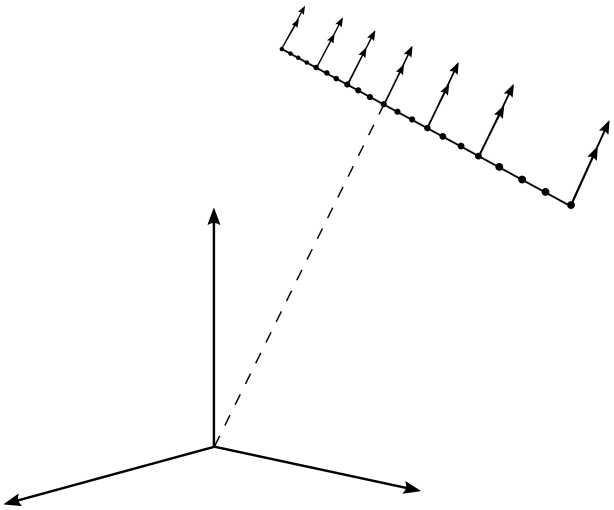

Figure 6.11: Rotational boundary conditions applied at discrete points along the beams to prevent lateral bending. The dots represent start/ending points of the B31 elements used in Abaqus, and the arrows represent boundary locations.

6.4.8 Modelling imperfections

The imperfections were modelled by introducing base modal shape imperfections from the seven first eigenshapes, for each corresponding load case, resulting in 21 different initial imperfection shapes. The initial imperfections were scaled according to table 6.1. The self weight of the structure was included in all linear buckling calculations. The mode shapes were obtained by performing an eigenvalue analysis employing the Lanczos method.

6.4.9 Modelling creep

Creep was modelled by modifying the Young's modulus. The stiffness was reduced only during the first step, where the self weight was applied. During the imposed load, the modulus was reverted to its default value. Table 6.5 shows the implemented procedure.

Table 6.5: Operational steps of simulating creep. See fig. 6.12.

Step	Case	Young's modulus
1	Self weight	Reduced
2	Imposed load	Constant (10.8 GPa)

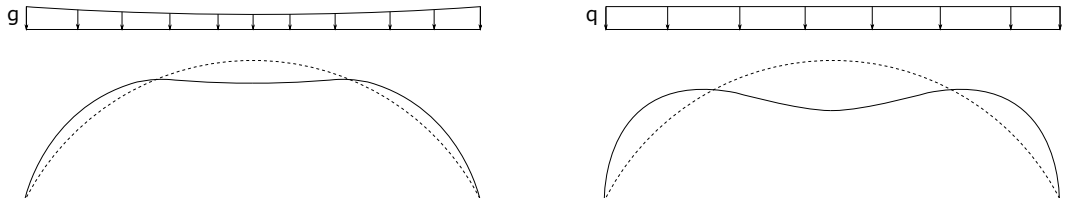

(a) Deformed shape caused by creep, self weight (g) (Step 1)

(b) Deformation caused by imposed load (q) and self weight (Step 2)

Figure 6.12: Schematic method used to study creep.

6.4.10 Modelling settlement

Radial settlements

The boundary conditions were altered to simulate a radial displacement of the base. The changed boundary conditions are listed below, and a graphical representation can be seen in fig. 6.13.

- Restriction of vertical movement of every base node,
- Node A was fully restricted to move in the horizontal plane,
- Node B was only restricted in one direction in the horizontal plane

This configuration allowed for radial settlement, while preventing rigid body motion.

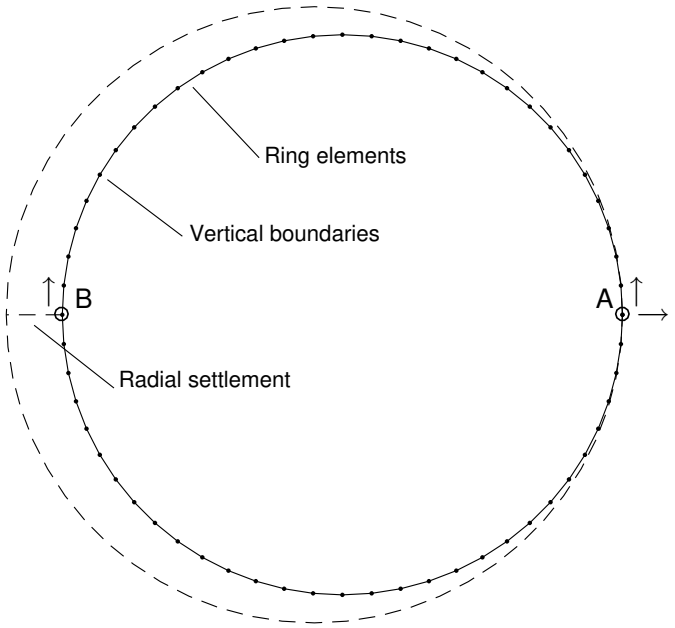

Figure 6.13: Boundary conditions applied to capture the radial settlement.

The outwards movement was governed by the introduced tension ring, seen in fig. 6.13. Note that the ring is fictitious and does not necessarily represent a realistic one. The tension stiffness was varied by changing the cross sectional area, whilst keeping the modulus of elasticity constant, equal to 30 GPa.

Remark that this type of boundary setup, combined with ring elements, was only applied in the case of radial settlements.

Differential settlements

The differential settlements were modelled by displacement controlled operation along one half of the base nodes. Maximum displacement, δ_{max}, was applied to node A, in fig. 6.14. The displacement was set to zero in nodes B and C, decreasing linearly from A.

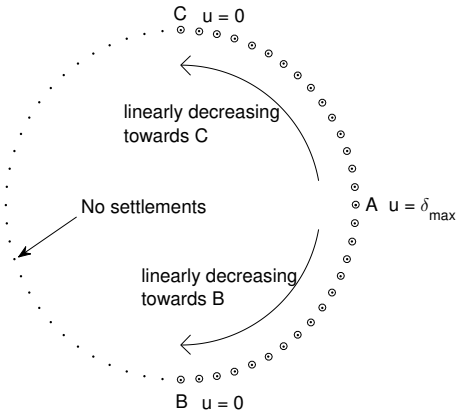

Figure 6.14: Differential settlement applied to the base nodes.

Table 6.6: Operational steps of simulation

Step	Case	Control type
1	Self weight	Force
2	Settlement	Displacement
3	Imposed load	Force

The Abaqus model had a two step procedure, including self weight and imposed load, before adding the displacement controlled settlement. This step was added in between the two initial steps, as outlined in table 6.6. The added step included non-linear behaviour, just like the first step, analysed using the Newton-Rhapson method.

6.4.11 Applying loads

The load on the structure consisted of dead load and imposed snow load. The self weight of the structure included the load carrying elements as well as the secondary structure. Since the roof was not included in the model, the weight of the secondary structure was added by increasing the density of the elements using eq. (6.17) and eq. (6.18)

$$q_{lb,eqv,d} = \frac{\rho V g}{A} \tag{6.17}$$

$$\rho_{eqv} = \rho\Big[\frac{q_{lb} + q_{secondary}}{q_{lb}}\Big] \tag{6.18}$$

$q_{lb,eqv,d}$ The equivalent design area load of the load bearing elements [kN/m^2]
ρ The density of glulam GL30c, 430 [kg/m^3]
V Volume of the load bearing members [m^3]
g Acceleration, 9.81 [m/s^2]
A Area of the dome
$q_{secondary,d}$ Design load of the secondary roof structure, assumed to 0.8 [kN/m^2]
ρ_{eqv} The equivalent density of the load bearing elements including the weight of the secondary structure [kg/m^3]

Three snow load cases were studied, see fig. 6.15, including full coverage, half and one sector, respectively. These were modelled as line loads, which were converted to area loads according

to eq. (6.19). The line loads were adjusted to more accurately represent a horizontally projected snow load. This was done by reducing the applied load by the factor seen in eq. (6.19).

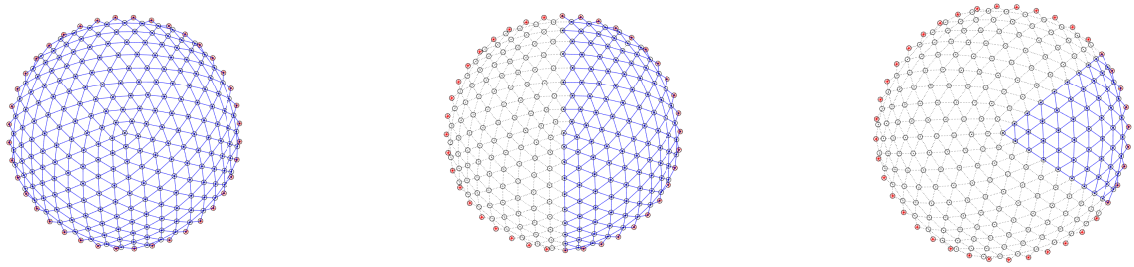

(a) Load case 1: 100% **(b)** Load case 2: 50% **(c)** Load case 3: 20%

Figure 6.15: Percentage snow coverage, where the dashed lines were unloaded and blue(full) lines were loaded with snow.

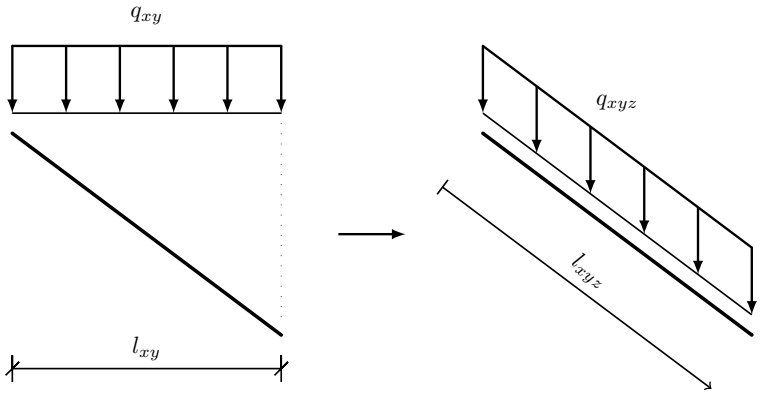

Figure 6.16: Adjusted line load.

$$q_{eq,d} = \frac{\sum\left[q_{xy} \cdot \frac{l_{xy}}{l_{xyz}}\right]}{A_{covered}} \tag{6.19}$$

q_{xy}	Line load [kN/m]
l_{xy}	fig. 6.16
l_{xyz}	fig. 6.16
$A_{covered}$	The area covered by the snow, 20, 50 and 100% of the dome area
q_{eq}	Equivalent area load [kN/m^2]

The design load, in [kN/m^2], was written according to eq. (6.20),

$$q_d = G_d + q_{eq,d} \tag{6.20}$$

where $G_d = q_{lb,eqv,d} + q_{secondary,d}$ is the self weight of the structure and $q_{eq,d}$ is the imposed design load.

6.4.12 Mesh convergence study

In order to verify that the beam element, B31, in the model was behaving according to theory, a mesh convergence study was performed, see appendix A. The study involved linear buckling analysis on a simply supported column and an arch with various amount of elements. The results are seen in the appendix, and the members were finally given 20 elements each.

Chapter 7

Dome comparison

The three dome patterns, Kiewitt, Three-way grid, and Geodesic were compared in terms of strength, stability and design considerations. The geometries were designed in order to have approximately the same total length, number of nodes and number of supports, summarised in table 7.1.

7.1 Design considerations

The design considerations included member length distribution and number of unique element lengths, fig. 7.1 and fig. 7.2 respectively. From fig. 7.1 it was concluded that the Geodesic sub 11 has a favourable distribution, where 99 % of the lengths are in the interval 14.3–20.1 metres compared to 12.8-32.8 and 13.7-23.6 for the Kiewitt and Three-way grid, respectively. An additional advantage is the maximum length of 20.1 metres, which is possible to produce, whereas lengths above 30 could pose a problem in production, and/or in transport.

Table 7.1: Linear buckling comparison of the dome patterns, sorted by critical load capacity.

Dome pattern	n_n	n_s	n_E	L_{tot} [km]	L_{rel}
Geodesic sub 11	386	60	1035	18.45	1.00
Three-way grid	391	66	1038	18.88	1.02
Kiewitt 8 sectors 9 rings	361	72	936	19.21	1.04

n_n	Number of nodes
n_s	Number of supports
n_E	Number of elements
l_n	The number of loaded nodes
L_{tot}	The sum of the element lengths
L_{rel}	The relative length with the L_{tot} Geodesic sub 11 as base value

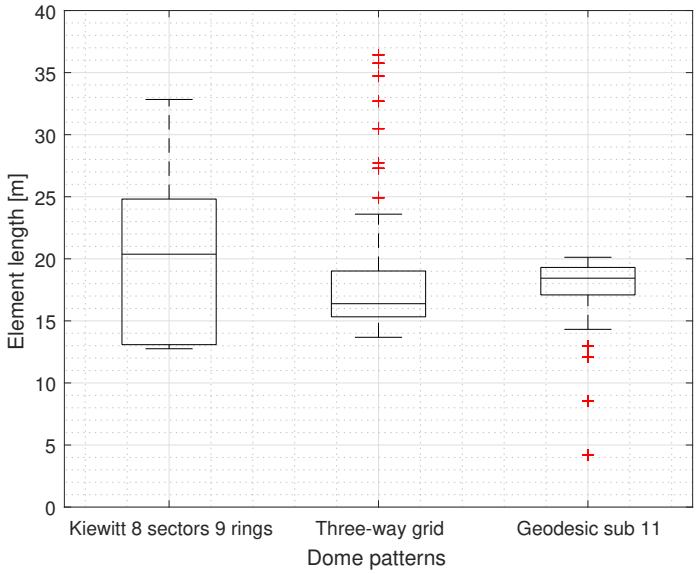

Figure 7.1: Member length distribution comparison of the dome patterns.

In order to reduce the cost, the number of unique elements has to be reduced. Elements cannot be produced to the exact node-to-node distance produced by the Matlab code, and since the actual tolerance is unknown the number of unique elements was studied by a tolerance interval from 1 to 20 millimetres. The number of different lengths was similar for the Kiewitt and the Geodesic geometries, which can be seen in fig. 7.2.

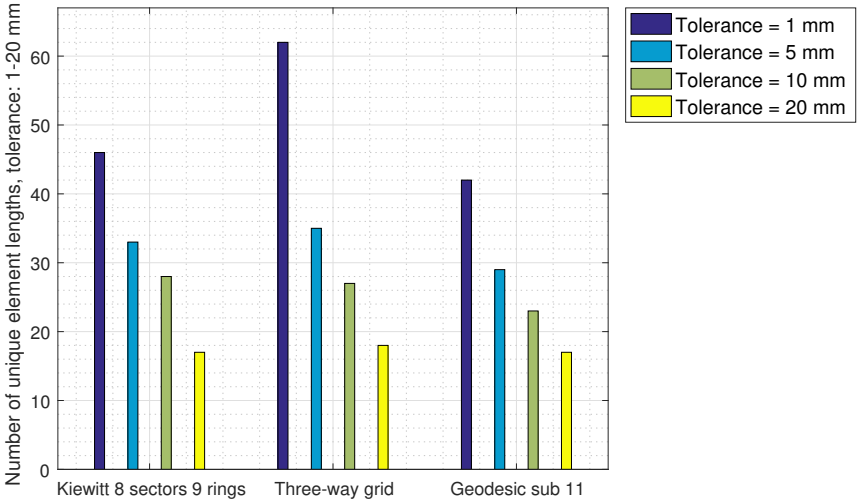

Figure 7.2: Number of unique element lengths depending on tolerance.

7.2 Strength and stiffness

The three domes were compared in terms of stiffness and strength, where stiffness was compared based on the maximum vertical displacement in each load case and strength on the linear buckling load. This was done for load cases one and two, with an imposed load of 3 kN/m^2. The deflection for the Kiewitt, the Three-way grid, and the Geodesic sub 11 was: 88, 115 and 155 mm, respectively for load-case one, and 120, 117 and 138 mm for load-case 2. Strength was measured by the linear buckling load, in load case 1 and 2. The result can be seen in table 7.2.

Table 7.2: The strength and stiffness compared by linear buckling in load case 1 and 2, for the different surface arrangements.

	Strength q_{crit} [kN/m^2]		**Stiffness** [mm]	
Arrangement	LC1	LC2	LC1	LC2
Kiewitt	62.9	53.0	88	120
Three-way grid	61.6	60.3	115	117
Geodesic	66.1	61.1	155	138

7.3 Choice of dome - Geodesic

The Geodesic pattern was chosen for further study based on

- **The higher stability load**
  Table 7.2 shows that the Geodesic geometry was favourable in both symmetrical and asymmetrical load cases. The difference was quite small between the Kiewitt and the Geodesic surface arrangements in load case 1, and the Three-way grid and the Geodesic in load case 2. Nevertheless, a higher critical failure value was seen as important since one of the main purposes of the thesis was to conclude that a dome with a span of 300 metres would not collapse due to the loss of stability.

- **The lower deviation of member lengths**
  The results seen in fig. 7.1 show a more concentrated distribution of member lengths for the Geodesic dome when compared to the Kiewitt and the Three-way pattern. Another important factor was the outlying element lengths, where the Geodesic domes had outliers that were shorter than the median length. The Three-way grid and Kiewitt had elements with lengths of over 30 metres, which are not practical in production and transportation.

- **The number of unique element lengths**
  The cost of the dome would likely decrease if the number of unique element lengths was low. The Geodesic geometry was slightly more favourable in that regard, as can be seen in fig. 7.2.

The only area of weakness of the Geodesic surface arrangement was the lower stiffness, particularly in load case 1, see table 7.2. This could potentially increase the non-linear behaviour of the structure.

7.3.1 Suitable subdivision - mesh density

Three different versions of the Geodesic geometry were compared, see fig. 7.3. These were subdivisions 9,10 and 11, where the number indicate the number of elements from the apex to the base along a meridian, seefigs. 6.6 and 7.5.

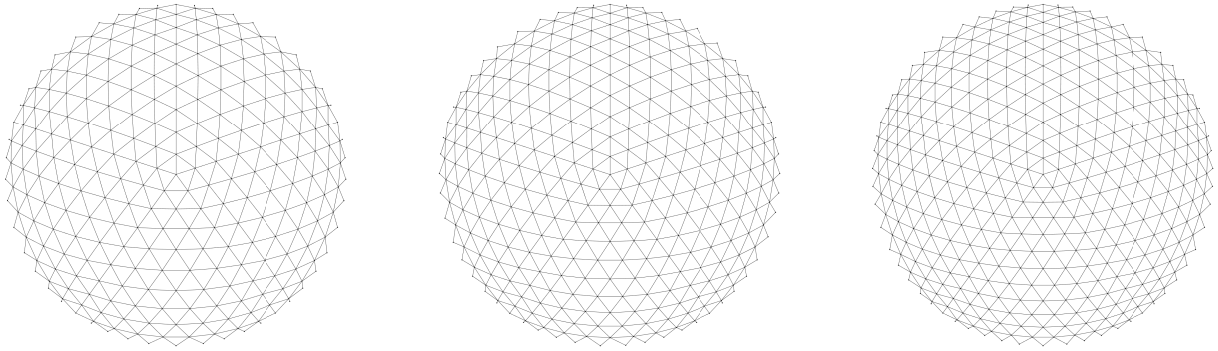

(a) Geodesic sub 9 **(b)** Geodesic sub 10 **(c)** Geodesic sub 11

Figure 7.3: Three different Geodesic subdivisions, where the subdivision is equal to the number of elements from the apex down to the base along a meridian.

The subdivision comparison included controls for combined bending and axial compression as well as tension. These were expressed in relation to the largest allowable stress in each case, and can be found in eq. (7.1) and eq. (7.2). The result is presented in tables 7.3-7.7 for a Geodesic dome with subdivisions 9-11. The material properties were calculated in chapter 5.

$$\frac{N_c}{A} \cdot \frac{1}{f_{cd}} + \frac{M''}{W} \cdot \frac{1}{f_{md}} < 1 \tag{7.1}$$

$$\frac{N_t}{A_r} \cdot \frac{1}{f_{td}} < 1 \tag{7.2}$$

N_c	Axial compression [N]
M''	Second order moment [Nm].
	Based on an initial imperfection factor of D/300, see section 6.2.4
W	Section modulus, $bh^2/6$, [m^3]
N_t	Axial tension [N]
A_r	Reduced cross sectional area to account drill holes, for example.
	Assumed to be $0.7 \cdot A$, [m^2]
f_{cd}	Design strength in compression 15.7 MPa
f_{md}	Design strength in bending 19.2 MPa
f_{td}	Design strength in tension 12.5 MPa

Table 7.3: Controls for combined bending and axial force, and tension according to eq. (7.1)-(7.2). Imposed loading $q = 2$ [kN/m^2], loadcase 1.

Sub/Control	eq. (7.1)	eq. (7.2)
Subdivision 9	0.66	0.22
Subdivision 10	0.52	0.23
Subdivision 11	0.42	0.20

Table 7.4: Controls for combined bending and axial force, and tension according to eq. (7.1)-(7.2). Imposed loading $q = 2$ [kN/m^2], loadcase 2.

Sub/Control	eq. (7.1)	eq. (7.2)
Subdivision 9	0.67	0.13
Subdivision 10	0.59	0.12
Subdivision 11	0.55	0.12

Table 7.5: Controls for combined bending and axial force, and tension according to eq. (7.1)-(7.2). Imposed loading $q = 3$ [kN/m^2], loadcase 1.

Sub/Control	eq. (7.1)	eq. (7.2)
Subdivision 9	0.83	0.28
Subdivision 10	0.65	0.29
Subdivision 11	0.59	0.25

Table 7.6: Controls for combined bending and axial force, and tension according to eq. (7.1)-(7.2). Imposed loading $q = 3$ [kN/m^2], loadcase 2.

Sub/Control	eq. (7.1)	eq. (7.2)
Subdivision 9	0.87	0.17
Subdivision 10	0.77	0.15
Subdivision 11	0.72	0.14

Table 7.7: Linear buckling values, $q_{cr,linear}$ for subdivisions 9-11, load case 1.

Subdivision/frequency	q_{cr} [kN/m^2]
Subdivision 9	50.4
Subdivision 10	59.0
Subdivision 11	66.1

Two sources were presented in section 4.4.3 regarding the effect of mesh density, Gioncu[38] concluding that longer elements would increase the critical load, and Pan[23] arguing that increasing the mesh density would do the opposite, and also improve the general behaviour of the dome. From the results in table 7.4-7.7, it can be concluded that increasing the subdivision from 9 to 11 in a Geodesic dome improved the linear buckling load and also reduced the stresses. For this reason, a Geodesic of frequency 11 was chosen.

7.3.2 Geometrical description

This section serves to summarise the geometry of the chosen dome. The span and height can be seen in fig. 7.4. The study was performed on a Geodesic subdivided 11 times. How to count the subdivision has been emphasised in fig. 7.5. The dimensions of the beam were set to 0.8×1.6 m^2, see section 5.4, made out of Glulam GL30c.

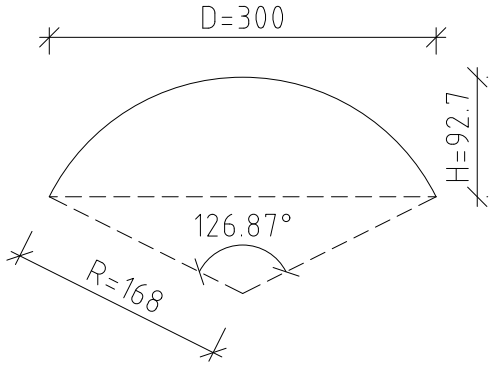

Figure 7.4: Geometry of the Geodesic sub 11. All distances are in metres.

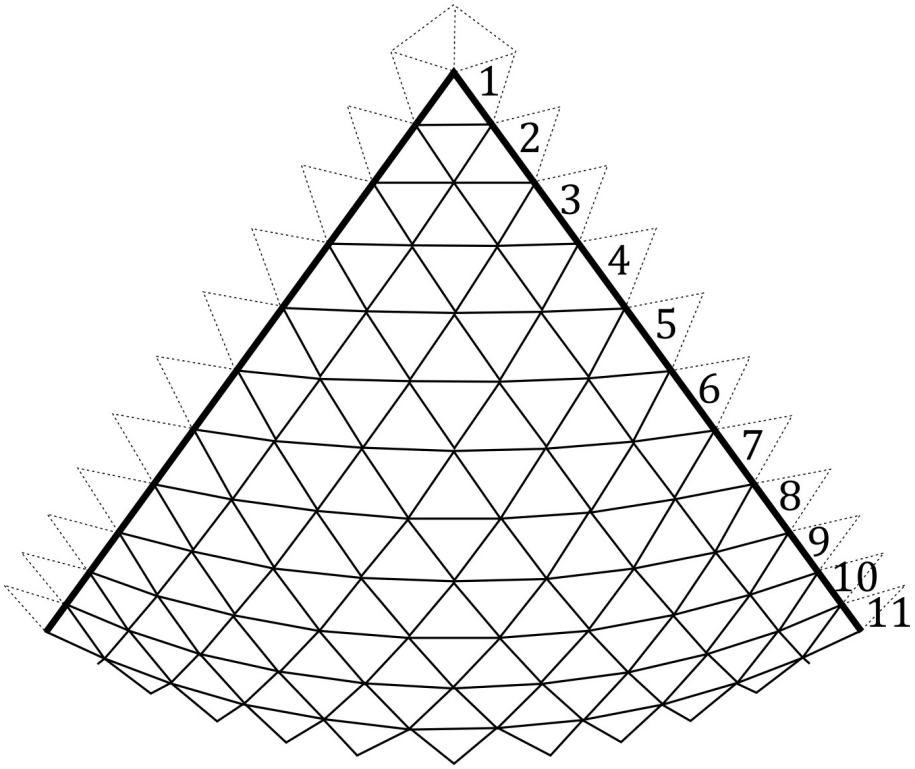

Figure 7.5: Sector of a Geodesic sub 11, where the numbers show how to count the subdivision/frequency. The meridians have been highlighted with thicker lines.

Chapter 8

Results and discussion of stability analysis

8.1 Continuous shell analogy analysis

A numerical simulation of a continuous shell was performed and compared with the formulas provided in chapter 4. The stiffness of the shell was adjusted according to eq. (5.17) in chapter 4 to account for a reticulated shell.

8.1.1 Hand calculations

The formulae are only valid within certain intervals, as described by Samuelson et al[28], and were checked in eq. (8.1).

$$\begin{aligned} R/t &< 3000 && 167.7/1.6 = 104.8 \\ 7 < \beta &< 50 && \beta = \sqrt{2\varphi\frac{R}{t}} = \sqrt{1.1 \cdot 104.8} = 10.7 \end{aligned} \tag{8.1}$$

The buckling pressure loads used were eq. (8.2) by Zoelly, and the modified version by Timoshenko in eq. (8.3). The k-values used in eq. (8.2) were 1.21 according to linear theory[29][28][2], the lower bound of 0.366[2] and the recommended value of 0.4[2]. The results are presented in table 8.1.

$$p_{cr} = k \cdot E' \left(\frac{t}{R}\right)^2 \tag{8.2}$$

$$p_{cr} = \left(1 - 0.175\frac{\varphi^\circ - 20^\circ}{20^\circ}\right)\left(1 - \frac{0.07R/t}{400}\right) 0.3E' \left(\frac{t}{R}\right)^2 \tag{8.3}$$

E'	0.554 GPa
t	1.6 m
R	167.7 m
φ	63°

Table 8.1: Non-linear buckling load results from a continuous shell dome.

Equation	k-value	Failure load [kN/m^2]	Ratio p/p_{linear}
eq. (8.2)	1.21 (linear)	61.0	1.00
eq. (8.2)	0.366 (lower bound)	18.5	0.30
eq. (8.2)	0.4 (recommended)	20.2	0.33
eq. (8.3)	—	9.3	0.15

8.1.2 Numerical results

The linear buckling analysis in Abaqus determined the eigenvalue to 60.9 kN/m^2, which is in good concordance with the hand calculated buckling loads presented in table 8.1. This ensures the numerical analysis to go along well with the theory of linear buckling of shells.

The axisymmetrical mode shape found in the numerical analysis is presented in fig. 8.1. No source was found to confirm the accuracy of this mode shape. The 2-dimensional cut in fig. 8.1 does, however, show a behaviour similar to the buckling of a continuous beam or a beam resting on spring supports.

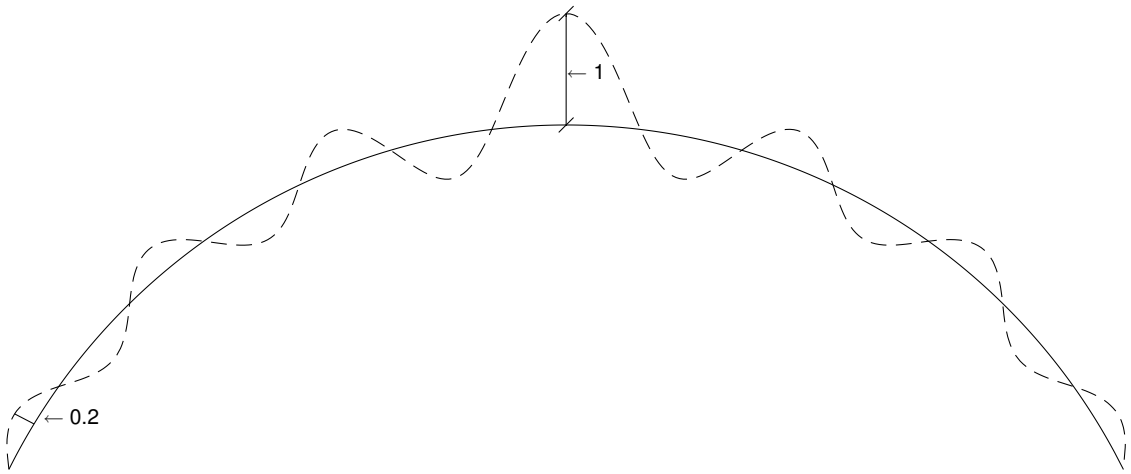

Figure 8.1: Axisymmetrical mode shape received from simulation.

The results of the non-linear buckling analysis is presented in fig. 8.2. Note that the load path showing perfect geometry makes a sudden collapse without any clear sign of lost stiffness. When the mode shape was applied in different magnitudes, the elastic buckling load reduced drastically, where the smallest imperfection of D/1000 had a remaining linear buckling capacity of 47 %. The results of failure load for each imperfection are summarised in table 8.2. Note that for the largest imperfections, D/300 and D/150, the buckling load was rising again, albeit their initial stiffness is considerably lower than the others seen in fig. 8.2.

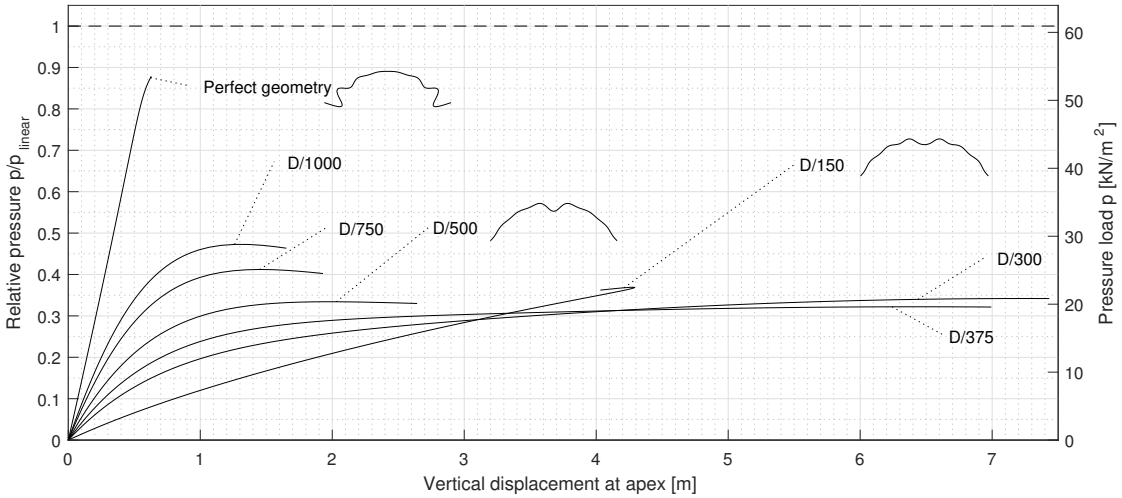

Figure 8.2: Results of non-linear buckle analysis in comparison to the linear. The imperfections D/3000, D/600 and D/300 are based on the mode shape gained from the linear buckle.

Table 8.2: Non-linear buckling load results from a continuous shell dome.

Imperfections	Failure load [kN/m^2]	Ratio p/p_{linear}	k-value for eq. (8.2)
None	53.4	0.88	1.06
D/1000	28.8	0.47	0.57
D/750	25.1	0.41	0.50
D/500	20.3	0.33	0.40
D/375	19.6	0.32	0.39
D/300	20.8	0.34	0.41
D/150	22.5	0.37	0.45

The miniature domes in fig. 8.2 show the buckle behaviour of the perfect geometry, and for the imperfections D/500 and D/150. Since the vertical displacement of the apex is seemingly linear for the perfect dome, it can also be observed in its failure shape that the buckled area is near the base. The stronger the imperfection, the more keen the dome becomes to buckle near its apex.

8.1.3 Discussion

In comparison to the hand calculated estimations of total buckling load, the numerical results showed a lowest buckling load of 19.6, which is close to the recommended hand calculated buckling load to consider when using continuous shell analogy for reticulated domes. The estimated load in eq. (8.3) deviated even further from the numerical results. It can be concluded that, while the hand calculations and the numerical analysis agree well regarding linear buckling, the non-linear results should be treated with care, as the results seem to be scattered along a wider spectra, depending on magnitude of the imperfection.

The reasons as for why the results of the non-linear numerical buckle analysis differ from the results presented in table 8.1 may be many. The analysis was limited to a single mode shape as the initial imperfection, and the size of the initial imperfection was chosen arbitrarily in order to study the impact of an increasing imperfection. Further, it should be noted that the physical experiments of continuous shells have most likely been performed on test considerably smaller in size and with use of different material, as stated back in section 4.2.

8.2 Snap-through analysis

The cases described in fig. 6.3 correspond to the upper bound in eq. (4.22). As the number of members involved in this case were five as opposed to the six members described by Wright[2], an assumed reduction of the formula by 5/6 was made.

$$W_{cr} = \frac{2AEr^3}{\sqrt{3} \cdot l^3} \cdot \frac{5}{6} = \frac{2 \cdot 1.28 \cdot 10.8 \cdot 10^6 \cdot 0.6^3}{\sqrt{3} \cdot 18^3} = 591.2 \cdot \frac{5}{6} = 492.7 \text{ kN} \tag{8.4}$$

Numerical results & discussion

The numerical results of the three cases studied, as well as the results from hand calculation are presented in fig. 8.3. As can be seen, the hand calculation coincides accurately with the first case studied (pinned connections), which corresponds to the upper bound formula by Wright[2]. The nodal load of 493 kN was converted to a uniformly distributed load equal to 7.0 kN/m^2, using eq. (4.23) from section 4.4.5. The lower bound would then be 3.5 kN/m^2, if worst case considered.

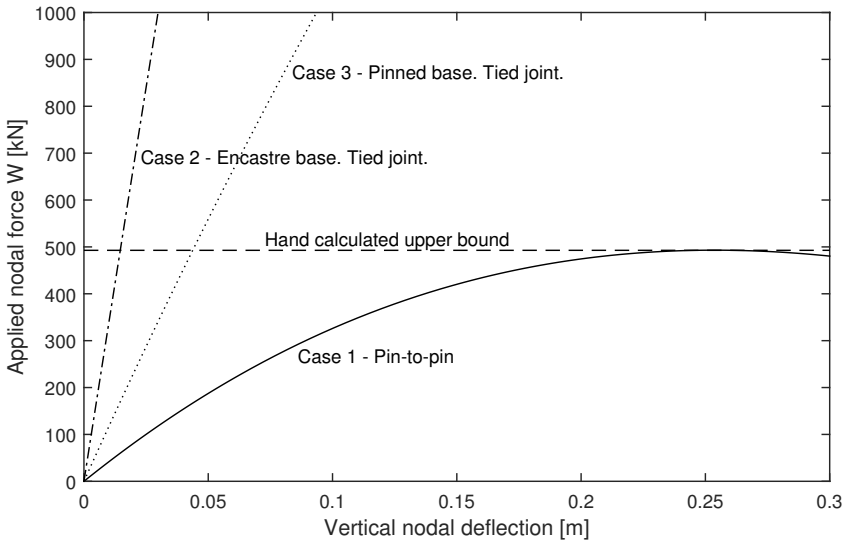

Figure 8.3: Resulting load path of the three cases studied.

Snap through failure was only observed in the completely pinned system, whereas in the two other cases, the load just kept increasing without stability failure, as seen in fig. 8.3. According to the theory explained in section 4.4.2, this should be the case.

The connections in the dome would not be completely pinned even after erection, nor would they be completely fixed either, even if they were modelled as such. In reality, the rotational stiffness of the connections would be somewhere in between the lower and upper bound values, likely closer to the latter. It can be expected that the dome will most likely have snap-buckling load higher than the upper bound found in formula used in eq. (8.4), if there is any local instability problem caused by snap through buckling at all.

8.3 Imperfections

8.3.1 Imperfection modes

The 7 first buckling modes, fig. 8.5 and fig. 8.6, in each load case were used as initial imperfections when calculating the non-linear limit point. The load cases are shown in fig. 8.4.

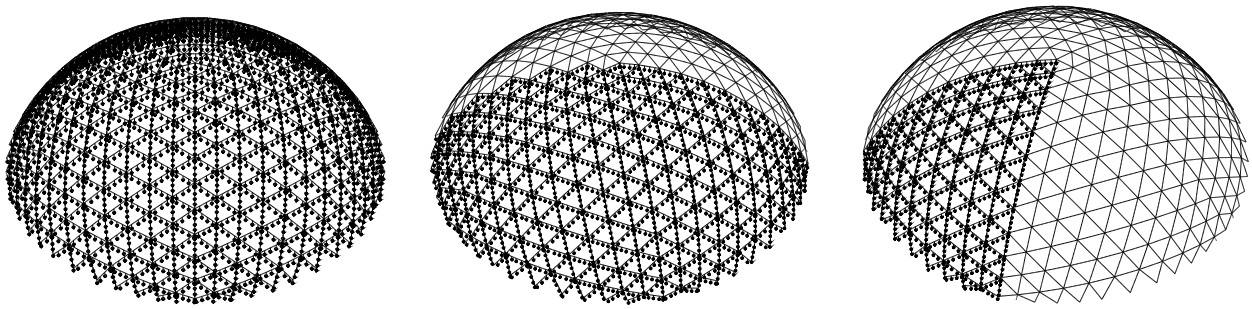

(a) Load case 1 **(b)** Load case 2 **(c)** Load case 3

Figure 8.4: The load cases in Abaqus.

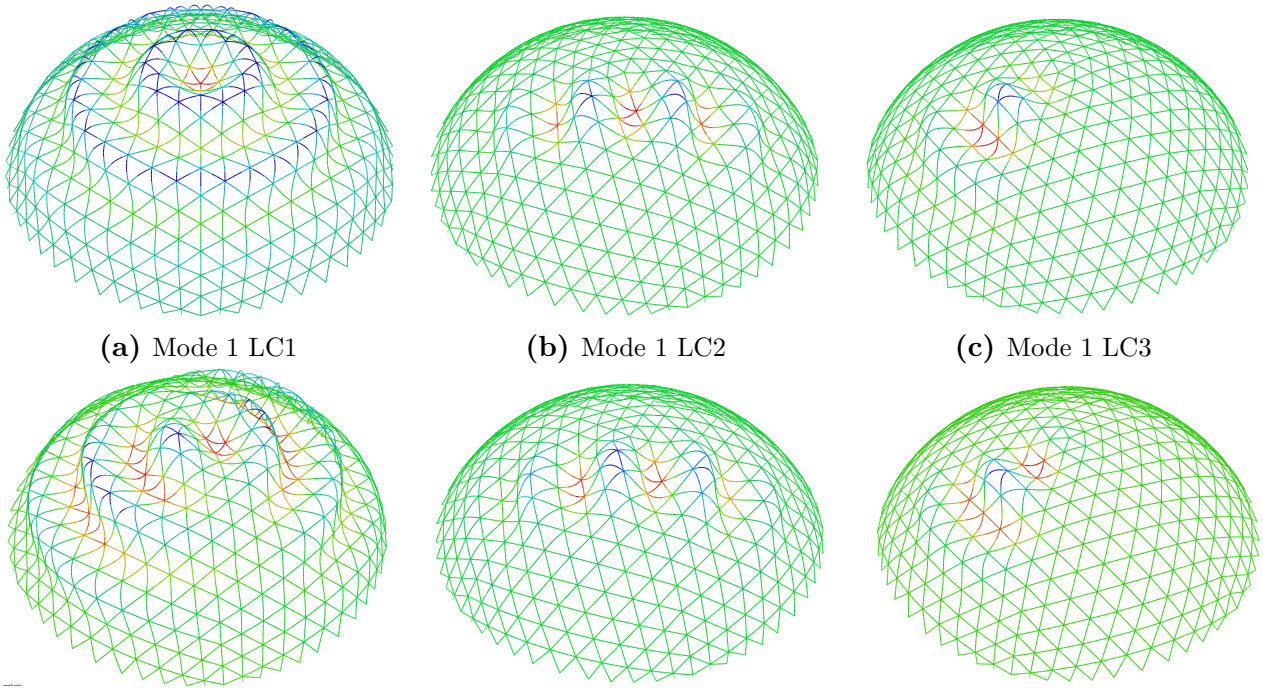

(a) Mode 1 LC1 **(b)** Mode 1 LC2 **(c)** Mode 1 LC3

(d) Mode 2 LC1 **(e)** Mode 2 LC2 **(f)** Mode 2 LC3

(g) Mode 3 LC1 **(h)** Mode 3 LC2 **(i)** Mode 3 LC3

Figure 8.5: Modes 1-3 used as initial imperfections, scaled 15 times.

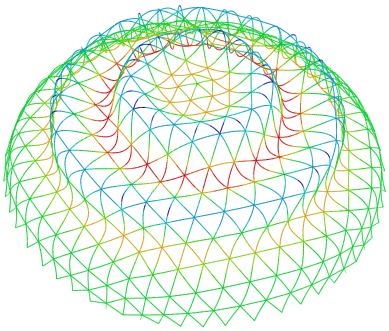

(a) Mode 4 LC1

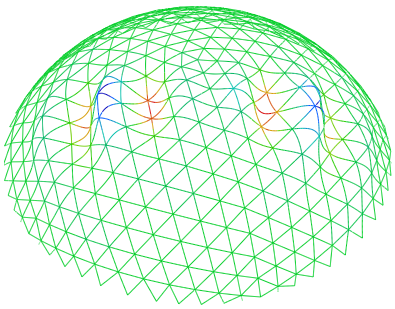

(b) Mode 4 LC2

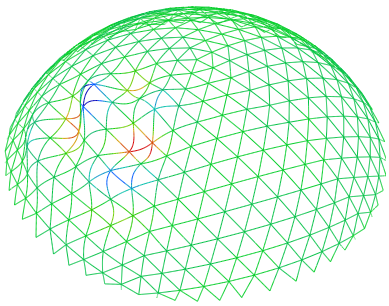

(c) Mode 4 LC3

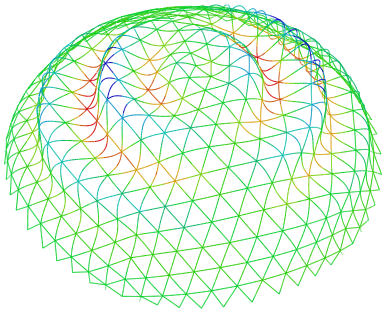

(d) Mode 5 LC1

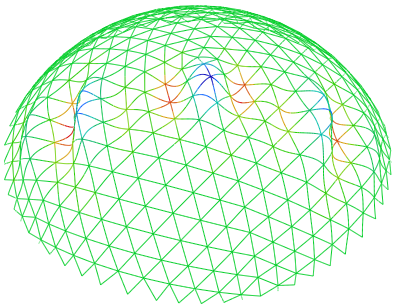

(e) Mode 5 LC2

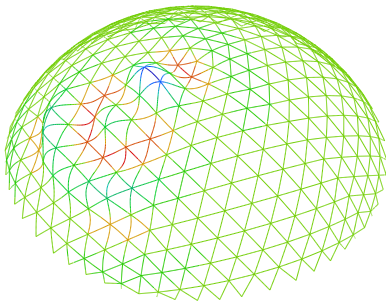

(f) Mode 5 LC3

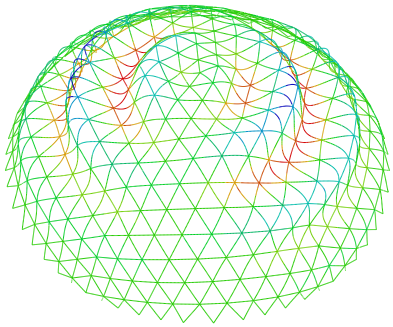

(g) Mode 6 LC1

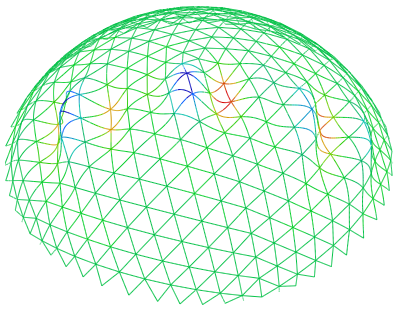

(h) Mode 6 LC2

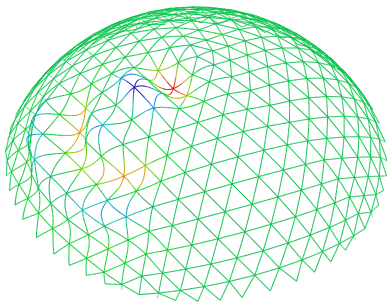

(i) Mode 6 LC3

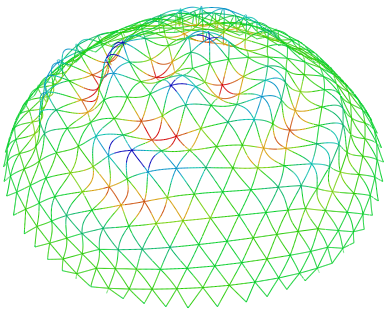

(j) Mode 7 LC1

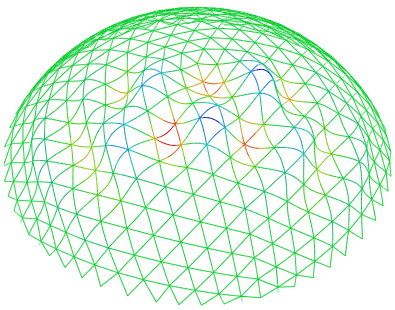

(k) Mode 7 LC2

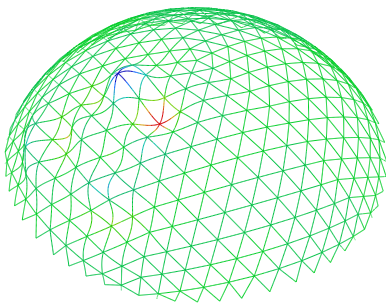

(l) Mode 7 LC3

Figure 8.6: Modes 4-7 used as initial imperfections, scaled 15 times.

Figure 8.7 show the sensitivity to imperfections depending on size and mode shape. From the tests it was concluded that, generally, the capacity was reduced as the size of the initial imperfection increased.

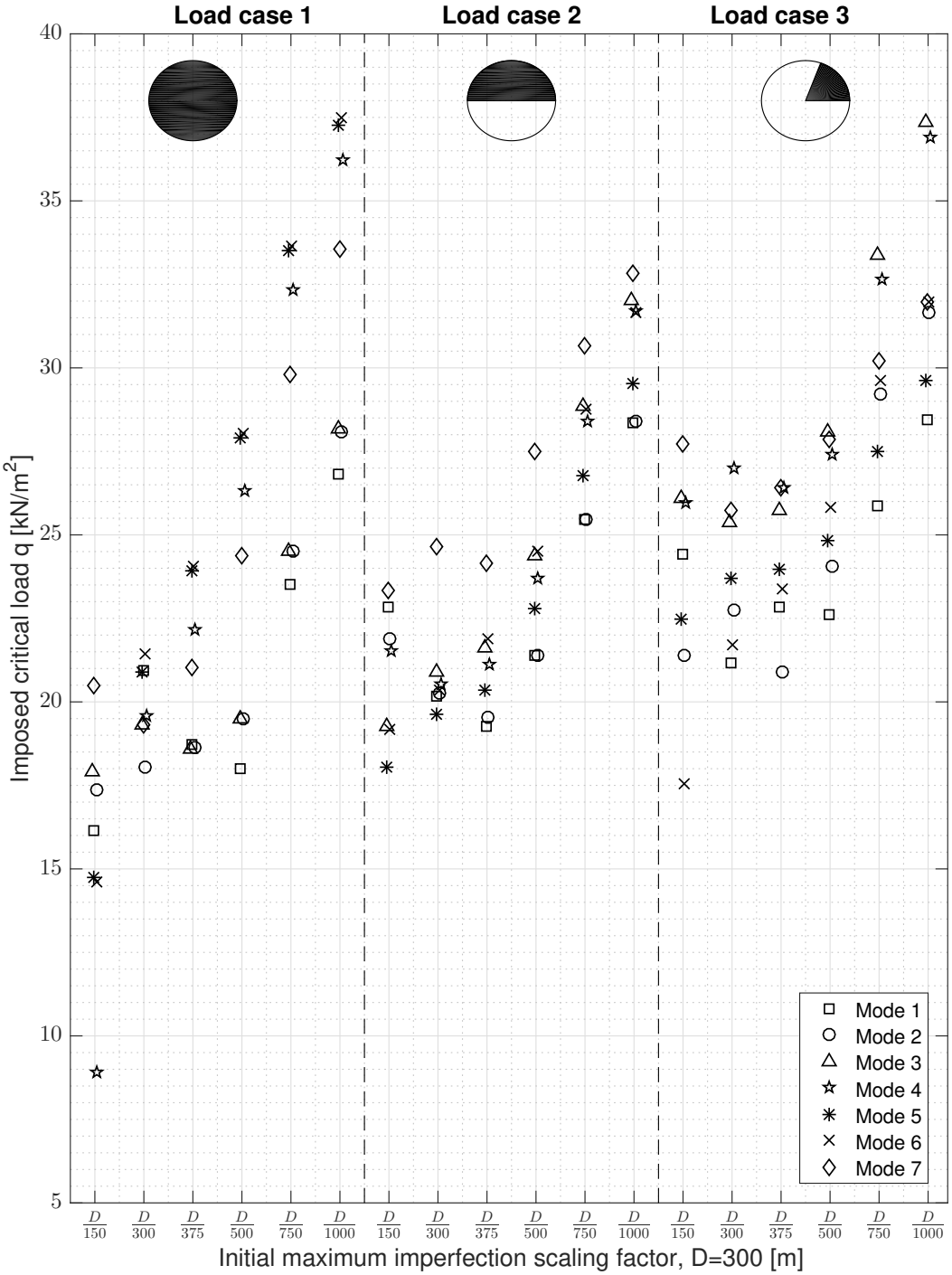

Figure 8.7: Imposed failure load when taking imperfections into account. Mode shapes 1-7 and initial imperfection D/300-D/1000. Note that the self weight, $q_{sw} = 2.2$ kN/m^2, is not included.

When studying fig. 8.9a and fig. 8.9b it can be seen that the lowest ratios q/q_{linear} were 0.135, 0.295, and 0.231 in order of the load cases. This corresponded to imposed failure loads of 8.9, 18.0, and 17.5 kN/m^2.

It is often stated that reticulated structures are particularly sensitive to asymmetrical load cases. However, such a trend was not found either at a relative critical level or at critical imposed load level. This sensitivity may be caused by the low self weight of common shells, as low as 0.25 kN/m^2 in short span reticulated metallic shells[2], but up to 0.8[1] kN/m^2 in the Houston Astrodome, also in steel. In contrast, the self weight of this dome was estimated to 2.2 kN/m^2, which could increase the capacity in asymmetric loading scenarios. In fig. 8.7 it can be seen that the remaining capacity in load case 1 and 2 were similar, while the critical loads in load case 3 were slightly higher, echoed by their corresponding median values of 24.1, 24.2, and 27.4 kN/m^2, respectively.

A general trend of the critical load at a mode-shape-level was difficult to observe, noting that mode shape 4, for instance, in load case 1 increased almost linearly, while mode 2 in load case two initially decreased when the imperfection decreased. The reason for this could be the infinite number of load paths that exist, as discussed in section 4.1.3. In addition, the location of the failure changes depending on the size of the imperfection as well as the sign of the initial imperfection factor.

The size of the initial imperfection also affects the stiffness of the dome. It was observed that, in almost every case, a smaller imperfection increased the stiffness. This effect can be found in appendix in fig. A3-A7. In addition, in cases where a lower critical load was found, despite a smaller initial imperfection, such as in load case 2 mode shape 1, seen in fig. 8.8, the stiffness of the structure was increased when the imperfection decreased. It was also seen that the non-linearity of the load-deflection curves was reduced along with a reduction in the initial imperfection.

The initial imperfection thus increases the deflection by lowering the stiffness, as well as causing a significant reduction in the imposed load when compared to linear buckling.

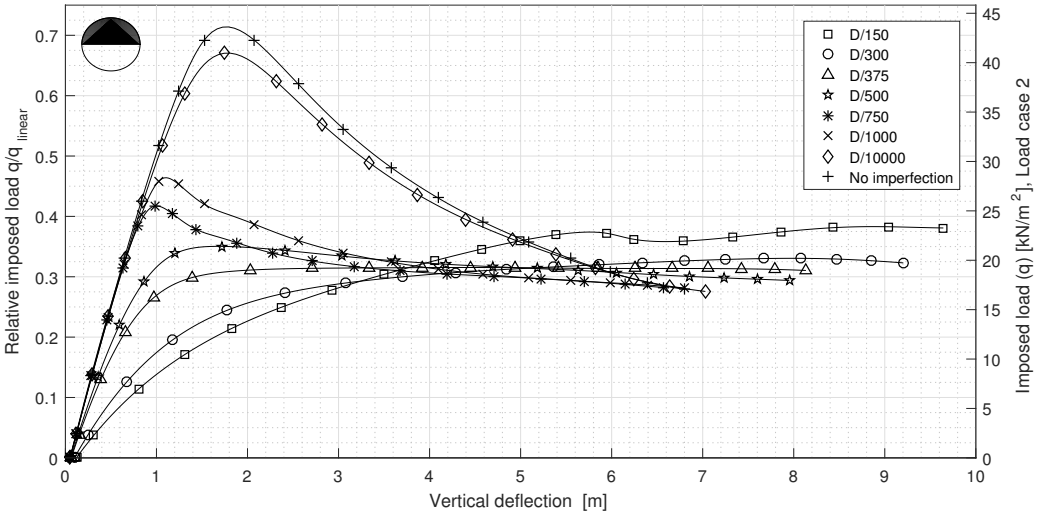

Figure 8.8: Load deflection curves for mode shape 1, fig. 8.5b, in load case 2. Initial imperfections D/150 to no imperfection.

The lower bound critical load values from fig. 8.7 can be seen in fig. 8.9b, where it can be seen that load case 1 had the lowest limit load. However, the second load case will be the most critical when considering the design load is double that of load case 1, to account for snow accumulation. Regardless of load case, the stability failure loads remain above the design load of 2 and 4 kN/m^2 respectively. It was stated in section 4.4.3 that mode shape one will not always induce the most severe reduction from the linear buckling load, which was replicated in this study where it had the largest impact in 11 out of 18 cases, fig. 8.9. The outliers (mode shape 4 in load case 1, mode shape 5 in load case 2, and mode shape 6 in load case 3) suggest that other mode shapes should be included when introducing through failure modes.

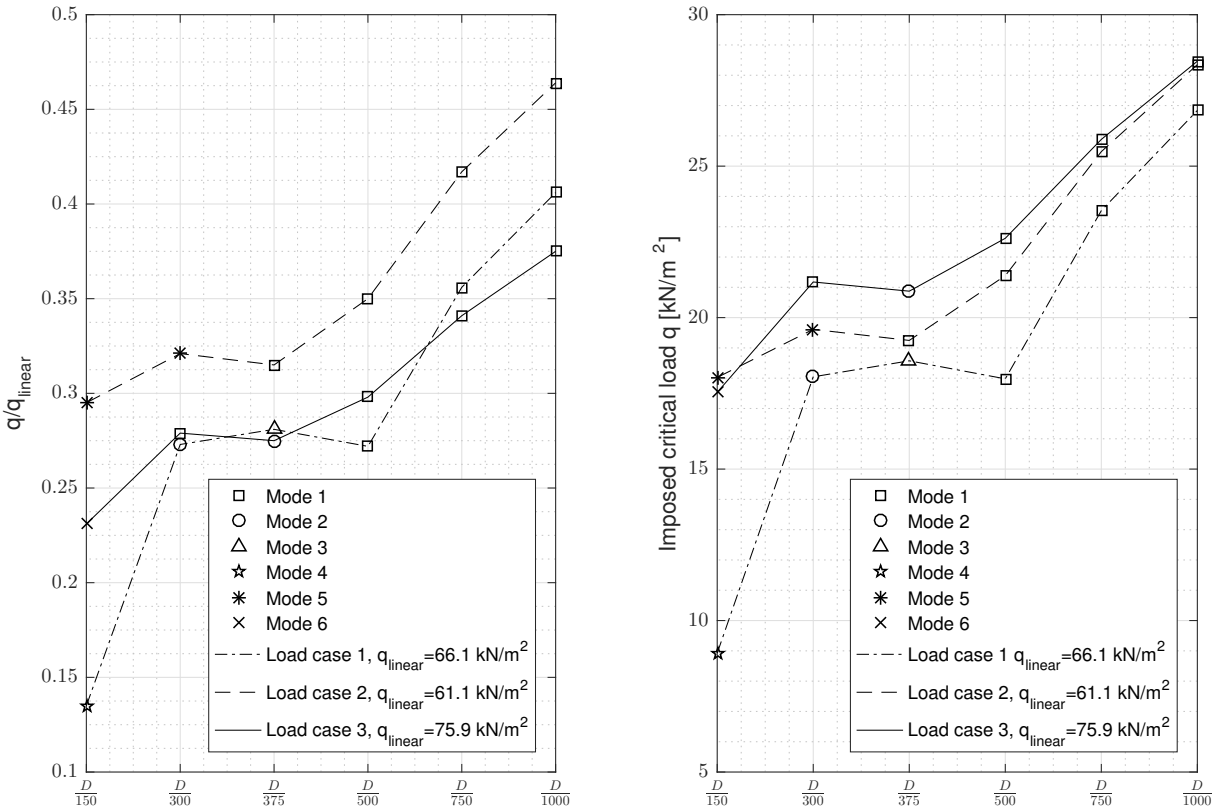

(a) Lowest ratio depending om mode shape and imperfection

(b) Worst instances of imposed critical load depending om mode shape and imperfection

Figure 8.9: Lowest imposed failure load for each initial imperfection and corresponding mode shape, for all three load cases, extracted from fig. A1 and fig. 8.7.

The sensitivity to imperfections should be translated into erection tolerances to ensure two things. First, that a sufficiently high critical load can be assured, and secondly that the stiffness of the dome remains high. The maximum initial imperfection is contingent on what the contractor can guarantee, but it can be seen that a construction error of D/150, corresponding to 2 metres, should be avoided. Note that $D/750$, 0.4 metres, may be advantageous as tolerances better than this would only improve the performance.

8.4 Creep

The deformation caused by creep was studied parametrically through variation of the modulus of elasticity, from 7 GPa to 10.8 GPa, for permanent loads, and restored to 10.8 GPa for imposed loads. This was done for a perfect geometry without any imperfections.

The load-deflection curves in each load case can be seen in fig. 8.10 - 8.12. It can be seen that creep lowered the critical capacity by Δq in all three load cases, from 46.0 to 37.5, 42.5 to 34.7, and 39.3 to 29.9 kN/m^2, in load case 1-3, respectively. Meaning a lower bound relative capacity of 56.8, 58.7, and 39.4 % in load cases 1-3 when compared to the linear buckling value corresponding to each load case, and 81.5, 81.6, 76.1 % if instead compared to the upper bound non-linear limit point. Creep alone thus reduces the capacity by 18.5, 18.4, and 23.9 % in load case 1 to 3 when the Young's modulus was reduced from 10.8 to 7.0 GPa. These data points were summarised in table 8.3.

Table 8.3: Summarised result of the reduction of the elastic buckling load due to creep.

Load case	Δ q	$q_{creep}/q_{qr,linear}$ [%]	$q_{creep}/q_{qr,non-linear}$ [%]	Creep reduction [%]
1	8.5	56.8	81.5	18.5
2	7.8	58.7	81.6	18.4
3	9.3	39.4	76.1	23.9

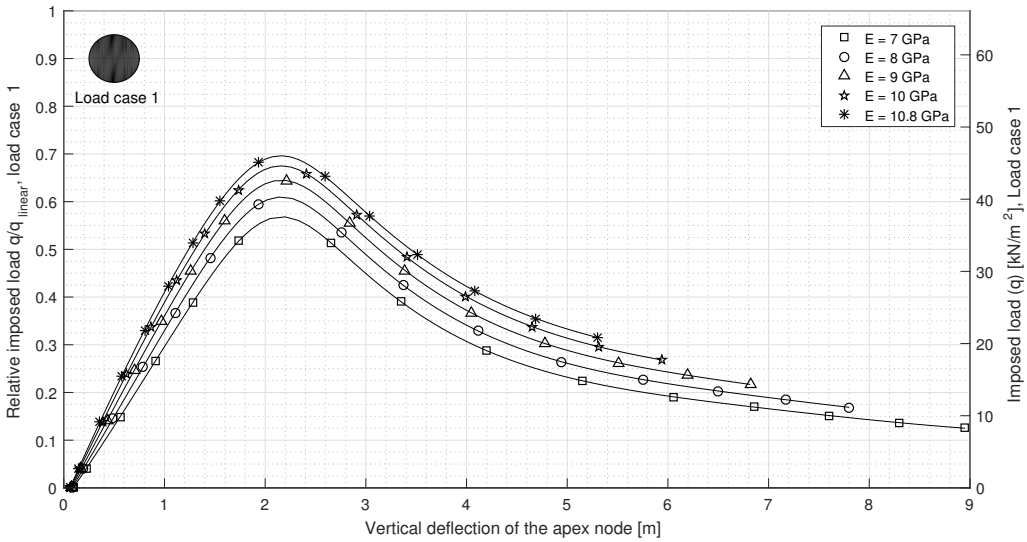

Figure 8.10: Parameter study of creep induced instability for various Young's modulus, load case 1.

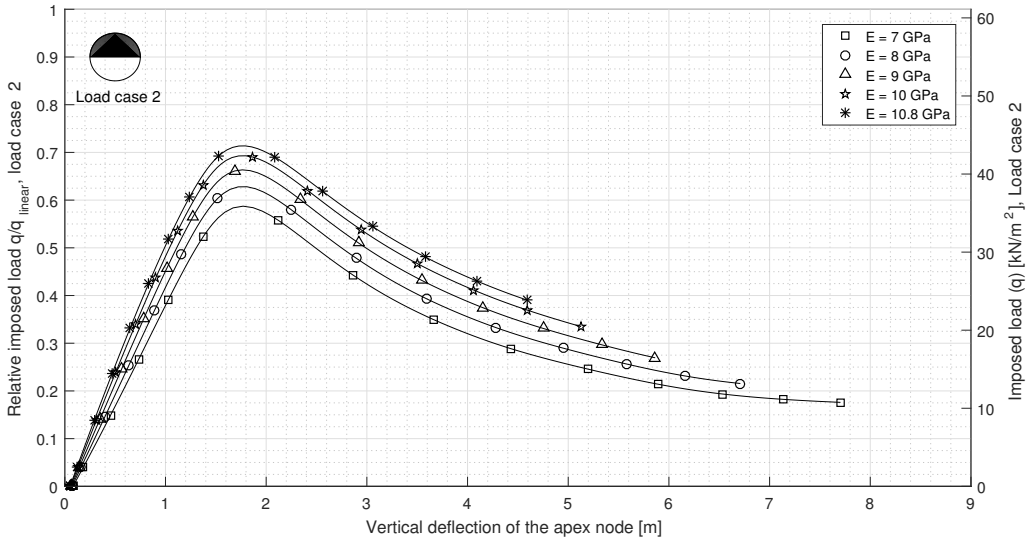

Figure 8.11: Parameter study of creep induced instability for various Young's modulus, load case 2.

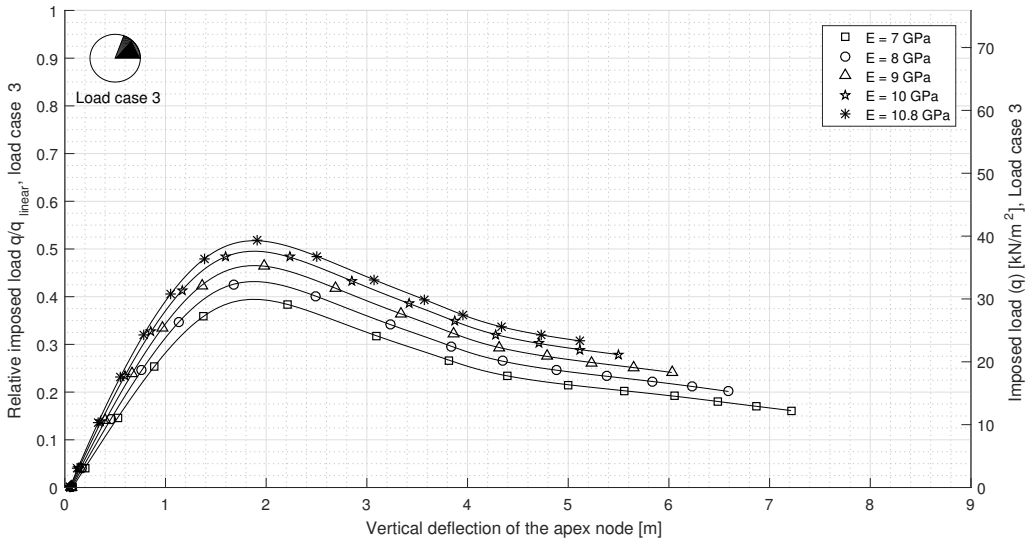

Figure 8.12: Parameter study of creep induced instability for various Young's modulus, load case 3.

As was shown here, creep reduced both the stiffness as well as the limit stability capacity and can therefore not be ignored when analysing reticulated shells. Creep buckling did however occur, for all values of E and for every load case, at loads, q, significantly higher than the imposed design loads of 2 an 4 kN/m^2. The reason why it still should be considered is its potential combined effect with other causes of failure, as imperfections for instance.

8.5 Imperfections and creep combined

The combined action of creep and imperfections was studied by performing non-linear analyses for the first seven mode shapes, each mode shape studied for six different initial scalers of imperfection, for all three load cases, while keeping the Young's modulus constant at 7 GPa for permanent loads and 10.8 GPa during imposed loading. The study covered both positive and negative mode shapes scaling factors, resulting in 252 data points. In fig. 8.13, the lowest imposed failure load for each mode shape and imperfection is presented.

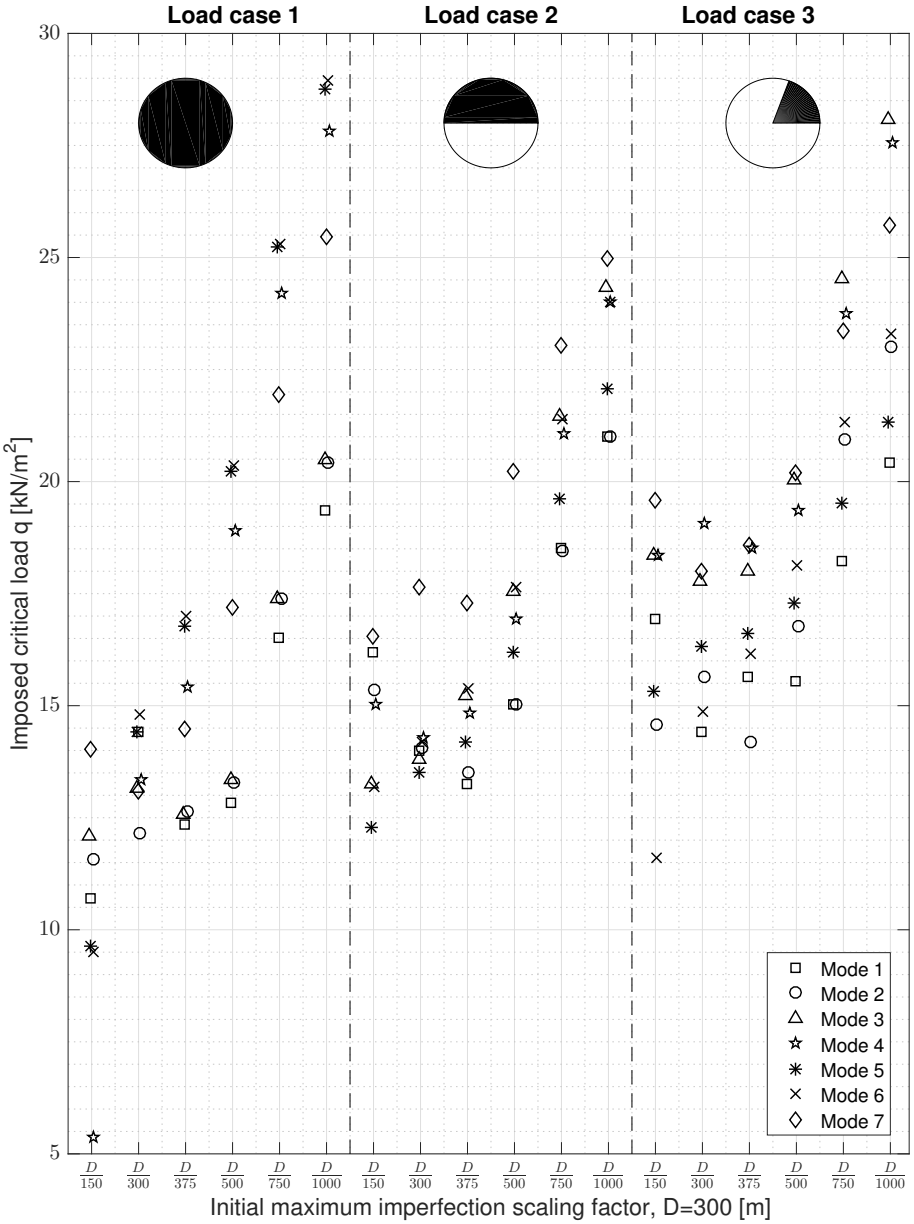

Figure 8.13: Imposed failure load when taking imperfections and creep into account by reducing the Young's modulus to 7 GPa for permanent loads. Mode shapes 1-7 and initial imperfection D/300-D/1000 for load cases 1-3. Note that the self weight, $q_{sw} = 2.2$ kN/m^2, is not included.

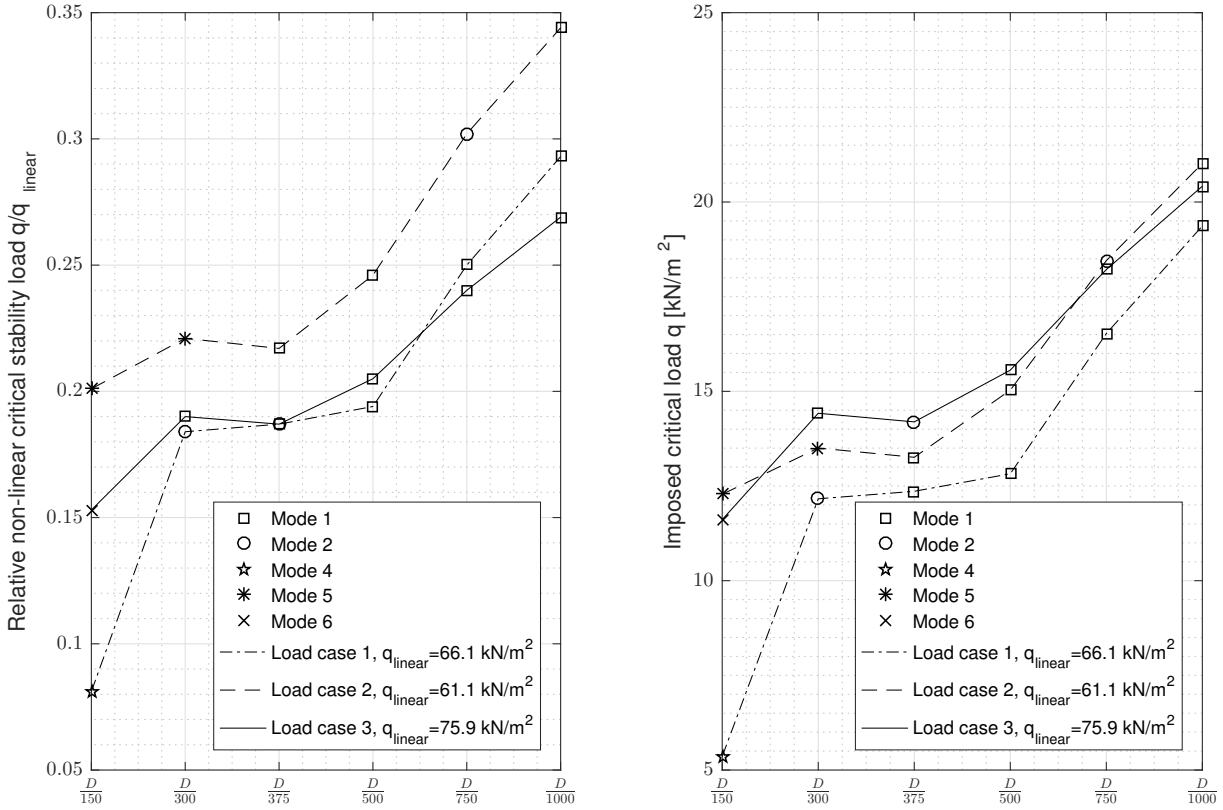

(a) Lowest ratio depending om mode shape and imperfection

(b) Worst instances of imposed critical load depending om mode shape and imperfection

Figure 8.14: Lowest imposed failure load for each initial imperfection and corresponding mode shape, for all three load cases, extracted from fig. A1 and fig. 8.7.

The reduction in capacity due to creep was established in section 8.4. The combined effect of creep and imperfections showed no synergistic effect, given the method used to study creep. The reduction in critical imposed load would have to increase, in comparison to creep alone, for there to be any such effect to be established. It appears that the effect of creep was reduced for larger imperfections, see fig. 8.15b. However, the smallest reduction was for mode shape 4 in load case 1, approximately 3.6 kN/m^2, as can be seen in fig. 8.15a. A similar pattern was also found in the other two load cases, see fig. A8.

The fact that creep dominated the reduction for small imperfections is almost self evident. The initial deformed shape of the dome tends towards the geometry without any mode-shape-induced imperfections as the imperfections get smaller. The reverse, a totally diminished effect from creep would likely not occur even for imperfections outside the chosen interval. It would appear as if, at least for the studied Young's modulus equal to 7 GPa, the creep deformation and the mode shape imperfections add to the reduction of the critical load. This relationship could be simplfied to: large deformations reduces the effect from creep.

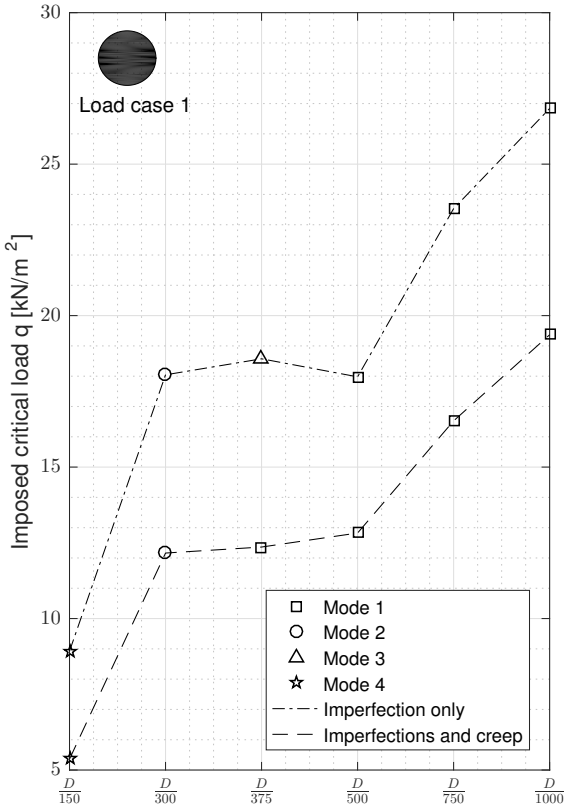

(a) Lowest critical loads in Load case 1, imperfections vs imperfection and creep, extracted from fig. 8.7 and fig. 8.13

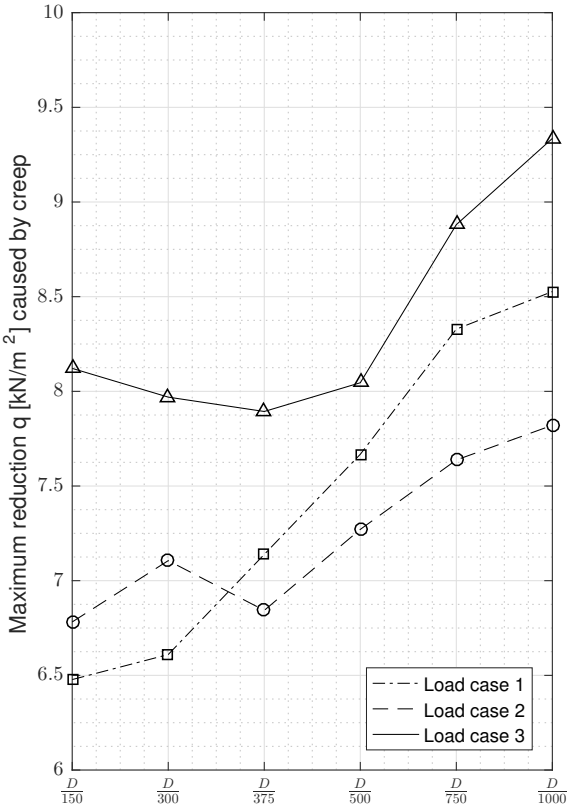

(b) Max creep reduction for each mode shape and all three load cases, studying possible synergistic effect between creep and imperfection

Figure 8.15: Comparison of reduction due to creep.

8.6 Settlements

Radial settlement

Stability failure due to radial settlement was investigated for a perfect geometry, presented in fig. 8.16-8.17. The cross sections used are presented in table 8.4.

Table 8.4: Relative axial stiffness in relation to the largest cross section 5x5.

Cross section [mxm]	0.5x0.5	0.8x0.8	1x1	1.5x1.5	2x2	3x3	5x5
Rel. axial stiffness	0.01	0.0256	0.04	0.09	0.16	0.36	1

Figure 8.16 shows the radial settlement for all ring sections under loading until failure. The

weakest ring, a relative stiffness of 0.01, expands radially up to roughly 6 meters before elastic failure. The expansion is drastically reduced, in combination of an increased failure load, when the cross section increases. A relative stiffness of 0.09 and higher yields failure load equal to the one of a perfect geometry, without modelling settlement.

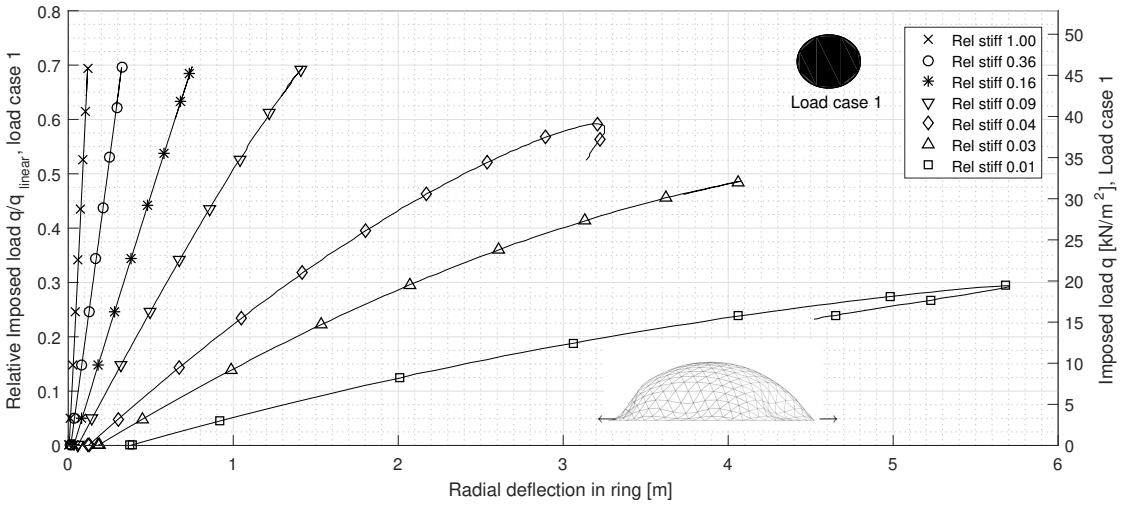

Figure 8.16: Load path curve showing the radial settlements during loading of imposed load for various base ring elements. The dome geometry has no imperfections and load case 1 is applied.

Figure 8.17 shows the vertical displacement of the apex node during the same simulation as for fig. 8.16. The results shows a decreased stiffness for smaller cross sections, but for 1.5x1.5 and larger, the difference in stiffness becomes smaller. The decreased level of failure load for cross sections corresponding to relative stiffness 0.01, 0.03, and 0.04 is likely due to different failure modes induced by the slender ring. The smaller cross sections cause a general snapping near the base, as opposed to the apex snapping which occurred for the larger cross sections.

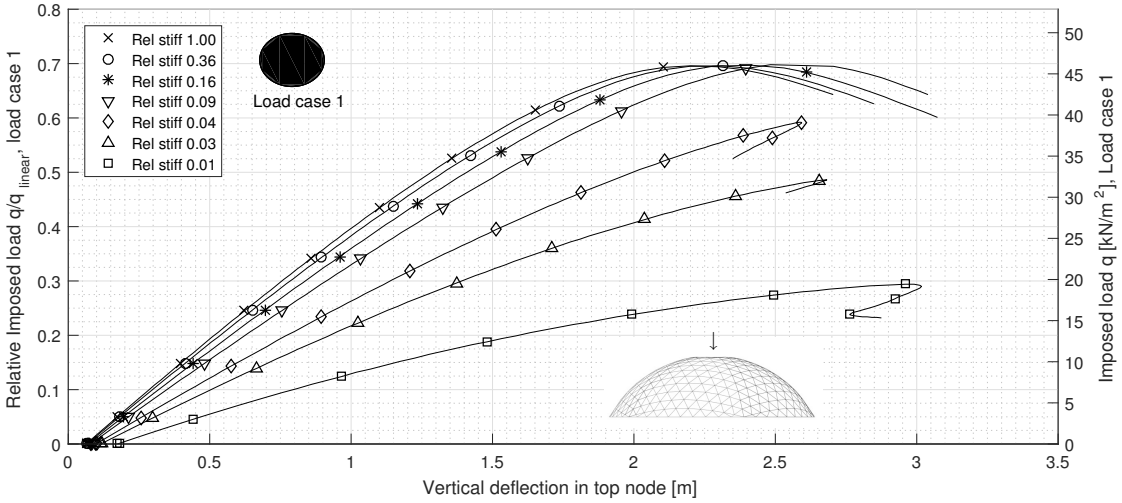

Figure 8.17: Load path curve showing the vertical displacement of the apex node during loading of imposed load for various base ring elements. The dome geometry has no imperfections and load case 1 is applied.

When the same model was given imperfections by its first linear mode shape and a magnitude of $D/300$, the difference in results became less significant. Generally, the elastic stability failure load level stays close to the results reviewed earlier in section 8.3, as can seen in both fig. 8.18 and fig. 8.19.

In fig. 8.18, the radial displacement is presented. Not only are the ring expansions smaller before undergoing failure, but this time it is only the smallest cross section, 0.5x0.5, that yields a decreased failure load.

When studying fig. 8.19, the load paths for all ring elements, except for the most slender one, nearly coincide with each other. From this graph it can be seen that the impact of settlement, when imperfection is added, is negligible.

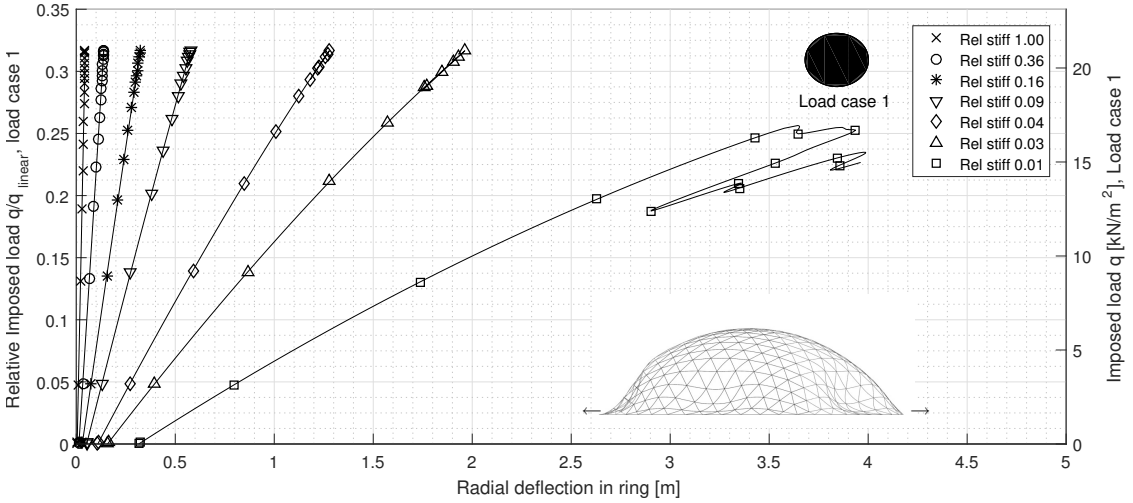

Figure 8.18: Load path curve showing the radial settlements during loading of imposed load for various base ring elements. Mode shape 1, D/300, is applied as imperfection and load case 1 is in action

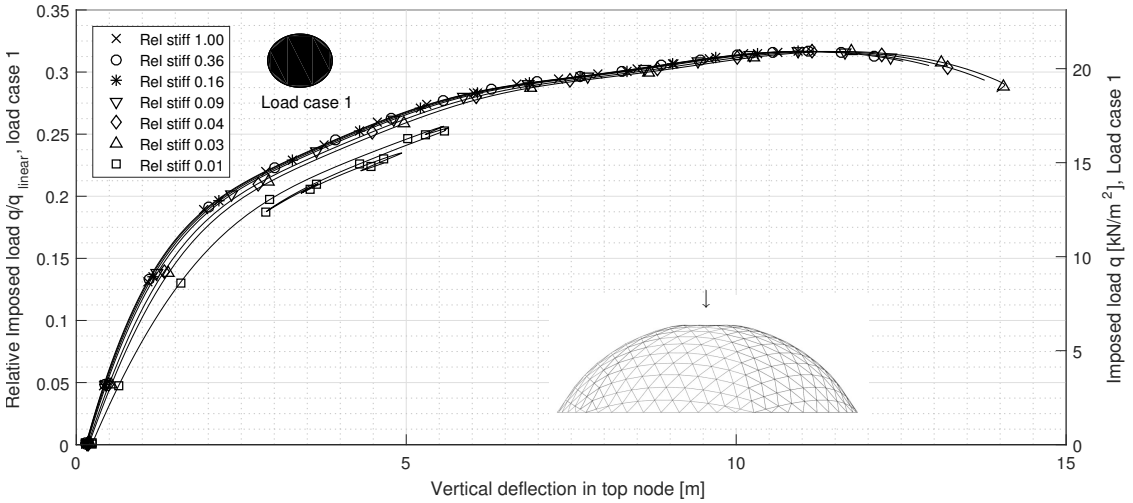

Figure 8.19: Load path curve showing the vertical displacement of the apex node during loading of imposed load for various base ring elements. Mode shape 1, D/300, is applied as imperfection and load case 1 is used.

Differential settlement

The differential settlement was implemented through displacement controlled base nodes. The maximum settlement used in each case was ranging from 0.01 to 2 m and the results are presented in fig. 8.20 and fig. 8.21 where the latter figure shows the effect of combined imperfection and settlement. As opposed to load case 1 used in radial settlement, load case 2 was instead used in this parameter study, as this case was expected to be more critical in this study.

The results of elastic stability from a differential settlement of a dome with perfect geometry are presented in fig. 8.20. The vertical displacement of a node near apex, were stability snapping occured, is plotted against the imposed load applied.

The load path curves for each settlement seem to coincide close to each other, albeit the slight offset sideways for larger settlements. Even in its most extreme case of 2 meter in maximum settlement, the collapse load is merely slightly less than the others.

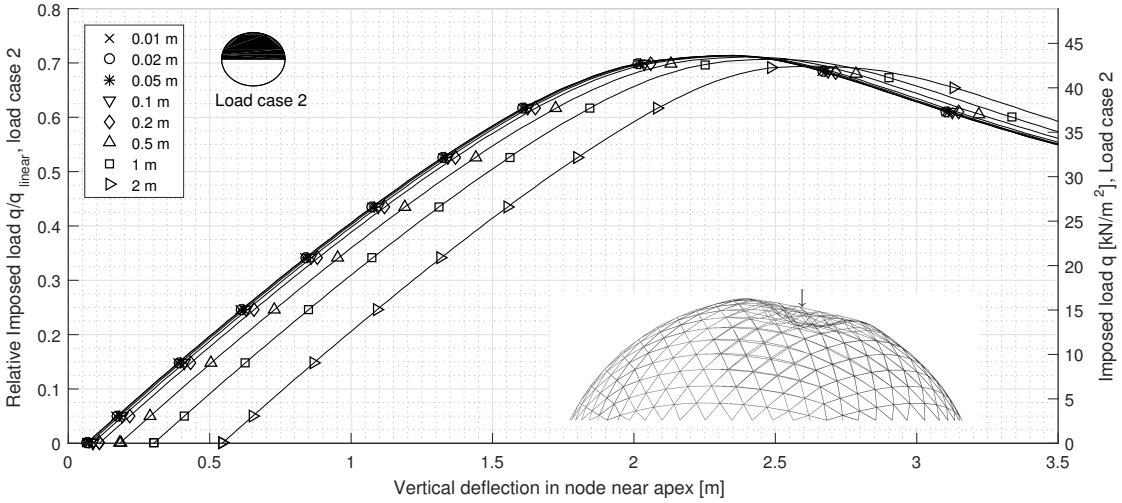

Figure 8.20: Load path curve showing the vertical displacement of worst displaced node near dome apex. No imperfection added and load case 2 is used.

In fig. 8.21, mode shape 1 of load case 2 was applied, with an imperfection of D/300 and new load paths were created. Again, the the results stay close to the achieved load paths presented in fig. 8.8 when studying imperfections alone. Only the worst case of settlement of 2 meters shows a deviation of roughly 5 % from the other test results.

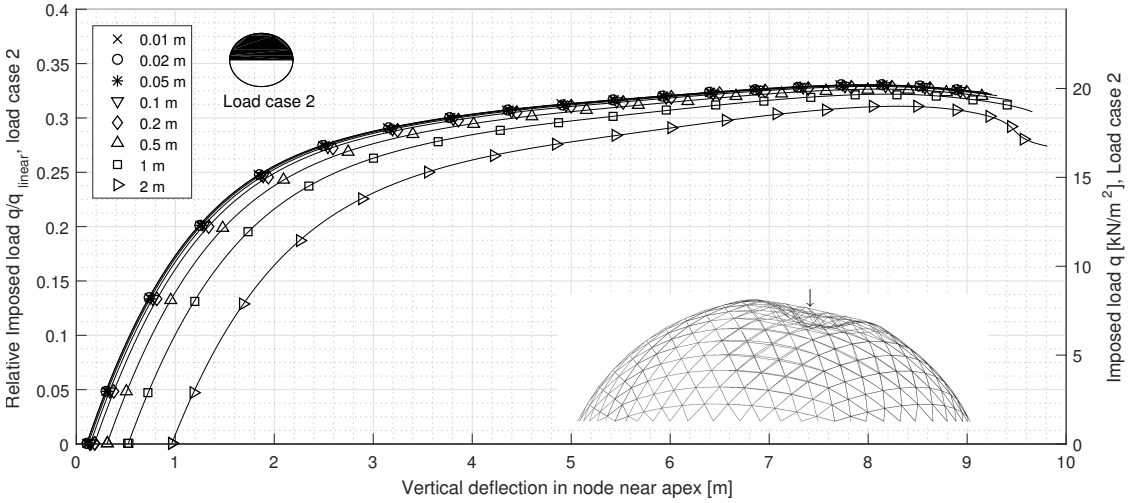

Figure 8.21: Load path curve showing the vertical displacement of worst displaced node near dome apex. Mode shape 1, D/300, is applied and load case 2 is used.

Chapter 9

Result and discussion of ULS analysis

9.1 Stresses with imperfections

The stresses have to be known in order to determine if material failure occurs prior to the loss of stability. The stresses caused by the third order moment and normal forces have been plotted in fig. 9.1-9.3. An increased imperfection clearly causes the stresses to increase as well, primarily through a larger moment. The normal stress remained almost constant in each load case, apart from a few instances when the initial imperfection was D/150, and did not increase drastically when the imposed load was doubled.

The asymmetrical load cases, 2 and 3, induced the highest stresses. The only case when that did not occur was for mode shape number 4 with an imperfection of D/150, see fig. 8.6a, the mode shape and imperfection with the lowest stability load (see fig. 8.9).

The maximum stress caused by mode shape 4, see fig. 8.6a, and imperfection can be seen in fig. 9.3. The mode shape causes considerable moment, comparable to the asymmetrical load cases. This might be the reason its critical stability load is so much lower - it forces the structure to act more via bending action, rather than through membrane action, at least more so than any other mode shape.

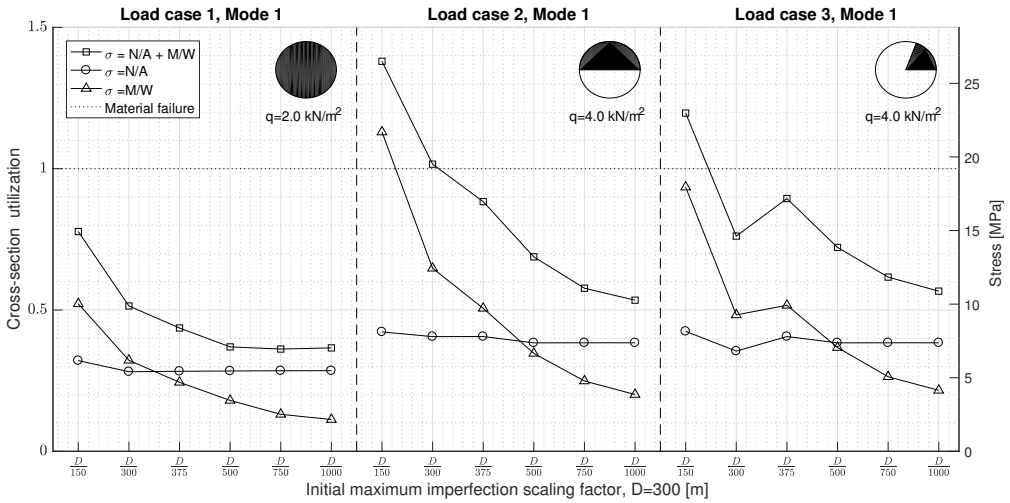

Figure 9.1: Utilization and stresses as a function of the mode shape 1 imperfections in fig. 8.5a-8.5c. Note that $\sigma = N/A + M/W$ is the most utilized cross section for a given imperfection and load case, whereas N/A and M/W only highlight the worst instance of normal force and moment, respectively, irrespective of location.

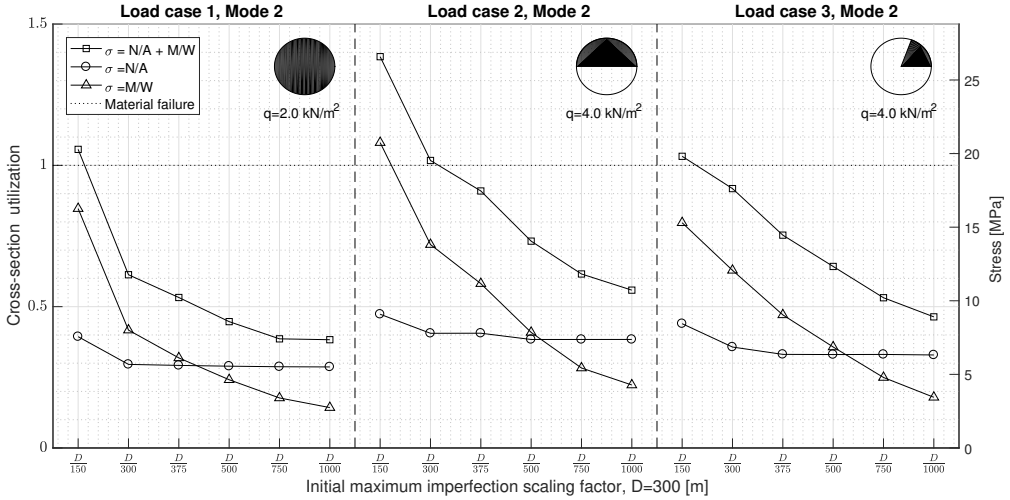

Figure 9.2: Utilization and stresses as a function of the mode shape 2 imperfections in fig. 8.5d-8.5f. Note that $\sigma = N/A + M/W$ is the most utilized cross section for a given imperfection and load case, whereas N/A and M/W only highlight the worst instance of normal force and moment, respectively, irrespective of location.

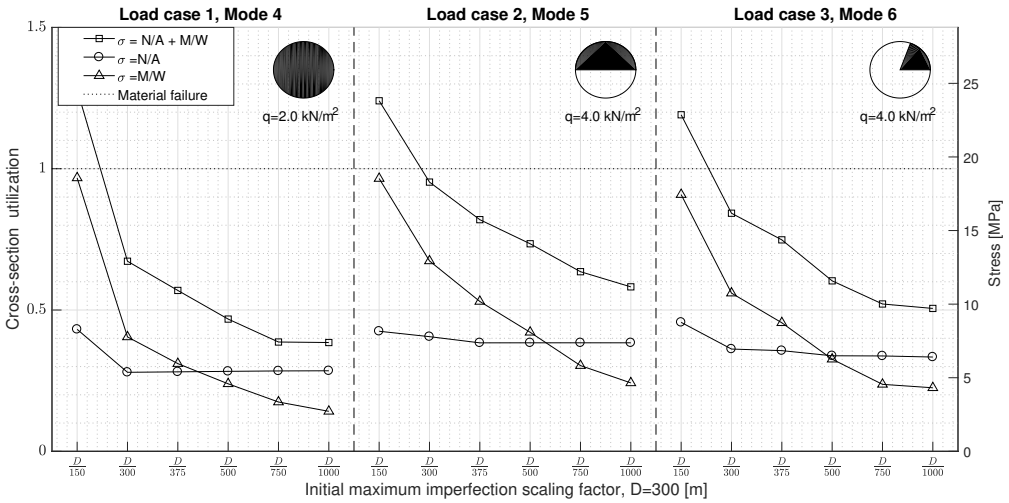

Figure 9.3: Utilization and stresses as a function of the mode shapes imperfections 4-6 in fig. 8.6a, 8.6e, and 8.6i . Note that $\sigma = N/A + M/W$ is the most utilized cross section for a given imperfection and load case, whereas N/A and M/W only highlight the worst instance of normal force and moment, respectively, irrespective of location.

The imperfections cause the stresses to increase through bending. It is thus important, just like in the discussion in section 8.3 with imperfections relating to stability, to reduce the imperfections during construction, perhaps even more so. The calculated stresses only account for normal forces and bending moments. Stresses caused by other phenomena could possibly make it necessary to put even more stringent demands on the construction errors, below D/300 seems reasonable, possibly even lower to obtain a satisfactory margin of safety.

9.2 Bending moment in the connections

The bending moments for a reduced amount of modal imperfections have been studied and can be seen in fig. 9.4. The bending moment was sensitive to the initial imperfection, with values over 5 MNm in all three load cases. It also seemed, perhaps unsurprisingly so, that there was an increase in bending moment when the load was asymmetrical, in load case 2 and 3. It is perhaps worth noting that the bending capacity of the beams was calculated to 6.55 MNm, so imperfections over D/375 should be regarded as unacceptable. This means that if the size of the initial imperfections is $<$ D/375 failure is likely to occur due to instability rather than reached material strength.

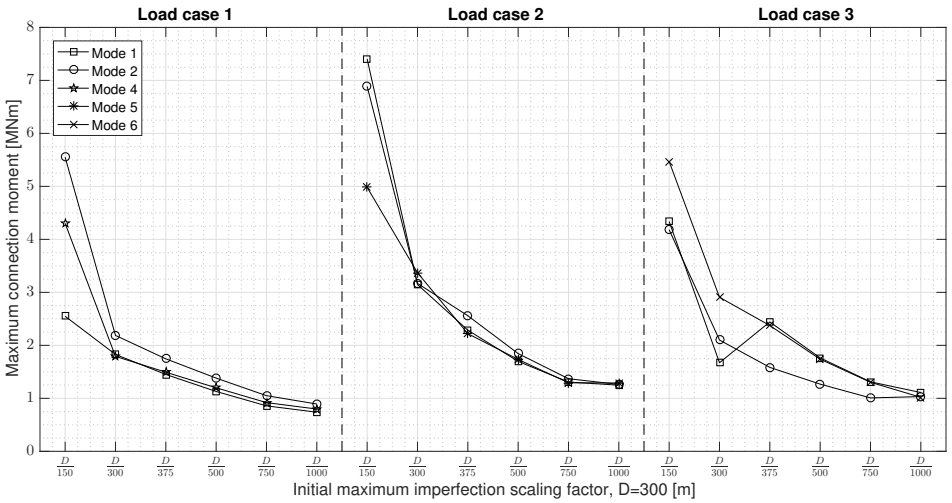

Figure 9.4: Maximum moment in the connections in load case 1-3 using mode shape imperfections 1,2,4-6 found in fig. 8.5a-8.5c, fig. 8.5d-8.5f, fig. 8.6a, 8.6e, and 8.6i.

The connections in the Brindisi domes can be seen in fig. 9.5a, and the connection type is explained in fig. 9.5b. The capacity in the connection was determined to approximately 900 kNm, according to Crocetti[65]. The height of the Brindisi beams is 1.13 metres, compared to 1.60 metres in this report. Hand calculations in combination with laboratory tests would need to be performed in order to determine how much more the bending capacity could be increased.

(a) Connection in one of the Brindisi domes, from R. Crocetti[65].

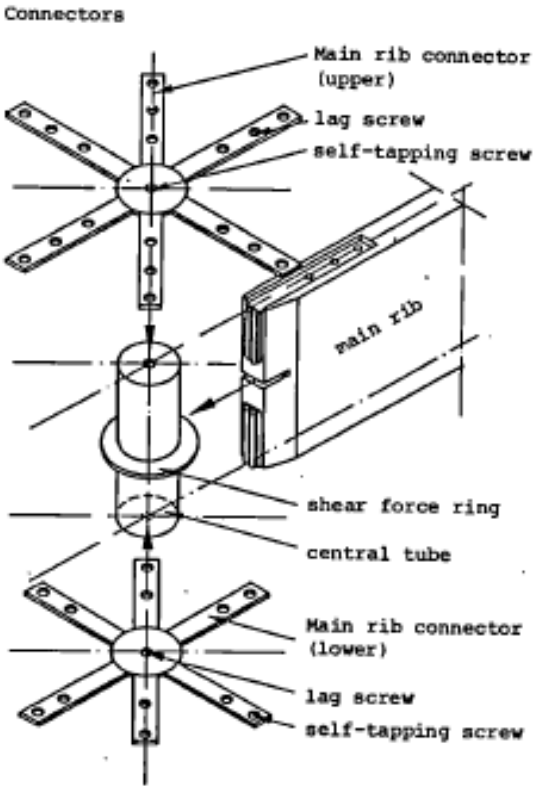

(b) Connection explanation, from A. Jorissen[17].

Figure 9.5: Possible connector.

9.2.1 A comparison of force distribution - Theory VS. Numerical

The theory concerning the distribution of meridian and hoop forces in a reticulated shell was compared with the corresponding member forces obtained in the computational model. By using the same dimensions and both self weight and snow load, the forces were plotted from the apex to the base, seen in fig. 9.6 and fig. 9.7.

When comparing the force along the meridian in fig. 9.6, it can be seen how the theoretical curve to the left ranges from approximately 5 MN to almost 6 MN. In fig. 9.6b, the member forces from Abaqus ranges from 3 MN at the apex to 4 MN at the base, while peaking roughly 5 MN on a 30 metres height.

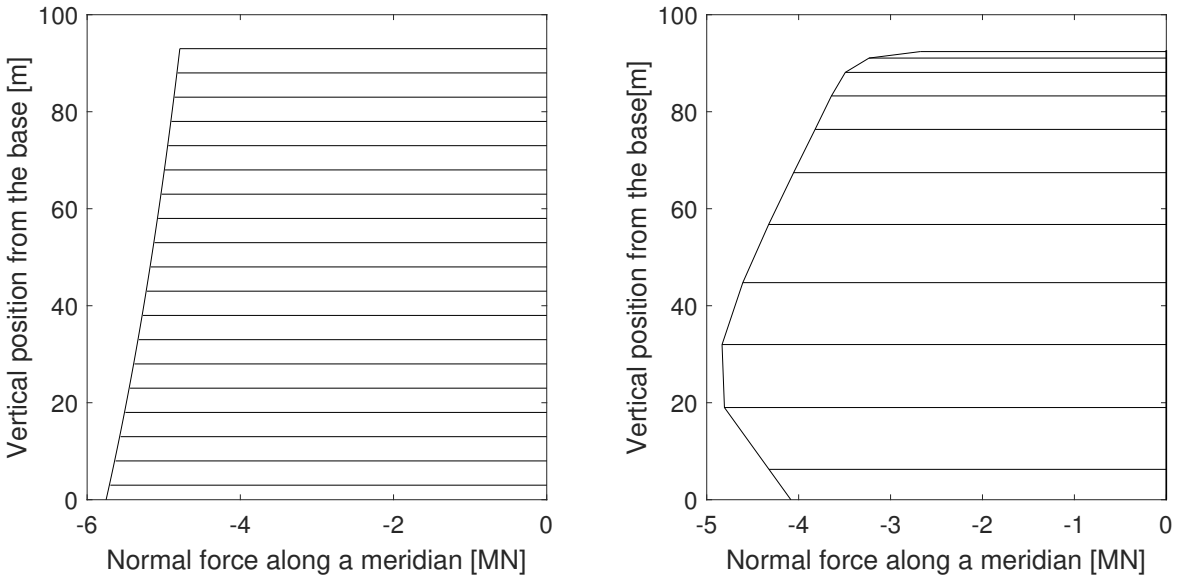

(a) According to formulas **(b)** According to Abaqus

Figure 9.6: A comparison of meridional forces from the apex to the base.

The result of the hoop force distribution is presented in fig. 9.7, where fig. 9.7a shows the distribution of the theoretical curve, previously presented in chapter 3. The theoretical distribution ranges from negative 5 MN at the apex, to positive 3 MN at the base, meaning a change from compression to tension along the dome. A similar behaviour was observed in the numerical analysis, seen in fig. 9.7b. The force distribution ranged from negative 3.5 MN to positive 1 MN, significantly lower than the theoretical. The point of transition from compression to tension is also located higher in the numerical analysis.

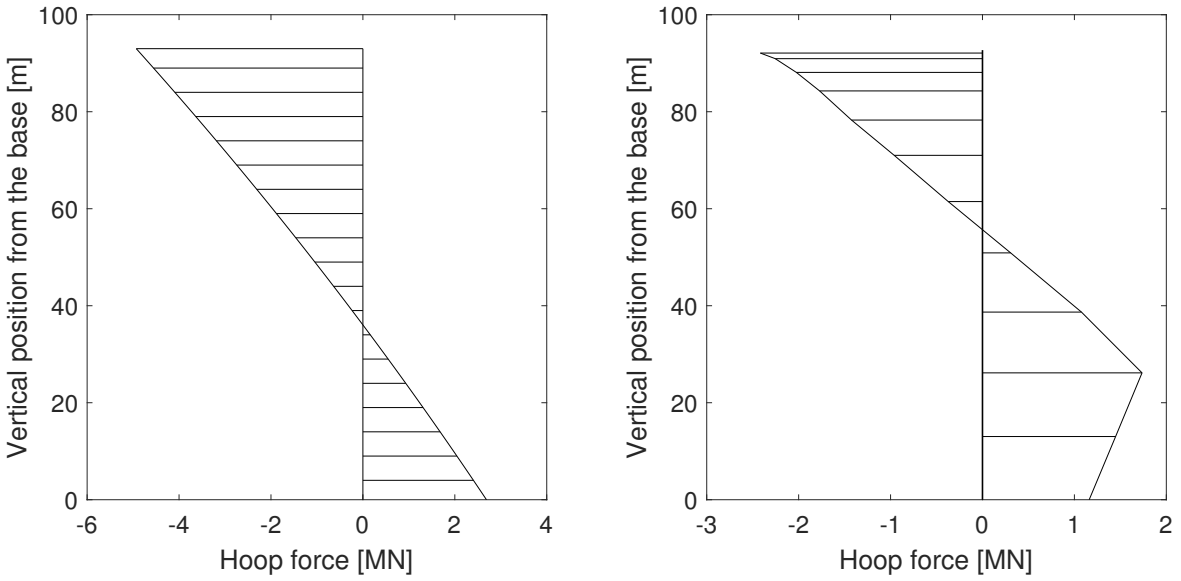

(a) According to formulas **(b)** According to Abaqus

Figure 9.7: A comparison of hoop forces from the apex to the base.

In summary, the forces gained when tracing the members along the meridian in Abaqus, did not reach the values achieved by formulas, nor was the shape of the distribution curve completely coinciding for neither meridian forces or hoop forces. There are arguably some similarities concerning the curves. The meridian force increased towards the base and the hoop force transitioned from compression to tension, just as the theory predicted. Another detail is the decrease of force near the base in the numerical analysis, for both the meridian and the hoop cases. The reason for this could possibly be that stiffness is not the same in all directions, as is assumed in the theoretical formulas, leading to different load paths. Another possible reason could be the assumed influence width is different in reality, and possibly not constant, as was assumed.

Chapter 10

Conclusions

Research question formulation

- Which dome geometry is most suitable to cover a span of 300 metres?
- How sensitive is a geodesic timber dome to imperfections applied in the shape of eigenmodes?
- If so, is there an easy/fast way to determine the non-linear elastic stability capacity, or does it require the study of several mode shapes?
- Can hand calculations accurately estimate the stability load?
- Can hand calculations accurately estimate the forces and the bending moments?
- How does creep influence the non-linear elastic stability capacity?
- How does the combined effect of creep and imperfections influence the non-linear elastic stability capacity?
- Does radial ring displacement/settlement negatively effect the elastic stability?
- Do differential settlements negatively effect the elastic stability?
- **Is it feasible to build a timber dome with a span of 300 metres when non-linear elastic stability and material failure is taken into account**?

The Geodesic arrangement was chosen based on the lower deviation of member lengths, the lower number of unique element lengths, and the higher linear buckling value in both load case 1 and 2.

The geodesic dome was very sensitive to imperfections, and the capacity and stiffness were reduced as the initial imperfections increased. It does however require many simulations to create a lower bound failure envelope, and it should be noted that it was not always the first eigenshape that produced the biggest reduction rate.

The study used cross sections that were estimated by help of hand calculations, which themselves did not deviate far too much from the numerical results. While the estimated normal forces never quite reached the values from the simulation, the buckling load did on the other hand end up close to its correspondent. The experience of using the formulas concludes that they work well considering the complexity of the structure, but should be taken with care, and should always be compared to secondary source. An issue was the limitation in load cases, where an asymmetrical snow load was not possible to calculate by hand.

Creep caused the structure to deflect symmetrically downwards, increasing deflection as the Young's modulus decreased. The structure subsequently lost stiffness and the elastic stability load decreased linearly. However, the reduction was less than the reduction caused by the geometrical imperfections. The capacity was further reduced when creep and imperfections were combined. However, the two did not have any synergistic effect. Meaning, the critical loads caused by only applying imperfections were always reduced by a value less than the maximum creep reduction in table 8.3.

The study has shown that settlements, both radially and vertically, cause little to none impact on the elastic stability, within the range investigated. Even when boundaries were pushed with seemingly extreme settlements, the difference in elastic collapse load was negligible. While it can be concluded that the elastic stability remains unaffected. It is, however, reasonable to suspect the stress distribution to be affected, possibly increasing the stresses such that the material strength capacity is insufficient. This would, however, require more information about the actual ground conditions in order to find a reasonable limit in total settlement.

The main question was whether this dome is feasible to build, primarily from a stability point of view, but also in terms of material failure. The critical stability safety factor, assuming rigid connections, was at least 2.5, 3, and 2.9, for the worst most severe initial imperfection in combination with the lowest Young's modulus in load case one, two and three, respectively. The global elastic stability for the Geodesic dome was studied thoroughly and a stability failure envelope was created. A global stability failure therefore seems to be unlikely.

The material failure was more critical with stresses reaching the utilisation limit at the given design loads. Given that many stress inducing factors remain to be studied, it cannot be said for certain that this cross section is suitable. However the stresses could remain within the capacity of the material, if stringent imperfection controls were implemented, or, if the dome was placed in a different snow zone, with a lower design load.

Chapter 11

Proposed further research

Connection fixity
The connections in the studied dome were assumed to be rigid. This was, of course, a simplification that needs to be studied further, specifically, would the global elastic stability be reduced significantly if there was some rotation in the connections? This should ideally be done in conjunction with a laboratory test regarding the rotational stiffness of the connection. It is, of course, possible to perform another parametric study, but the critical load in the range from pinned to fixed could be too large, other than possibly obtaining a lower bound value.

Rise to span ratio
The Geodesic dome proposed has a height of over 90 metres, which could create an unnecessarily large indoor volume or possibly cause problems during construction. It should therefore be studied how the rise and span ration relates to both the stability and the stresses, which has already be done for other geometries by Pan[23] and Bulenda[42]. They suggest that the dome will be less stable and that the stresses will increase.

Double layer
The cross-section used in this thesis was 0.8x1.6 (wxh), resulting in a quite heavy structure. Further, the main issue was the stresses induced by the bending moments and not the axial stress induced by the normal forces. It could therefore be possible to improve the utilization of the material by introducing a truss system, and thus creating a double-layer dome. Double-layer systems are less imperfection prone according to Gioncu[38], which needs to be verified for this particular geometry.

Bracing stiffness
The bracing was modelled with discrete points not allowing any rotation, this made the assumption that the roof structure could provide the necessary stiffness to support the bracing purlins. This should be looked at thoroughly because it is possible to get a torsional stability failure, which occurs at a lower imposed load, if this assumption is false.

Wind

Makowski[1] stated that any dome design should include the effect of wind. He also argued that it is difficult to predict the actual pressure distribution and that some assumed pressure distributions have turned out to be false in light of wind tunnel tests. The Eurocode[66] has a proposed wind distribution, it is however uncertain if it applies to such large scale structures. It is therefore pertinent to perform a wind tunnel test to understand the effect of wind.

Bibliography

[1] ZS. Makowski. "A history of the development of domes and a review of recent achievements world-wide". In: *Analysis, Design, and Construction of Braced Domes*. Nichols Publishing Company, 1984. Chap. 1.

[2] T.D. Wright. "Membrane forces and buckling in reticulated shells". In: *Journal of the structural division* 91.1 (1965), pp. 173–202.

[3] TRADA Technology Ltd. *Wide Span Wood Sport Structures*. URL: https://www.trada.co.uk/downloads/wide_span_wood_sports.pdf (visited on 01/31/2017).

[4] R. J. Ross et al. "Wood handbook: wood as an engineering material". In: (2010).

[5] R. H. White and M. A. Dietenberger. "Fire Safety of Wood Construction". In: *Wood handbook: wood as an engineering material*. Routledge, 2010. Chap. 18.

[6] T. Wierzbicki. *Lecture 10: Advanced Topic in Column Buckling*. 2013. URL: https://ocw.mit.edu/courses/mechanical-engineering/2-080j-structural-mechanics-fall-2013/course-notes/MIT2_080JF13_Lecture10.pdf (visited on 02/02/2017).

[7] A. G. Greenhill. *Determination of the greatest height consistent with stability that a vertical pole or mast can be made, and of the greatest height to which a tree of given proportions can grow*. publisher not identified, 1881.

[8] R. Crocetti. *Horisontalstabilisering och förband*. 2016. URL: https://www.youtube.com/watch?v=8P4nAwrr9SU (visited on 04/01/2017).

[9] Svenskt Trä. *Hållfasthetsklasser för limträ enligt SS-EN 14080:2013*. 2015. URL: http://www.svenskttra.se/siteassets/6-om-oss/publikationer/pdfer/hallfasthetsklasser-for_limtra.pdf (visited on 02/03/2017).

[10] M. Johansson. "Structural properties of sawn timber and engineered wood products". In: *Design of timber structures*. Swedish Forest Industries, 2015. Chap. 2.

[11] D. E. Kretschmann. "Mechanical Properties of Wood". In: *Wood handbook: wood as an engineering material*. Routledge, 2010. Chap. 5.

[12] J.M. Dinwoodie. *Timber: its nature and behaviour*. CRC Press, 2002.

[13] Swedish Standards Institute. *SS-EN 1995-1-1:2004 Eurocode 5: Design of timber structures – Part 1-1: General – Common rules and rules for buildings*. Swedish Standards Institute, 2004.

[14] Svenskt Trä. *Limträhandbok Del 1 - Fakta om limträ (Glulam Handbook Part 1)*. Svenskt Trä, 2016.

[15] R. Crocetti. "Fackverk". In: *Limträhandbok Del 2 - Projektering av limträkonstruktioner*. Svenskt Trä, 2016. Chap. 8.

[16] C. Williams. "What is a shell?" In: *Shell structures for architecture: form finding and optimization*. Routledge, 2014. Chap. 3.

[17] A. Jorissen. "Wooden Domes". In: *Commission of the European Communities industrial processes Building and Civil Engineering Timber structures*. Commission of the European Communities, 1989. Chap. V-4. ISBN: 92-825-9944-2.

[18] W.F Chen and E.M. Lui. "Space Frame Structures". In: *Handbook of Structural Engineering, Second Edition*. CRC Press, 2005. Chap. 24.

[19] G.R. Kiewitt. *Roof structure*. US Patent 2,908,236. 1959. URL: `https://www.google.com/patents/US2908236`.

[20] Geometrica. *Defining Domes*. 2017. URL: `http://www.geometrica.com/en/domes`.

[21] R. B. Fuller. *Building construction*. US Patent 2,682,235. 1954. URL: `https://www.google.com/patents/US2682235`.

[22] E. Lüning. "Timber Dome Structures - The history, geometry, calculation and erection of geodesic timber domes". In: (2009), pp. 87–103.

[23] D.H. Pan and U.A. Girhammar. "Influence of Geometrical Parameters on Behaviour of Reticulated Timber Domes". In: *International Journal of Space Structures* 18.2 (2003), pp. 105–121.

[24] N Lovecchio. *In Brindisi, the two largest domes in Europe*. URL: `https://building.closeupengineering.it/en/the-two-largest-domes-in-europe/245/` (visited on 01/31/2017).

[25] Y. Iimura et al. "Reticulated timber dome structural system using glulam with a low specific gravity and its scalability". In: *Proceedings of WCTE* (2006), pp. 6–10.

[26] P. Mullord. "Introduction to the analysis of braced domes". In: *Analysis, Design, and Construction of Braced Domes*. Nichols Publishing Company, 1984. Chap. 2.

[27] K.K. Mukhanov. *Design of metal structures*. Mir, 1968.

[28] L.A. Samuelson and S. Eggwertz. *Shell Stability Handbook*. Elsevier Science Publishers LTD, 1992.

[29] S. P. Timoshenko and J. M. Gere. *Theory of elastic stability*. 1961.

[30] Z.S. Makowski. "Shell analogies applied to the analysis of stress distribution in braced domes". In: *Analysis, Design, and Construction of Braced Domes*. Nichols Publishing Company, 1984. Chap. 7.

[31] K. Runesson, A. Samuelsson, and NE. Wiberg. *Byggnadsmekanik Knäckning*. Studentlitteratur, 1992.

[32] P-J. Gustafsson. *Balkteori - Course material*. Studentlitteratur, 2017.

[33] R. Crocetti. *Frames*. Design of Steel and Timber Structures. 2016.

[34] S. Krenk. *Non-linear modeling and analysis of solids and structures*. Cambridge University Press, 2009.

[35] J. Singer, J. Arbocz, and T. Weller. "Buckling experiments". In: *Experimental methods in buckling of thin-walled structure. Shells built-up structures* 2 (2002).

[36] K. Persson. *Nonlinear geometry*. n.d. URL: `http://www.byggmek.lth.se/fileadmin/byggnadsmekanik/education/courses/optional/VSMN30/Buckling.pdf/` (visited on 03/06/2017).

[37] Dassault Systèmes. *Abaqus Theory Manual (6.12) - Eigenvalue extraction*. 2012. URL: `https://things.maths.cam.ac.uk/computing/software/abaqus_docs/docs/v6.12/books/stm/default.htm?startat=ch02s05ath24.html` (visited on 03/09/2017).

[38] V. Gioncu. "Buckling of reticulated shells: state-of-the-art". In: *International Journal of Space Structures* 10.1 (1995), pp. 1–46.

[39] Dassault Systèmes. *Abaqus Theory Manual (6.12) - Modified Riks algorithm*. 2012. URL: `https://things.maths.cam.ac.uk/computing/software/abaqus_docs/docs/v6.12/books/stm/default.htm?startat=ch02s03ath18.html` (visited on 03/09/2017).

[40] A. Ivan and M. Ivan. "Typical failure modes of some single layered reticulated shells". In: *International Colloquium-Recent advances and new trends in structural design, Editura Orizonturi Universitare, Timisoara, Romania*. 2004, pp. 145–154.

[41] K. Gidófalvy and L. Katula. "Imperfection for the Buckling Analysis of Grid Shells". In: *Second Conference of Junior Researchers in Civil Engineering* (2013), pp. 74–80.

[42] T. Bulenda and J. Knippers. "Stability of grid shells". In: *Computers & Structures* 79.12 (2001), pp. 1161–1174.

[43] T. Chen. "On Introducing Imperfection in the Non-Linear Analysis of Buckling of Thin Shell Structures". In: *Coordinates* 51 (2014), pp. 4–375754.

[44] F. Fan et al. "Stability of reticulated shells considering member buckling". In: *Journal of Constructional Steel Research* 77 (2012), pp. 32–42.

[45] E. Lindgaard et al. "Nonlinear buckling optimization of composite structures considering "worst" shape imperfections". In: *International Journal of Solids and Structures* 47.22 (2010), pp. 3186–3202.

[46] J.M. Guo. "Research on distribution and magnitude of initial geometrical imperfection affecting stability of suspen-dome". In: *Adv. Steel Constr* 7.4 (2011), pp. 344–358.

[47] H.Z. Zhou et al. "Buckling of reticulated laminated veneer lumber shells in consideration of the creep". In: *Engineering Structures* 32.9 (2010), pp. 2912–2918.

[48] F. Fan et al. "Elasto-plastic stability of single-layer reticulated shells". In: *Thin-Walled Structures* 48.10 (2010), pp. 827–836.

[49] D.L. Richter. "Developments in Temcor aluminium domes". In: *Analysis, Design, and Construction of Braced Domes*. Nichols Publishing Company, 1984. Chap. 18.

[50] T. Suzuki et al. "Elastic buckling analysis of rigidly jointed single layer reticulated domes with random initial imperfection". In: *International Journal of Space Structures* 7.4 (1992), pp. 265–273.

[51] F. Fan et al. "Elasto-plastic stability of single-layer reticulated domes with initial curvature of members". In: *Thin-Walled Structures* 60 (2012), pp. 239–246.

[52] X. Chen et al. "Complete load-deflection response and initial imperfection analysis of single-layer lattice dome". In: *International Journal of Space Structures* 8.4 (1993), pp. 271–278.

[53] S. Kato et al. "Collapse of semi-rigidly jointed reticulated domes with initial geometric imperfections". In: *Journal of Constructional Steel Research* 48.2 (1998), pp. 145–168.

[54] I. M. Kani and R. E. McConnel. "Collapse of shallow lattice domes". In: *Journal of Structural Engineering* 113.8 (1987), pp. 1806–1819.

[55] S.Z. Shen. "Design formulas for stability analysis of reticulated shells". In: (1999).

[56] G. Yan, Q. Duan, and X. Hua. "Instability signature for detecting snap-through buckling of dome structures". In: *Sensors and Smart Structures Technologies for Civil, Mechanical, and Aerospace Systems 2016*. Vol. 9803. Apr. 2016, p. 98033X. DOI: 10.1117/12.2219389.

[57] C. Cui et al. "Node shift method for stiffness-based optimization of single-layer reticulated shells". In: *Journal of Zhejiang University SCIENCE A* 15.2 (2014), pp. 97–107.

[58] K. Abedi and GAR. Parke. "Progressive collapse of single-layer braced domes". In: *International Journal of Space Structures* 11.3 (1996), pp. 291–306.

[59] I. M. Kani and R. E. Mcconnel. "Single layer shallow lattice domes: analysis, general behaviour and collapse". In: *International Journal of Space Structures* 3.2 (1988), pp. 64–73.

[60] S.M. Holzer et al. "Finite Element Stability Analysis of a Glulam Dome". In: *International Journal of Space Structures* 7.4 (1992), pp. 353–361.

[61] R. Crocetti. *Arches*. Lecture in course Design of Bridges and Advanced Structures. 2016.

[62] VB Helper. *Tutorial: Drawing Platonic Solids - 6. Icosahedron*.

[63] D. Bertels. *Proportions in a Geodesic Dome - Calculations of the geodesic dome based on the icosahedron (frequency 3)*. 2004. URL: www.dirkbertels.net/computing/pentaDome_files/pentaDome_070206.pdf (visited on 02/20/2017).

[64] Dassault Systèmes. *Abaqus 6.10 Online Documentation - 26.3.8 Beam element library*. 2010. URL: http://abaqusdoc.ucalgary.ca/books/usb/default.htm?startat=pt06ch26s03ael14.html (visited on 04/05/2017).

[65] R. Crocetti. *Förband som klarar stora laster*. 2017. URL: https://www.svenskttra.se/tidningen-tra/2016-4/kunskap/ (visited on 05/18/2017).

[66] Swedish Standards Institute. *SS-EN 1991-1-4 Eurocode 1: Actions on structures - Part 1-4: General actions - Wind actions*. Swedish Standards Institute, 2005.

[67] P. E. Austrell et al. *CALFEM - A Finite Element Toolbox*. Vol. 3.4. Studentlitteratur, 2004.

[68] Dassault Systèmes. *Abaqus 6.12 - Keyword Reference Manual*. 2012. URL: https://things.maths.cam.ac.uk/computing/software/abaqus_docs/docs/v6.12/pdf_books/KEYWORD.pdf (visited on 04/10/2017).

Appendix A

Verification of Abaqus

A.1 Column and arch

Geometry & material

A linear buckling analysis was performed on a 5 m tall simply supported column in compression and an arch with uniformly distributed load over a span of 20 m and rise of 6 m. The material was set to isotropic with $E = 13$ GPa and $v = 0$. The column had a quadratic section with side 0.2 m while the arch had $bxh = 0.2x0.5$ m^2.

Abaqus simulation

Both cases were modeled as a wire of beam elements in 2D-space, i.e. type B21. The number of nodes were varied as a parametric study to check its convergence.

linear perturbation -> buckle were chosen in *step*-module, with Lanczos algorithm. The eigenvalue produced as a result corresponds to the buckling load, given in N for the column, and in N/m for the arch.

Hand calculations

The buckling load for the simply supported column corresponds to one of Euler's buckling load cases where the critical length is the same as the original, i.e. $\beta = 1$. The buckling load is calculated in eq. (A.1).

$$P_{cr} = \frac{\pi^2 EI}{(\beta l)^2} = \frac{\pi^2 \cdot 130 \cdot 10^9 \cdot 0.2^4}{5^2 \cdot 12} = 684.3 \text{ kN} \tag{A.1}$$

The linear buckling load for a uniformly compressed circular arch is determined by eq. (A.2) by Timoshenko[29], where l in this case corresponds to the span of 20 m. The factor γ_2 is governed by the rise/span and hinge configuration, which in this case is a two-hinged arch. According to Timoshenko[29] $\gamma_2 = 40.9$.

$$q_{cr} = \gamma_2 \frac{EI}{l^3} = 40.9 \cdot \frac{13e9 \cdot 0.2 \cdot 0.5^3}{20^3 \cdot 12} = 138.5\text{kN/m} \tag{A.2}$$

Conclusion

A mesh study was performed to verify the program's concordance with Euler buckling and Timoshenko's buckling equation for circular arches subjected to uniform compression.

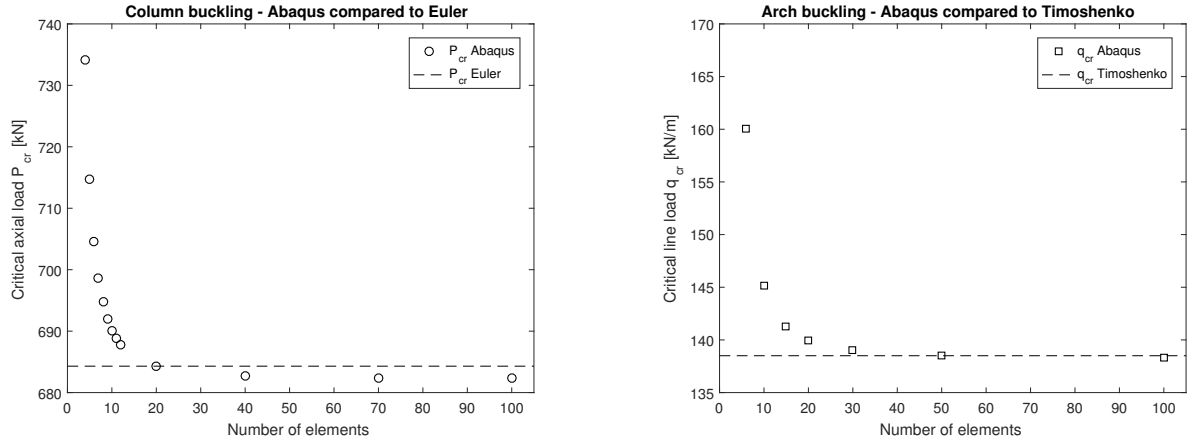

(a) Critical load vs number of elements **(b)** Critical load vs number of elements

Figure A1: Critical loads for a column and an arch

The result of this is that the numerical solution in Abaqus is in need of several nodes along the arch or column in order to capture the theoretical values. At least 20 nodes for the column would be sufficient, while the arch should have 30 or closer to 40.

Appendix B

Appendix Results: Stability

B.1 Imperfections

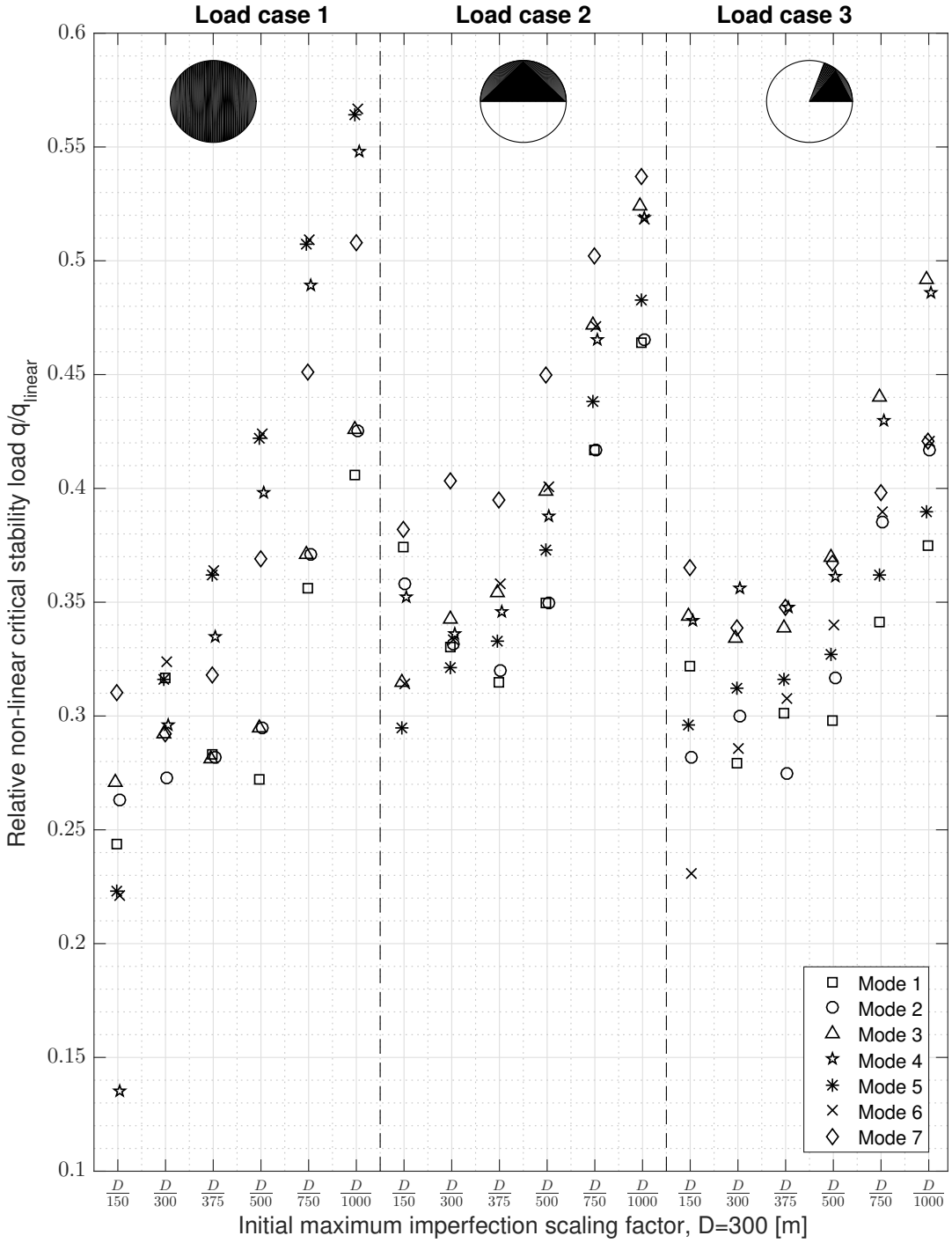

Figure A1: Imposed failure load when taking imperfections into account. Mode shapes 1-7 and initial imperfection D/300-D/1000

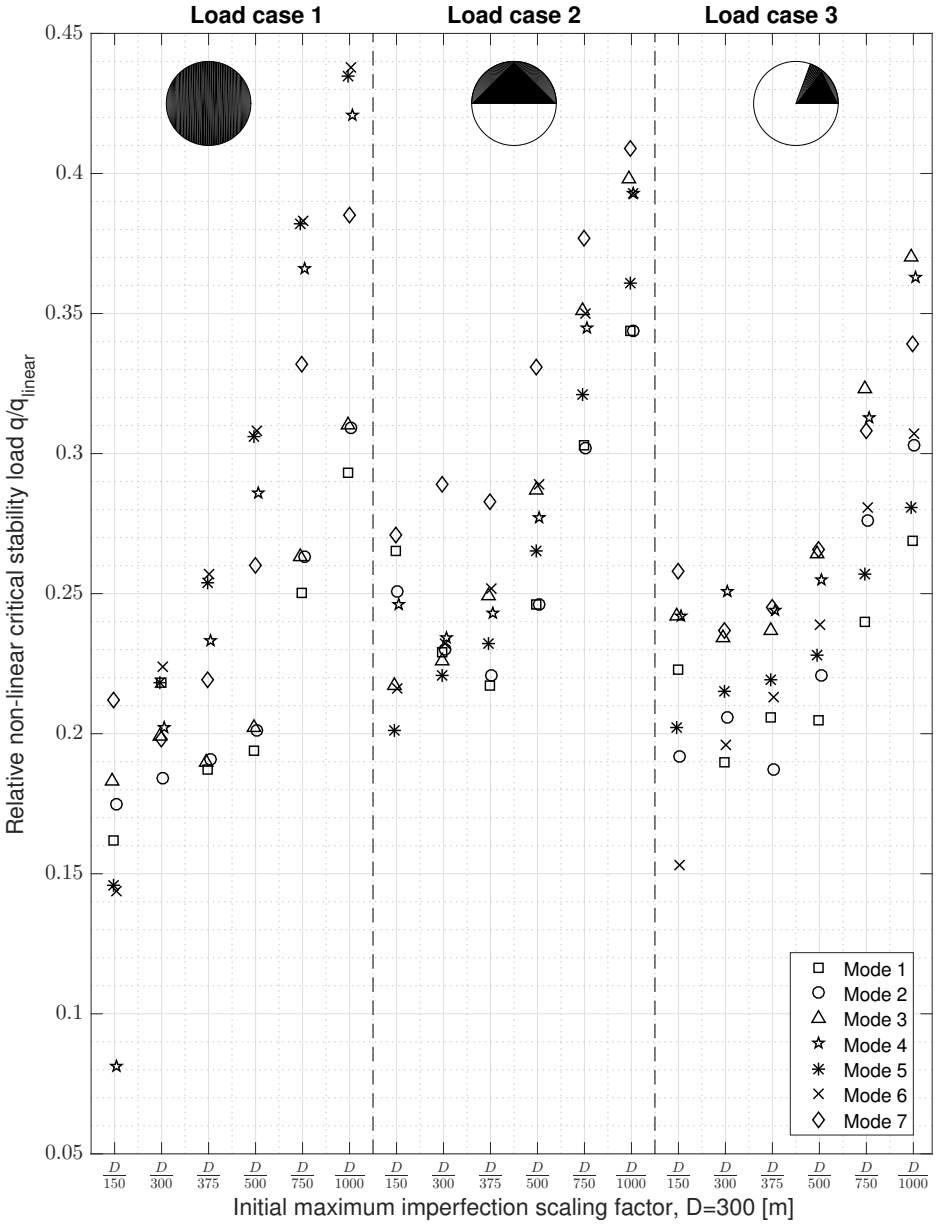

Figure A2: Imposed failure load when taking imperfections and creep into account by reducing the Young's modulus to 7 GPa for permanent loads. Mode shapes 1-7 and initial imperfection D/300-D/1000 for load cases 1-3

B.2 Load-deflection curve

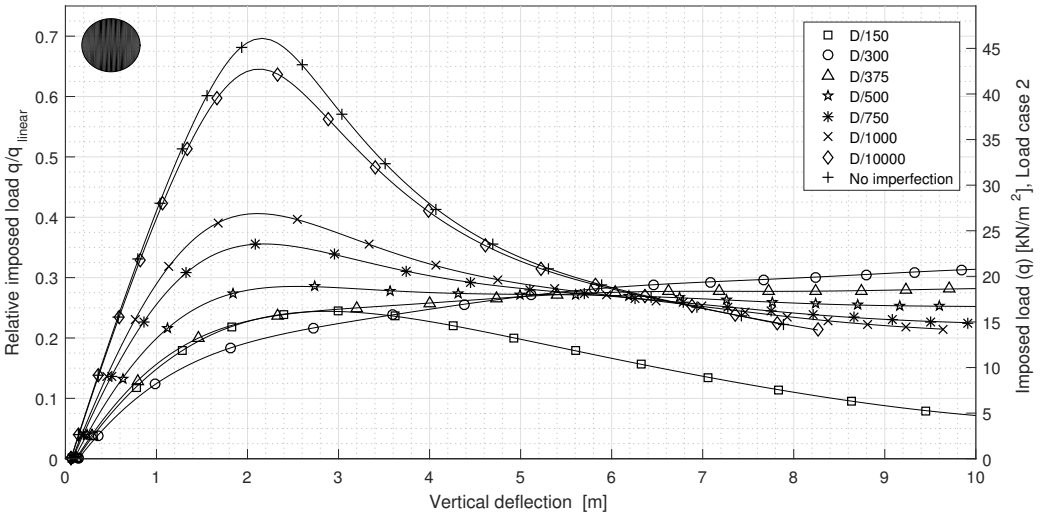

Figure A3: Load deflection curves for mode shape 1, fig. 8.5a, in load case 1. Initial imperfection D/150 to no imperfection

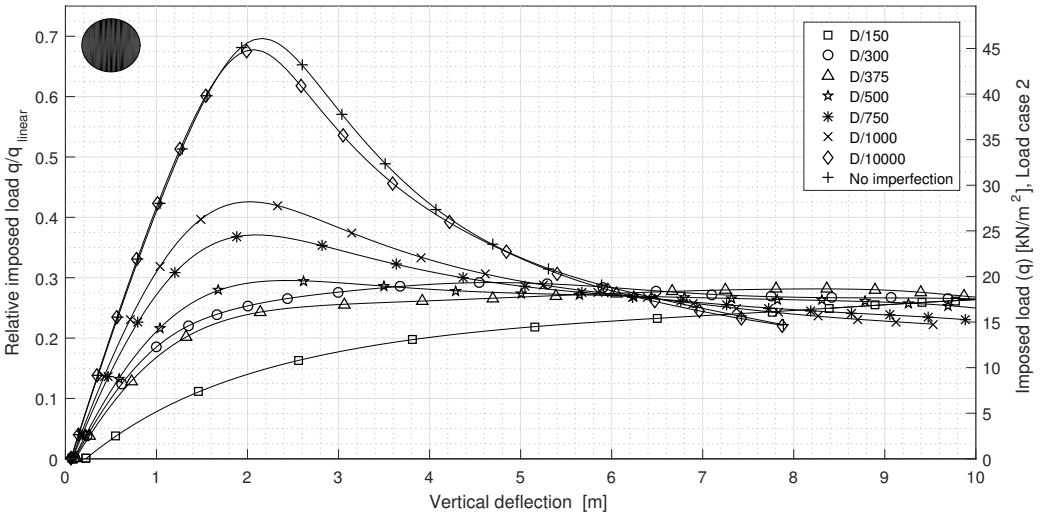

Figure A4: Load deflection curves for mode shape 3, fig. 8.5g, in load case 1. Initial imperfection D/150 to no imperfection

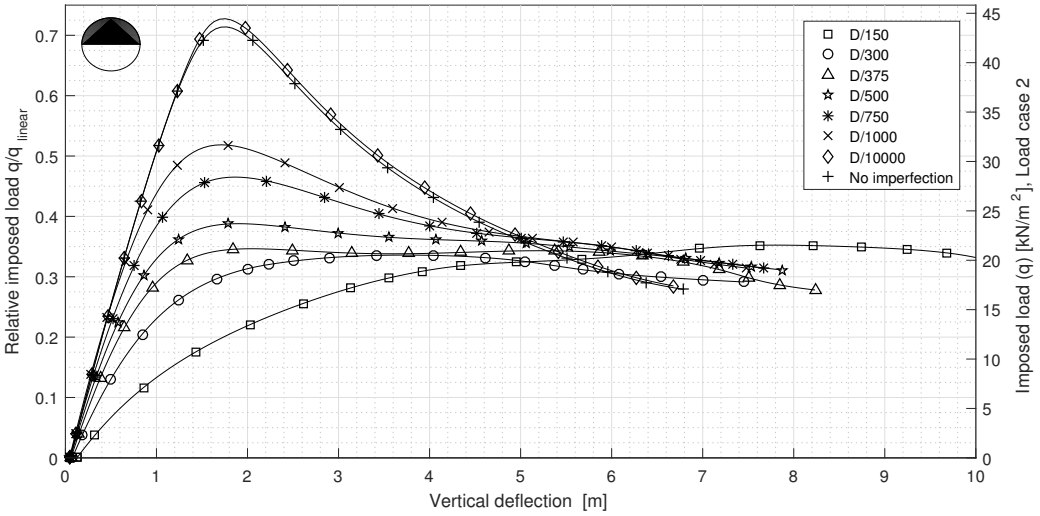

Figure A5: Load deflection curves for mode shape 4, fig. 8.6b, in load case 2. Initial imperfection D/150 to no imperfection

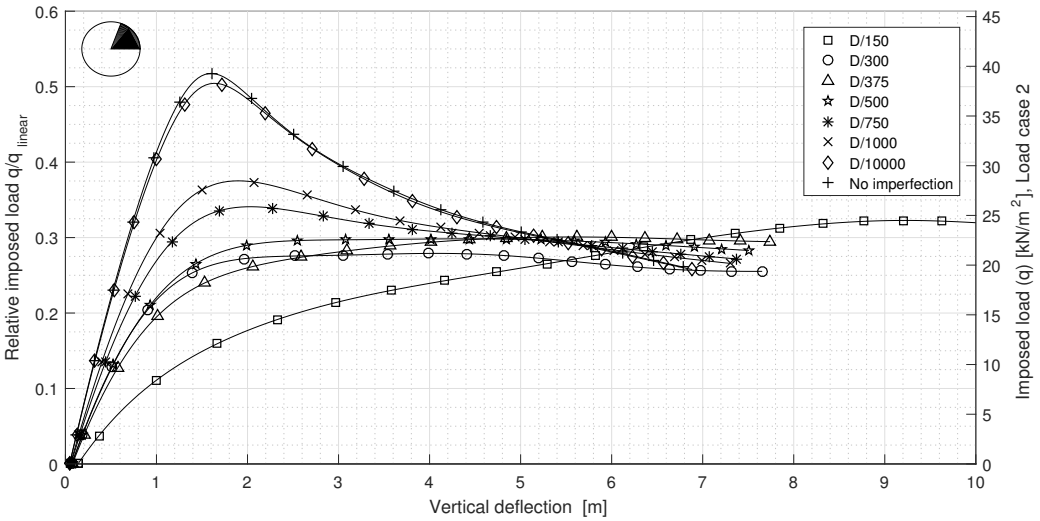

Figure A6: Load deflection curves for mode shape 1, fig. 8.5c, in load case 3. Initial imperfection D/150 to no imperfection

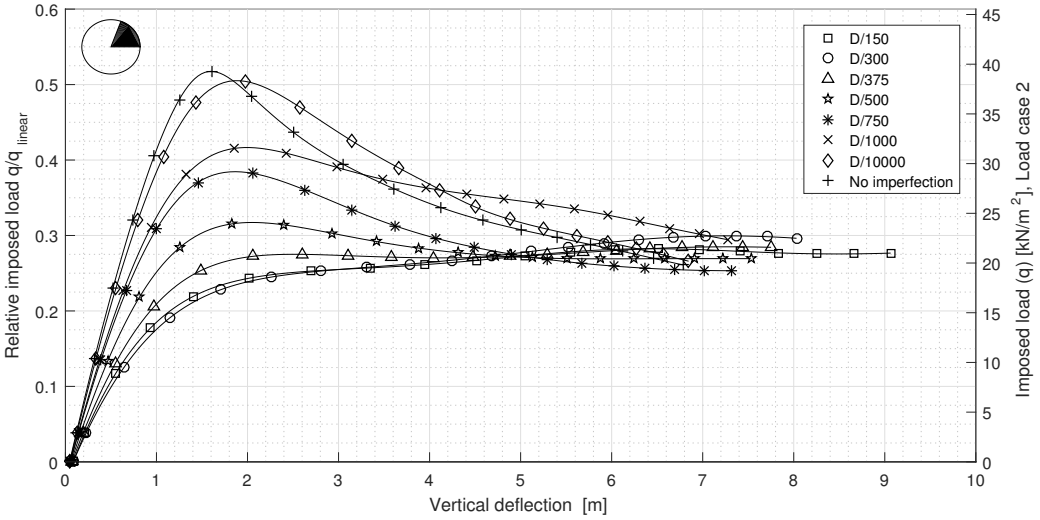

Figure A7: Load deflection curves for mode shape 2, fig. 8.5f, in load case 3. Initial imperfection D/150 to no imperfection

B.3 Creep and imperfection

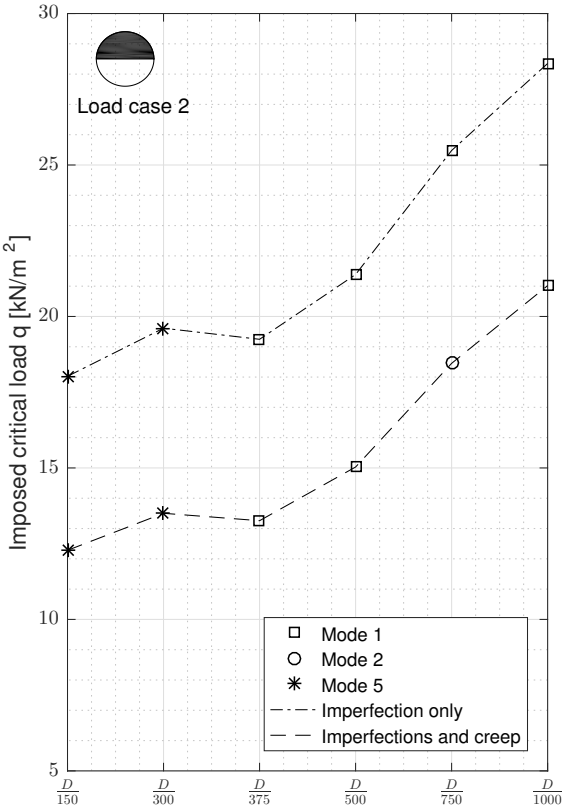

(a) Least remaining capacity in Load case 2, imperfections and imperfection and creep respectively, extracted from fig. 8.7 and fig. 8.13

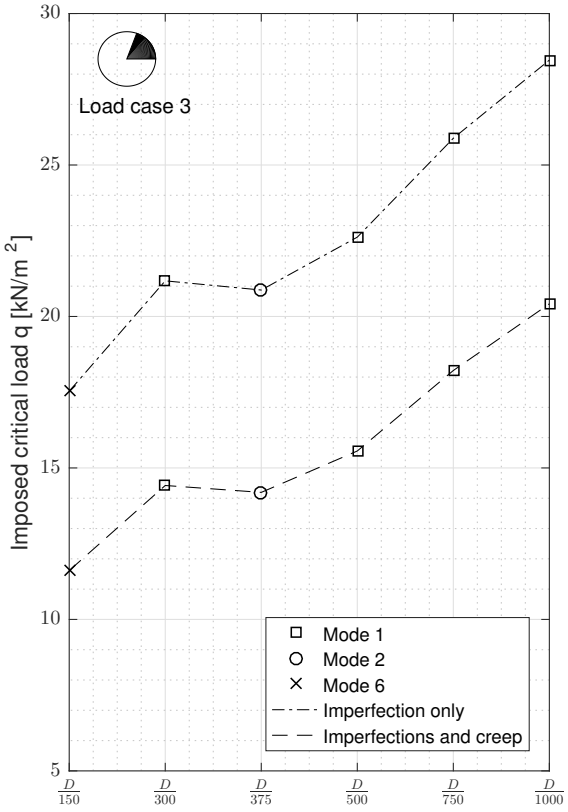

(b) Least remaining capacity in Load case 3, imperfections vs imperfection and creep respectively, extracted from fig. 8.7 and fig. 8.13

Figure A8: Least remaining capacity in Load case 1 and 2, imperfections and imperfection and creep respectively

Appendix C

Matlab Code

C.1 General scripts

C.1.1 Generating beam elements

C.1.2 Linear buckling

```
function makeinput_linearbuckling(filnamn,All_Nodes,Main_Nodes,
Topology_Matrix,Topology_Matrix_All_El,density,
h,b,section_A,I_11,I_22,J,loaded_members,redfac,boundary,div,
description,length_quota)

if (exist([filnamn,'.inp']))
    delete([filnamn,'.inp']);
end
diary([filnamn,'.inp'])

disp('*HEADING');
disp(description);
disp('SI units (kg, m, s, N)')
disp('1-axis horizontal, 2-axis vertical')
disp('*PREPRINT, ECHO=YES, MODEL=YES, HISTORY=YES')
disp('**')
disp('** Model definition')
disp('**')

Dofload=1:length(Main_Nodes);
Dofload(boundary)=[];
for i=Dofload
    disp(['*NODE, NSET=Mainnode-',num2str(i)])
    node=[sprintf('%d',i),', ',sprintf('%1.6f',(All_Nodes(i,1))),
        ', ',sprintf('%1.6f',(All_Nodes(i,3))),', ',sprintf('%1.6f',
    (All_Nodes(i,2)))];
    disp(node)
end
```

```
disp('**')
for i=boundary
    disp(['*NODE, NSET=Base-',num2str(i)])
    node=[sprintf('%d',i),', ',sprintf('%1.6f',(All_Nodes(i,1))),
        ', ',sprintf('%1.6f',(All_Nodes(i,3))),', ',sprintf('%1.6f',
    (All_Nodes(i,2)))];
    disp(node)
end

start_i=length(Main_Nodes);
for i=1:length(Topology_Matrix)
    disp('**')
    disp(['*NODE, NSET=Node-set-',num2str(i)])
    for j=1:div-1
        node=[sprintf('%d',start_i+j),', ',
            sprintf('%1.6f',(All_Nodes(start_i+j,1))),', ',
            sprintf('%1.6f',(All_Nodes(start_i+j,3))),', ',
            sprintf('%1.6f',(All_Nodes(start_i+j,2)))];
        disp(node)
    end
    start_i=start_i+j;
end
disp('*ELEMENT, TYPE=B31, ELSET=FRAME')
for i=1:length(Topology_Matrix_All_El)
   element=[sprintf('%d',Topology_Matrix_All_El(i,1)),
       ', ',sprintf('%d',(Topology_Matrix_All_El(i,2))),', ',
       sprintf('%d',(Topology_Matrix_All_El(i,3)))];
   disp(element)
end


% %------------------------------ GENERAL SECTION-----------------------
    for i=1:length(Topology_Matrix)
    disp(['*Elset, elset=Set-',num2str(i),', generate'])
    disp([num2str(div*(i-1)+1),', ',num2str(div*i),', 1'])
    disp('** Section: BEAMUS  Profile: GENERAL')
    disp(['*Beam General Section, elset=Set-',num2str(i),
        ', poisson=0.3, density=',num2str(density),', section=GENERAL'])
    disp([num2str(section_A),', ',num2str(I_22),', 0., ',num2str(I_11),', ',
        num2str(J)])
    n1=Main_Nodes(Topology_Matrix(i,2),:);
    n2=Main_Nodes(Topology_Matrix(i,3),:);
    nm=(n1+n2)*0.5;
    nm=[nm(1) nm(3) nm(2)];
    nm_norm=nm*1/norm(nm);
    disp([sprintf('%d',(nm_norm(1))),
        ', ',sprintf('%d',(nm_norm(2))),', ',sprintf('%d',(nm_norm(3)))]);
    disp('10.8e9, 4.212e9')
    end

disp('*MATERIAL, NAME=GLULAM')
disp('*DENSITY')
disp(num2str(density))
disp('*ELASTIC')
```

```
disp('10.8E9, 0.3')
disp('**')
disp('** History data')
disp('**')
disp('*BOUNDARY')
for i=1:length(boundary)
    bc=[sprintf('%d',boundary(i)),', ','ENCASTRE'];
    disp(bc)
end
disp('**')

for i=Dofload
    disp('**')
    disp(['*TRANSFORM,NSET=Mainnode-',num2str(i),',TYPE=S'])
    coord1=[0 0 0];
    coord2=Main_Nodes(i,:);
    print=[sprintf('%1.6f',coord1(1)),', ',sprintf('%1.6f',coord1(3)),
        ', ',sprintf('%1.6f',coord1(2)),', ',sprintf('%1.6f',coord2(1)),
        ', ',sprintf('%1.6f',coord2(3)),', ',sprintf('%1.6f',coord2(2))];
    disp(print)
    disp(['*BOUNDARY'])
    node=[sprintf('%d',i),', 4'];
    disp(node)
end

start_i=length(Main_Nodes)+1;
startind=length(Main_Nodes)+round(div/2);
j=startind:div-1:length(All_Nodes);
for i=1:length(Topology_Matrix)
    disp(['*TRANSFORM,NSET=Node-set-',num2str(i),',TYPE=S'])
    coord1=[0 0 0];
    coord2=All_Nodes(Topology_Matrix_All_El(j(i),2),:);
    print=[sprintf('%1.6f',coord1(1)),', ',sprintf('%1.6f',coord1(3)),
        ', ',sprintf('%1.6f',coord1(2)),', ',sprintf('%1.6f',coord2(1)),
        ', ',sprintf('%1.6f',coord2(3)),', ',sprintf('%1.6f',coord2(2))];
    disp(print)
    disp(['*BOUNDARY'])
    for k = start_i+1:4:start_i+div-2
        node=[sprintf('%d',k),', 4'];
        disp(node)
    end
    start_i=start_i+div-1;
end
disp('**')
disp('** STEP: Static self weight')
disp('** ')
disp('*Step, name="Static self weight", nlgeom=NO')
disp('*Static')
disp('1., 1., 1e-05, 1.')
disp('** ')
disp('** LOADS')
disp('** ')
disp('** Name: self weight   Type: Gravity')
disp('*Dload')
```

```
disp(', GRAV, 9.81, 0., -1., 0.')
disp('** ')
disp('** OUTPUT REQUESTS')
disp('** ')
disp('*Restart, write, frequency=0')
disp('** ')
disp('** FIELD OUTPUT: F-Output-2')
disp('** ')
disp('*Output, field, variable=PRESELECT')
disp('** ')
disp('** HISTORY OUTPUT: H-Output-1')
disp('** ')
disp('*Output, history, variable=PRESELECT')
disp('*End Step')
disp('*STEP')
disp('Buckling analysis')
disp('*BUCKLE, EIGENSOLVER=LANCZOS')
disp('10,')


disp('*DLOAD')
for i=1:length(Topology_Matrix)
    if ismember(i,loaded_members)
        disp(['Set-',num2str(i),', PY, ',num2str(-1*length_quota(i))])
    else
        disp(['Set-',num2str(i),', PY, ',num2str(-1*redfac*length_quota(i))])
    end
end

disp('*******************')
disp('*Output, field, variable=all')
disp('*FILE FORMAT, ASCII')
disp('*NODE FILE')
disp('U')
disp('*END STEP')
diary off
%-------------------------------------------------------------------------------------------
```

C.1.3 Non-linear buckling

```
function makeinput_riks(filename,All_Nodes,Main_Nodes,Topology_Matrix,
Topology_Matrix_All_El,density,h,b,section_A,I_11,I_22,J,loaded_members,
redfac,boundary,div,description,eigenvalue,length_quota,
mode,scaling,jobname_linbuck)

if (exist([filename,'.inp']))
    delete([filename,'.inp']);
end

diary([filename,'.inp'])
```

```
disp('*HEADING');
disp(description);
disp('SI units (kg, m, s, N)')
disp('1-axis horizontal, 2-axis vertical')
disp('*PREPRINT, ECHO=YES, MODEL=YES, HISTORY=YES')
disp('**')
disp('** Model definition')
disp('**')
Dofload=1:length(Main_Nodes);
Dofload(boundary)=[];
for i=Dofload
    disp(['*NODE, NSET=Mainnode-',num2str(i)])
    node=[sprintf('%d',i),', ',sprintf('%1.6f',(All_Nodes(i,1))),
        ', ',sprintf('%1.6f',(All_Nodes(i,3))),', ',
        sprintf('%1.6f',(All_Nodes(i,2)))];
    disp(node)
end
disp('**')
for i=boundary
    disp(['*NODE, NSET=Base-',num2str(i)])
    node=[sprintf('%d',i),', ',sprintf('%1.6f',(All_Nodes(i,1))),
        ', ',sprintf('%1.6f',(All_Nodes(i,3))),', ',
        sprintf('%1.6f',(All_Nodes(i,2)))];
    disp(node)
end


start_i=length(Main_Nodes);
for i=1:length(Topology_Matrix)
    disp('**')
    disp(['*NODE, NSET=Node-set-',num2str(i)])
    for j=1:div-1
        node=[sprintf('%d',start_i+j),', ',
            sprintf('%1.6f',(All_Nodes(start_i+j,1))),', ',
            sprintf('%1.6f',(All_Nodes(start_i+j,3))),', ',
            sprintf('%1.6f',(All_Nodes(start_i+j,2)))];
        disp(node)
    end
    start_i=start_i+j;
end

disp('*ELEMENT, TYPE=B31, ELSET=FRAME')
for i=1:length(Topology_Matrix_All_El)
   element=[sprintf('%d',Topology_Matrix_All_El(i,1)),', ',
       sprintf('%d',(Topology_Matrix_All_El(i,2))),', ',
       sprintf('%d',(Topology_Matrix_All_El(i,3)))];
   disp(element)
end


%------------------------------ GENERAL SECTION-------------------------
for i=1:length(Topology_Matrix)
    disp(['*Elset, elset=Set-',num2str(i),', generate'])
    disp([num2str(div*(i-1)+1),', ',num2str(div*i),', 1'])
```

```
    disp('** Section: BEAMUS  Profile: GENERAL')
    disp(['*Beam General Section, elset=Set-',num2str(i),
        ', poisson=0.3, density=',num2str(density),', section=GENERAL'])
    disp([num2str(section_A),', ',num2str(I_22),', 0., ',
        num2str(I_11),', ',num2str(J)])
    n1=Main_Nodes(Topology_Matrix(i,2),:);
    n2=Main_Nodes(Topology_Matrix(i,3),:);
    nm=(n1+n2)*0.5;
    nm=[nm(1) nm(3) nm(2)];
    nm_norm=nm*1/norm(nm);
    disp([sprintf('%d',(nm_norm(1))),', ',sprintf('%d',
    (nm_norm(2))),', ',sprintf('%d',(nm_norm(3)))]);
    disp('10.8e9, 4.212e9')
end
%-------------------------------------------------------------------------------

disp('**')
disp('** History data')
disp('**')
disp('*BOUNDARY')
for i=1:length(boundary)
    bc=[sprintf('%d',boundary(i)),', ','ENCASTRE'];
    disp(bc)
end
disp('**')

for i=Dofload
disp('**')
disp(['*TRANSFORM,NSET=Mainnode-',num2str(i),',TYPE=S'])
coord1=[0 0 0];
coord2=Main_Nodes(i,:);
print=[sprintf('%1.6f',coord1(1)),', ',sprintf('%1.6f',coord1(3)),
    ', ',sprintf('%1.6f',coord1(2)),', ',sprintf('%1.6f',coord2(1)),
    ', ',sprintf('%1.6f',coord2(3)),', ',sprintf('%1.6f',coord2(2))];
disp(print)
disp(['*BOUNDARY'])
        node=[sprintf('%d',i),', 4'];
        disp(node)
end

start_i=length(Main_Nodes)+1;
startind=length(Main_Nodes)+round(div/2);
j=startind:div-1:length(All_Nodes);
for i=1:length(Topology_Matrix)
disp(['*TRANSFORM,NSET=Node-set-',num2str(i),',TYPE=S'])
coord1=[0 0 0];
coord2=All_Nodes(Topology_Matrix_All_El(j(i),2),:);
print=[sprintf('%1.6f',coord1(1)),', ',sprintf('%1.6f',coord1(3)),', ',
    sprintf('%1.6f',coord1(2)),', ',sprintf('%1.6f',coord2(1)),', ',
    sprintf('%1.6f',coord2(3)),', ',sprintf('%1.6f',coord2(2))];
disp(print)
disp(['*BOUNDARY'])
for k=start_i+1:4:start_i+div-2
    node=[sprintf('%d',k),', 4'];
```

```
    disp(node)
end
start_i=start_i+div-1;
end
disp(['*IMPERFECTION, FILE=',jobname_linbuck,', STEP=2'])
disp([sprintf('%d',mode),', ',sprintf('%1.2f',scaling)])
disp('** STEP: Static egentyngd')
disp('** ')
disp('*Step, name="Static egentyngd", NLGEOM=YES, INC=100')
disp('*Static')
disp('1.E-5, 1.0, 1.E-5, 0.1, 1.0')
disp('** ')
disp('** LOADS')
disp('** ')
disp('** Name: egentyngd   Type: Gravity')
disp('*Dload')
disp(', GRAV, 9.81, 0., -1., 0.')
disp('** ')
disp('** OUTPUT REQUESTS')
disp('** ')
disp('*Restart, write, frequency=0')
disp('** ')
disp('** FIELD OUTPUT: F-Output-2')
disp('** ')
disp('*Output, field, variable=all')
disp('** ')
disp('** HISTORY OUTPUT: H-Output-1')
disp('** ')
disp('*Output, history, variable=all')
disp('*End Step')
disp('*STEP, NAME="Variabel Riks", NLGEOM=YES, INC=200')
disp('*STATIC, RIKS')
disp('1.E-5, 1.0, 1.E-5, 0.01, 1.0')

disp('*DLOAD')
for i=1:length(Topology_Matrix)
    if ismember(i,loaded_members)
        disp(['Set-',num2str(i),', PY, ...
            ',num2str(-eigenvalue*length_quota(i))])
    else
        disp(['Set-',num2str(i),', PY, ...
            ',num2str(-eigenvalue*redfac*length_quota(i))])
    end
end
disp('** ')
disp('** OUTPUT REQUESTS')
disp('** ')
disp('** ')
disp('** FIELD OUTPUT: F-Output-2')
disp('** ')
disp('*Output, field, variable=all')
disp('*NODE PRINT')
disp('U,')
disp('RF,')
```

```
disp('*Output, field, variable=all')
disp('*EL PRINT')
disp('S,')
disp('SF,')
disp('SM,')
disp('** ')
disp('** HISTORY OUTPUT: H-Output-1')
disp('** ')
disp('*Output, history, variable=all')
disp('**********************************')
disp('** OUTPUT FOR ABAQUS QA PURPOSES')
disp('**********************************')
disp('*FILE FORMAT, ASCII')
disp('*EL FILE')
disp('S,')
disp('SF,')
disp('*NODE FILE')
disp('U, RF')
disp('*END STEP')

diary off
```

C.1.4 Non-linear creep buckling

```
function makeinput_riks_creep(filnamn,All_Nodes,Main_Nodes,Topology_Matrix,
Topology_Matrix_All_El,density,h,b,section_A,I_11,I_22,J,loaded_members,
redfac,boundary,div,description,eigenvalue,length_quota,sub,
jobname_linbuck,E,G,mode,scaling)

if (exist([filnamn,'.inp']))
    delete([filnamn,'.inp']);
end

diary([filnamn,'.inp'])

disp('*HEADING');
disp(description);
disp('SI units (kg, m, s, N)')
disp('1-axis horizontal, 2-axis vertical')
disp('*PREPRINT, ECHO=YES, MODEL=YES, HISTORY=YES')
disp('**')
disp('** Model definition')
disp('**')
Dofload=1:length(Main_Nodes);
Dofload(boundary)=[];
for i=Dofload
    disp(['*NODE, NSET=Mainnode-',num2str(i)])
    node=[sprintf('%d',i),', ',sprintf('%1.6f',(All_Nodes(i,1))),', ',
        sprintf('%1.6f',(All_Nodes(i,3))),', ',
        sprintf('%1.6f',(All_Nodes(i,2)))];
    disp(node)
```

```
end
disp('**')
for i=boundary
    disp(['*NODE, NSET=Base-',num2str(i)])
    node=[sprintf('%d',i),', ',sprintf('%1.6f',(All_Nodes(i,1))),', ',
        sprintf('%1.6f',(All_Nodes(i,3))),', ',
        sprintf('%1.6f',(All_Nodes(i,2)))];
    disp(node)
end

start_i=length(Main_Nodes);
for i=1:length(Topology_Matrix)
    disp('**')
    disp(['*NODE, NSET=Node-set-',num2str(i)])
    for j=1:div-1
        node=[sprintf('%d',start_i+j),', ',
            sprintf('%1.6f',(All_Nodes(start_i+j,1))),', ',
            sprintf('%1.6f',(All_Nodes(start_i+j,3))),', ',
            sprintf('%1.6f',(All_Nodes(start_i+j,2)))];
        disp(node)
    end
    start_i=start_i+j;
end

disp('*ELEMENT, TYPE=B31, ELSET=FRAME')
for i=1:length(Topology_Matrix_All_El)
   element=[sprintf('%d',Topology_Matrix_All_El(i,1)),', ',
       sprintf('%d',(Topology_Matrix_All_El(i,2))),', ',
       sprintf('%d',(Topology_Matrix_All_El(i,3)))];
   disp(element)
end


%------------------------------ GENERAL SECTION-------------------------
for i=1:length(Topology_Matrix)
    disp(['*Elset, elset=Set-',num2str(i),', generate'])
    disp([num2str(div*(i-1)+1),', ',num2str(div*i),', 1'])
    disp('** Section: BEAMUS  Profile: GENERAL')
    disp(['*Beam General Section, elset=Set-',num2str(i),
        ', poisson=0.3, density=',num2str(density),
        ', section=GENERAL, dependencies=1'])
    disp([num2str(section_A),', ',num2str(I_22),', 0., ',
        num2str(I_11),', ',num2str(J)])
    n1=Main_Nodes(Topology_Matrix(i,2),:);
    n2=Main_Nodes(Topology_Matrix(i,3),:);
    nm=(n1+n2)*0.5;
    nm=[nm(1) nm(3) nm(2)];
    nm_norm=nm*1/norm(nm);
    disp([sprintf('%d',(nm_norm(1))),', ',sprintf('%d',(nm_norm(2))),', ',
        sprintf('%d',(nm_norm(3)))]);
    disp([sprintf('%1.1f',(E)),', ',sprintf('%1.6f',(G)),', 0, 0, 1'])
    disp('10.8e9, 4.212e9, 0, 0, 2')
end
```

```
disp('**')
disp('** History data')
disp('**')
disp('*BOUNDARY')
for i=1:length(boundary)
    bc=[sprintf('%d',boundary(i)),', ','ENCASTRE'];
    disp(bc)
end
disp('**')

for i=Dofload
disp('**')
disp(['*TRANSFORM,NSET=Mainnode-',num2str(i),',TYPE=S'])
coord1=[0 0 0];
coord2=Main_Nodes(i,:);
print=[sprintf('%1.6f',coord1(1)),', ',sprintf('%1.6f',coord1(3)),', ',
    sprintf('%1.6f',coord1(2)),', ',sprintf('%1.6f',coord2(1)),', ',
    sprintf('%1.6f',coord2(3)),', ',sprintf('%1.6f',coord2(2))];
disp(print)
disp(['*BOUNDARY'])

        node=[sprintf('%d',i),', 4'];
        disp(node)
end

start_i=length(Main_Nodes)+1;
startind=length(Main_Nodes)+round(div/2);
j=startind:div-1:length(All_Nodes);
for i=1:length(Topology_Matrix)
disp(['*TRANSFORM,NSET=Node-set-',num2str(i),',TYPE=S'])
coord1=[0 0 0];
coord2=All_Nodes(Topology_Matrix_All_El(j(i),2),:);
print=[sprintf('%1.6f',coord1(1)),', ',sprintf('%1.6f',coord1(3)),
    ', ',sprintf('%1.6f',coord1(2)),', ',sprintf('%1.6f',coord2(1)),', ',
    sprintf('%1.6f',coord2(3)),', ',sprintf('%1.6f',coord2(2))];
disp(print)
disp(['*BOUNDARY'])
for k=start_i+1:4:start_i+div-2
    node=[sprintf('%d',k),', 4'];
    disp(node)
end
start_i=start_i+div-1;
end

disp('*Initial conditions, type=field, variable=1')
for i=Dofload
    disp(['Node-set-',num2str(i),', ','1'])
end
for i=boundary
    disp(['Base-',num2str(i),', ','1'])
end
for i=1:length(Topology_Matrix)
    disp(['Node-set-',num2str(i),', ','1'])
end
```

```
disp(['*IMPERFECTION, FILE=',jobname_linbuck,', STEP=2'])
disp([sprintf('%d',mode),', ',sprintf('%1.1f',scaling)])
disp('** STEP: Static egentyngd')
disp('**')
disp('*Step, name="Static egentyngd", NLGEOM=YES, INC=100')
disp('*Static')
disp('1.E-5, 1.0, 1.E-5, 0.1, 1.0')
disp('** ')
disp('** LOADS')
disp('** ')
disp('** Name: egentyngd   Type: Gravity')
disp('*Dload')
disp(', GRAV, 9.81, 0., -1., 0.')
disp('** ')
disp('** OUTPUT REQUESTS')
disp('** ')
disp('*Restart, write, frequency=0')
disp('** ')
disp('** FIELD OUTPUT: F-Output-2')
disp('** ')
disp('*Output, field, variable=all')
disp('** ')
disp('** HISTORY OUTPUT: H-Output-1')
disp('** ')
disp('*Output, history, variable=all')
disp('*End Step')
disp('*STEP, NAME="Variabel Riks", NLGEOM=YES, INC=150')
disp('*STATIC, RIKS')
disp('1.E-5, 1.0, 1.E-5, 0.05, 1.0')
disp('*Field,variable=1')
for i=Dofload
    disp(['Node-set-',num2str(i),', ','2'])
end
for i=boundary
    disp(['Base-',num2str(i),', ','2'])
end
for i=1:length(Topology_Matrix)
    disp(['Node-set-',num2str(i),', ','2'])
end
disp('*DLOAD')
for i=1:length(Topology_Matrix)
    if ismember(i,loaded_members)
        disp(['Set-',num2str(i),', PY, ...
            ',num2str(-eigenvalue*length_quota(i))])
    else
        disp(['Set-',num2str(i),', PY, ...
            ',num2str(-eigenvalue*redfac*length_quota(i))])
    end
end

disp('*NODE PRINT')
disp('U,')
disp('RF,')
disp('*EL PRINT')
```

```
disp('S,')
disp('SF,')
disp('SM,')
disp('**********************************')
disp('** OUTPUT FOR ABAQUS QA PURPOSES')
disp('**********************************')
disp('*EL FILE')
disp('S,')
disp('*NODE FILE')
disp('U, RF')
disp('*END STEP')

diary off
```

C.2 Kiewitt

C.2.1 Main code

```
close all
clear all
div=20;
radius=150;
%% Section controls
b = 0.8; % b=0.8;
h = 0.8; % h=0.8;
parts=2;
sectiontype=2;
[section_A,I_11,I_22,I_12,J]=makesection(b,h,sectiontype,parts);
%------------------------------
% type        s               r
%    1        5               8
%    2        6               7
%    3        10              6
%    4        10              7
%    5        8               6
%    6        8               8
%    7        8               9
%------------------------------
type=7;                % TYPE
loadcase = 1;          % LOADCASE
redfac=0;
[Sector_coordinates ,R, rings ,sectors]=KiewittNodes(type);


Dof=1:length(Sector_coordinates);
[Topology_Matrix, Main_Nodes, Dof_big, boundary, loaded_members]
=KiewittElements(type,loadcase,Sector_coordinates,Dof, R);

[Ex,Ey,Ez]=coordxtr(Topology_Matrix,Main_Nodes,Dof_big',2);
```

```
Dof=Dof_big;
oldDof=Dof;

[Ex,Ey,Ez]=coordxtr(Topology_Matrix(loaded_members,:),Main_Nodes,oldDof',2);


[Topology_Matrix_All_El,Dof,All_Nodes]=beamgen(Dof,Topology_Matrix,Main_Nodes,div);
[Ex,Ey,Ez]=coordxtr(Topology_Matrix_All_El,All_Nodes,Dof',2);

for i=1:length(Topology_Matrix)
    distance(i)=sqrt((Main_Nodes(Topology_Matrix(i,2),1)
    -Main_Nodes(Topology_Matrix(i,3),1))^2
    +(Main_Nodes(Topology_Matrix(i,2),2)
    -Main_Nodes(Topology_Matrix(i,3),2))^2
    +(Main_Nodes(Topology_Matrix(i,2),3)
    -Main_Nodes(Topology_Matrix(i,3),3))^2);

    distance_xy(i) = sqrt((Main_Nodes(Topology_Matrix(i,2),1)
    -Main_Nodes(Topology_Matrix(i,3),1))^2
    +(Main_Nodes(Topology_Matrix(i,2),2)
    -Main_Nodes(Topology_Matrix(i,3),2))^2);
end
% calculate the relation between the 2D and 3D lengths
length_quota = distance_xy./distance;

[density ,q_egt]=fakedense(distance,section_A,radius);
```

C.2.2 Kiewitt nodes

```
function [Coord_xyz, R, s, r]=KiewittNodes(type)

%% External parameters. Geometry
if type == 1
    s=5 ;
    r=8;
elseif type==2
    s=6;
    r=7;
elseif type==3
    s=10;
    r=6;
elseif type==4
    s=10;
    r=7;
elseif type==5
    s=8;
    r=6;
elseif type==6
    s=8;
    r=8;
elseif type==7
    s=8;
    r=9;
end

span=300;
ratio = 0.3;
h = span*ratio;
R = h/2 + span^2/(8*h);



% Calculate number of nodes on each ring and place inside a vector
% calculate the initial angle on each ring, in radians
for i=1:r
    nodes_per_ring(i) = i*s;
    alpha(i) = (360)/nodes_per_ring(i);
    radius(i) = span/2* i/r;
end


nodes_per_seg = 1:r-1;
radii=[radius']; ...
index=r+1;
for i=1:r-1
    for j=1:nodes_per_seg(i)
        radii(index+j-1) = radius(i+1);
    end
    index=j+index;
```

```
end
index=r+1;
angles = [zeros(r,1)];
for i=1:r-1
    for j=1:nodes_per_seg(i)
        angles(index+j-1) = alpha(i+1)*j;
    end
    index=j+index;
end
nn_seg = length(radii);


angles= angles';
% Coordinates
for m=1:length(angles)
    x(m) = radii(m)*cosd(angles(m));
    y(m) = radii(m)*sind(angles(m));
    z(m) = sqrt(R^2- x(m)^2-y(m)^2);
end
Coord_xyz = [x', y', z'];
Coord_dominus=[Coord_xyz];
for i=1:s-1
    theta= (i)*pi*2/s;
    for j=1:length(x)
          P=[Coord_xyz(j,1) Coord_xyz(j,2) Coord_xyz(j,3)];
          P = P*[cos(theta),sin(theta),0;-sin(theta),cos(theta),0;0,0,1];
          Coord_dome(j,:) = [P];
    end
    Coord_dominus=[Coord_dominus; Coord_dome];
end


Coord_dominus = [Coord_dominus; 0, 0, R];
```

C.3 Geodesic

```
%%%%%%%%%%%%%%% Welcome %%%%%%%%%%%%%%%
format long, close all, clear all, clc
%%%%%%%%%%%%%%%%%%%%%%%%%%%%%%%%%%%%%%%
%%%%%%% GEODESIC DOME GENERATOR %%%%%%
%%%%%% Requires CALFEM %%%%%%%%%%%%%%%
% http://www.solid.lth.se/fileadmin/hallfasthetslara/..
% ...utbildning/kurser/FHL064_FEM/calfem34.pdf
%%%%%%%%%%%%%%%%%%%%%%%%%%%%%%%%%%%%%%%

%%%%%%%%%%%%%% Controls %%%%%%%%%%%%%%%
sub = 11; % Number of divisons (8, 9, 10 or 11)
radius_dome = 150; % Radius of the dome

%  1 = UDL over entire dome
%  2 = 1*UDL over half dome. 0.5*UDL over second half
%  3 = UDL on 1 sector of 70 degrees.
loadcase = 1; % 1-3
% Asym load reduction factor
redfac = 0;
% Number of B31 Elements per beam
div = 20;

%% Section controls
b = 0.8; % b=0.8;
h = 0.8; % h=0.8;
parts=2;
sectiontype=2;
h_tot= 2.*(h+move_vertically);


%% Geometrical parameters
% phi = (1+ sqrt(5))/2;
S=2;
t1 = 2 * pi / 5 ;
t2 = pi / 10;
t4 = pi / 5 ;
t3 = -3 * pi / 10;
R  = (S/2) / sin(t4);
Ha  = cos(t4) * R;
Cx = R * cos(t2);
Cy = R * sin(t2);
H1 = sqrt(S * S - R * R);
H2 = sqrt((Ha + R) * (Ha + R) - Ha * Ha);
Z2 = (H2 - H1) / 2;
Z1 = Z2 + H1;

A =    [0,   0,  Z1];
B =   [ 0,   R,  Z2];
C =  [ Cx,  Cy,  Z2];
```

```
D = [ S/2,  -Ha,  Z2];
E =[ -S/2,  -Ha,  Z2];
F = [ -Cx,  Cy,  Z2];
G =[    0,  -R, -Z2];
H =  [-Cx, -Cy, -Z2];
I = [-S/2,   Ha, -Z2];
J =[  S/2,   Ha, -Z2];
K =[   Cx, -Cy, -Z2];
L =[    0,   0, -Z1];


triangles = [A D C;
             A C B;
             A B F;
             A F E;
             A E D];

%The varaiable Main_nodes denote the points where the beams are connected
Main_Nodes=[];
ex_supportus=[];
[len_tri,~]=size(triangles);

for i=1:len_tri
    [V, radius_icosahedron, ex_support]=makevertex(triangles(i,:),sub);
    Main_Nodes=[Main_Nodes; V];
    ex_supportus=[ex_supportus; ex_support];
end
Main_Nodes=[0 0 1; Main_Nodes; ex_supportus];
Main_Nodes=Main_Nodes./radius_icosahedron*radius_dome;


Dof=1:length(Main_Nodes);
[Topology_Matrix boundary loaded_members ...
   ]=geodesic_elements(sub,loadcase,Main_Nodes,Dof);

oldDof=Dof;
%Generating the 20 B31 intermediate elements on every beam, controlled by
%div
[Topology_Matrix_All_El,Dof,All_Nodes]=beamgen(Dof,Topology_Matrix,Main_Nodes,div);
[Ex,Ey,Ez]=coordxtr(Topology_Matrix_All_El,All_Nodes,Dof',2);
% Calcuate the distance in 3D and 2D
for i=1:length(Topology_Matrix)
    distance(i)=sqrt((Main_Nodes(Topology_Matrix(i,2),1)
    -Main_Nodes(Topology_Matrix(i,3),1))^2
    +(Main_Nodes(Topology_Matrix(i,2),2)-Main_Nodes(Topology_Matrix(i,3),2))^2
    +(Main_Nodes(Topology_Matrix(i,2),3)-Main_Nodes(Topology_Matrix(i,3),3))^2);

    distance_xy(i) = sqrt((Main_Nodes(Topology_Matrix(i,2),1)
    -Main_Nodes(Topology_Matrix(i,3),1))^2
    +(Main_Nodes(Topology_Matrix(i,2),2)-Main_Nodes(Topology_Matrix(i,3),2))^2);
end
% calculate the relation between the 2D and 3D lengths
length_quota = distance_xy./distance;
```

```
[section_A,I_11,I_22,I_12,J]=makesection(b,h,sectiontype,parts);
[density , q_egt]=fakedense(distance,section_A,radius_dome,sub);
```

C.4 Three-way grid

```
clc
clear all
close all
r = 150;   % Radius
w = 10;    % number of elements along from the apex to the base along a ...
   meridional
loadcase=2;
redfac=0;
div=20;
%------------------------------
% Section controls
%------------------------------
b = 0.8; % b=0.8;
h = 0.8; % h=0.8;
parts=2;
sectiontype=2;
h_tot= 2.*(h+move_vertically);
[section_A,I_11,I_22,I_12,J]=makesection(b,h,sectiontype,
move_vertically,move_sideways,parts);
%------------------------------


sectors = 6;
phi = 2*pi/6;
ratio = 0.3;
h=ratio*2*r;
R = h/2 + (2*r)^2/(8*h); % Radius of the sphere in the XY-plane

A = [r*cos(0) r*sin(0)];
B = [r*cos(phi) r*sin(phi)];
O = [0 0];
anglevec = (pi/33):(pi/33):pi/3;
for i=1:w
    angle = anglevec(i);
    S(i,:) = [r*cos(angle) r*sin(angle) (R-h)];
end


%Edge coordinates XY-plane
for v=1:w
    AO_e(v,:) = ( v*A+ (w-v)*O)/w;
    BO_e(v,:) = ( v*B+ (w-v)*O)/w;
    AB_e(v,:) = ( (w-v)*A+ v*B)/w;
end


%Intermediate nodes Name: O_level_A_B in a triangle
O_211 = (AO_e(2,:)+ BO_e(2,:))/2;  %level 2
```

```
O_321 = (2*AO_e(3,:)+ BO_e(3,:))/3;  %level 3
O_312 = (AO_e(3,:)+ 2*BO_e(3,:))/3;   %level 3

O_431 = (3*AO_e(4,:)+ 1*BO_e(4,:))/4;   %level 4
O_422 = (2*AO_e(4,:)+ 2*BO_e(4,:))/4;   %level 4
O_413 = (1*AO_e(4,:)+ 3*BO_e(4,:))/4;   %level 4

O_541 = (4*AO_e(5,:)+ 1*BO_e(5,:))/5;   %level 5
O_532 = (3*AO_e(5,:)+ 2*BO_e(5,:))/5;   %level 5
O_523 = (2*AO_e(5,:)+ 3*BO_e(5,:))/5;   %level 5
O_514 = (1*AO_e(5,:)+ 4*BO_e(5,:))/5;   %level 5

O_651 = (5*AO_e(6,:)+ 1*BO_e(6,:))/6;   %level 6
O_642 = (4*AO_e(6,:)+ 2*BO_e(6,:))/6;   %level 6
O_633 = (3*AO_e(6,:)+ 3*BO_e(6,:))/6;   %level 6
O_624 = (2*AO_e(6,:)+ 4*BO_e(6,:))/6;   %level 6
O_615 = (1*AO_e(6,:)+ 5*BO_e(6,:))/6;   %level 6

O_761 = (6*AO_e(7,:)+ 1*BO_e(7,:))/7;   %level 7
O_752 = (5*AO_e(7,:)+ 2*BO_e(7,:))/7;   %level 7
O_743 = (4*AO_e(7,:)+ 3*BO_e(7,:))/7;   %level 7
O_734 = (3*AO_e(7,:)+ 4*BO_e(7,:))/7;   %level 7
O_725 = (2*AO_e(7,:)+ 5*BO_e(7,:))/7;   %level 7
O_716 = (1*AO_e(7,:)+ 6*BO_e(7,:))/7;   %level 7

O_871 = (7*AO_e(8,:)+ 1*BO_e(8,:))/8;   %level 8
O_862 = (6*AO_e(8,:)+ 2*BO_e(8,:))/8;   %level 8
O_853 = (5*AO_e(8,:)+ 3*BO_e(8,:))/8;   %level 8
O_844 = (4*AO_e(8,:)+ 4*BO_e(8,:))/8;   %level 8
O_835 = (3*AO_e(8,:)+ 5*BO_e(8,:))/8;   %level 8
O_826 = (2*AO_e(8,:)+ 6*BO_e(8,:))/8;   %level 8
O_817 = (1*AO_e(8,:)+ 7*BO_e(8,:))/8;   %level 8

O_981 = (8*AO_e(8,:)+ 1*BO_e(8,:))/8;   %level 8
O_972 = (7*AO_e(8,:)+ 2*BO_e(8,:))/8;   %level 8
O_963 = (6*AO_e(8,:)+ 3*BO_e(8,:))/8;   %level 8
O_954 = (5*AO_e(8,:)+ 4*BO_e(8,:))/8;   %level 8
O_945 = (4*AO_e(8,:)+ 5*BO_e(8,:))/8;   %level 8
O_936 = (3*AO_e(8,:)+ 6*BO_e(8,:))/8;   %level 8
O_927 = (2*AO_e(8,:)+ 7*BO_e(8,:))/8;   %level 8
O_918 = (1*AO_e(8,:)+ 8*BO_e(8,:))/8;   %level 8

% Collect all the XY-nodes into one matrix
Coord_Sector_xy = [O; AO_e;  AB_e; O_211; O_321; O_312; O_431; O_422; ...
    O_413;...
   O_541; O_532; O_523; O_514; O_651; O_642; O_633; O_624; O_615;
   O_761; O_752; O_743; O_734; O_725; O_716;
   O_871;  O_862; O_853; O_844; O_835; O_826; O_817;
   O_981; O_972; O_963; O_954; O_945; O_936; O_927; O_918
   ];


 for i=1:length(Coord_Sector_xy)
    z_coord(i) = sqrt(R^2 - Coord_Sector_xy(i,1)^2- Coord_Sector_xy(i,2)^2);
```

```
    Coord_Sector_xyz(i,:) = [Coord_Sector_xy(i,:) z_coord(i)];
 end
 Coord_Sector_xyz= [Coord_Sector_xyz; S];

Coord_Sector_xyz(length(O)+length(AO_e)+length(AB_e)-1,:)=[];
Coord_Sector_xyz(1,:)=[];
old_coord=Coord_Sector_xyz;
c_z = [Coord_Sector_xyz(:,3); Coord_Sector_xyz(:,3);
    Coord_Sector_xyz(:,3); Coord_Sector_xyz(:,3);...
    Coord_Sector_xyz(:,3); Coord_Sector_xyz(:,3)];


for i=1:length(El_tria)
    Topology_sector(i,:)=[i El_tria(i,:)];
end


lEdof=length(Topology_sector);

Topology_Matrix=[];
Main_Nodes=[Coord_Sector_xyz];

for i=1:5
    theta= (i)*pi/3;
    for j=1:length(Coord_Sector_xyz)
          P=[Coord_Sector_xyz(j,1) Coord_Sector_xyz(j,2) ...
             Coord_Sector_xyz(j,3)];
          P = P*[cos(theta),sin(theta),0;-sin(theta),cos(theta),0;0,0,1];
          Coord_dome(j,:) = [P];
    end
    Main_Nodes=[Main_Nodes; Coord_dome];
    Topology_Matrix=[Topology_Matrix; Topology_sector];

    Topology_sector(:,1)=Topology_sector(:,1)+lEdof;
    Topology_sector(:,2:end)=Topology_sector(:,2:end)+length(Coord_Sector_xyz);

end
Topology_Matrix=[Topology_Matrix; Topology_sector];

Main_Nodes=[Main_Nodes; 0 0 R];

len_El_fixus=length(El_fixus);
last_el = Topology_Matrix(end,1);
for sec=1:5
    j=0;
    Elements=Topology_Matrix(end,1)+1:Topology_Matrix(end,1)+len_El_fixus;
    for i=Elements
        j=j+1;
        Topology_Matrix(i,:) =[i El_fixus(j,:)];
    end
    El_fixus=El_fixus+length(Coord_Sector_xyz);
end

Dof=1:length(Main_Nodes);
```

```
j=0;
for i=Elements(end)+1:Elements(end)+length(El_sist)
    j=j+1;
    Topology_Matrix(i,:)=[i El_sist(j,:)];
end

Dof=1:length(Main_Nodes);

for i=1:length(Topology_Matrix)
    distance(i)=sqrt((Main_Nodes(Topology_Matrix(i,2),1)
    -Main_Nodes(Topology_Matrix(i,3),1))^2
    +(Main_Nodes(Topology_Matrix(i,2),2)
    -Main_Nodes(Topology_Matrix(i,3),2))^2
    +(Main_Nodes(Topology_Matrix(i,2),3)
    -Main_Nodes(Topology_Matrix(i,3),3))^2);

    distance_xy(i) = sqrt((Main_Nodes(Topology_Matrix(i,2),1)
    -Main_Nodes(Topology_Matrix(i,3),1))^2
    +(Main_Nodes(Topology_Matrix(i,2),2)
    -Main_Nodes(Topology_Matrix(i,3),2))^2);
end
length_quota = distance_xy./distance;
[density, q_egt]=fakedense_KW(distance,section_A,r);
oldDof=Dof;

[Topology_Matrix_All_El,Dof,All_Nodes]=beamgen(Dof,Topology_Matrix,Main_Nodes,div);
[Ex,Ey,Ez]=coordxtr(Topology_Matrix_All_El,All_Nodes,Dof',2);
```

Appendix D

Input files

The geometry, material, element and element type, and loads were all controlled by input files. The keywords used as well as a few sample input files are listed below. All the keywords can be found in the Abaqus Keyword Reference Manual[68].

Keyword[68] used in Abaqus - see appendix C for Matlab scripts and appendix D for sample input files

---

*ELEMENT, TYPE=B31, ELSET=FRAME

Keywords[68] used in Abaqus - see appendix C for Matlab scripts and appendix D for sample input files

---

*Elset, elset=Set-<*Set number*>, generate
<*First Element*>, <*Last Element*>, <*Element Increment*>
*Beam General Section, elset=Set-<*Set number*>, poisson=0.3,
density=<*density*>, section=GENERAL
<*Cross-sectional Area*>, <I_{11}>, <I_{12}>, <I_{22}>, <*Torsional constant J*>
<*First direction cosine of the first beam section axis*>,
<*Second direction cosine of the first beam section axis*>,
<*Third direction cosine of the first beam section axis*>

Keyword[68] used in Abaqus - see appendix C for Matlab scripts and appendix D for sample input files

---

*BOUNDARY
<*Node number*>, ENCASTRE

Keywords[68] used in Abaqus - see appendix C for Matlab scripts and appendix D for sample

input files

---

*TRANSFORM,NSET=Node-set-<*Set number*>, TYPE=S
Global X-coordinate of point a specifying transformation,
Global Y-coordinate of point a specifying transformation,
Global Z-coordinate of point a specifying transformation,
Global X-coordinate of point b specifying transformation,
Global Y-coordinate of point b specifying transformation,
Global Z-coordinate of point b specifying transformation
*BOUNDARY
<*Node number*>, <*4th degree of freedom*>

Keyword[68] used in Abaqus - see appendix C for Matlab scripts and appendix D for sample input files

---

*IMPERFECTION, FILE=',<*Jobname linear buckling*>, STEP=<*Step number*>
<*Mode number*>, <*Mode shape scaling factor*>

D.1 Linear buckling

```
*HEADING
Geodesic with sub11. h = 0.8. b = 0.8. Truss, Loadcase 2. I_11 = 0.27307
SI units kg, m, s, N
1-axis horizontal, 2-axis vertical
*PREPRINT, ECHO=YES, MODEL=YES, HISTORY=YES
**
** Model definition
**
*NODE, NSET=Mainnode-1
1, 0.000000, 167.705098, 0.000000
*NODE, NSET=Mainnode-2
2, 8.408599, 167.093839, -11.573444
*NODE, NSET=Mainnode-3
.......
366, 61.380875, 82.050085, -132.759827
*NODE, NSET=Mainnode-367
367, 75.677391, 78.680597, -127.307880
**

*NODE, NSET=Base-57
57, 88.167788, 75.000000, -121.352549
*NODE, NSET=Base-68
```

```
68, 107.900970, 75.000000, -104.198756
*NODE, NSET=Base-69
.....
385, -77.255711, 75.000000, -128.575095
*NODE, NSET=Base-386
386, 77.255711, 75.000000, -128.575095
**
*ELEMENT, TYPE=B31, ELSET=FRAME
1, 2, 387
2, 387, 388
.....
20699, 20050, 20051
20700, 20051, 386

*Elset, elset=Set-1, generate
1, 20, 1
** Section: BEAMUS  Profile: GENERAL
*Beam General Section, elset=Set-1, poisson=0.3, density=674.0886, section=GENERAL
1.28, 0.068267, 0., 0.27307, 0.11537
7.744053e-02, 9.912830e-01, -1.065877e-01
10.8e9, 4.212e9
....
*Elset, elset=Set-1035, generate
20681, 20700, 1
** Section: BEAMUS  Profile: GENERAL
*Beam General Section, elset=Set-1035, poisson=0.3, density=674.0886, section=GENERAL
1.28, 0.068267, 0., 0.27307, 0.11537
4.559942e-01, 4.582229e-01, -7.629555e-01
10.8e9, 4.212e9

**
** History data
**
*BOUNDARY
57, ENCASTRE
68, ENCASTRE
......
386, ENCASTRE
**
**

*TRANSFORM,NSET=Node-set-1,TYPE=S
0.000000, 0.000000, 0.000000, 49.968079, 152.259284, -48.844130
*BOUNDARY
388, 4
392, 4
396, 4
400, 4
404, 4

*TRANSFORM,NSET=Node-set-1035,TYPE=S
0.000000, 0.000000, 0.000000, -0.680270, 167.674535, 0.221033
*BOUNDARY
20034, 4
```

```
20038, 4
20042, 4
20046, 4
20050, 4
**
** STEP: Static self weight
**
*Step, name="Static self weight", nlgeom=NO
*Static
1., 1., 1e-05, 1.
**
** LOADS
**
** Name: self weight   Type: Gravity
*Dload
, GRAV, 9.81, 0., -1., 0.
**
** OUTPUT REQUESTS
**
*Restart, write, frequency=0
**
** FIELD OUTPUT: F-Output-2
**
*Output, field, variable=PRESELECT
**
** HISTORY OUTPUT: H-Output-1
**
*Output, history, variable=PRESELECT
*End Step
*STEP
Buckling analysis
*BUCKLE, EIGENSOLVER=LANCZOS
10,
*DLOAD
Set-1, PY, -0.99128
Set-2, PY, -0.99714
.......
********************
*Output, field, variable=all
*FILE FORMAT, ASCII
*NODE FILE
U
*END STEP
```

D.2 Non-linear buckling - Riks

The keywords: *NODE, *ELEMENT, *Elset, *BOUNDARY, *TRANSFORM have been removed since they were identical to the linear buckling input file in appendix D.1. The keyword *IMPERFECTION and the step *STATIC, RIKS have been added to the input

file.

```
.....

*IMPERFECTION, FILE=LinearBuckling, STEP=2
1, -1.0
** STEP: Static egentyngd
**
*Step, name="Static self weight", NLGEOM=YES, INC=100
*Static
1.E-5, 1.0, 1.E-5, 0.1, 1.0
**
** LOADS
**
** Name: egentyngd   Type: Gravity
*Dload
, GRAV, 9.81, 0., -1., 0.
**
** OUTPUT REQUESTS
**
*Restart, write, frequency=0
**
** FIELD OUTPUT: F-Output-2
**
*Output, field, variable=all
**
** HISTORY OUTPUT: H-Output-1
**
*Output, history, variable=all
*End Step
*STEP, NAME="Variabel Riks", NLGEOM=YES, INC=200
*STATIC, RIKS
1.E-5, 1.0, 1.E-5, 0.01, 1.0
*DLOAD
Set-1, PY, -266387.4846
Set-2, PY, -267961.3362
....
**
** OUTPUT REQUESTS
**

...

*END STEP
```

D.3 Non-linear creep buckling - Riks

```
.....
*Elset, elset=Set-1, generate
```

```
1, 20, 1
** Section: BEAMUS  Profile: GENERAL
*Beam General Section, elset=Set-1, poisson=0.3, density=674.0886, section=GENERAL, dependencies=1
1.28, 0.068267, 0., 0.27307, 0.11537
7.744053e-02, 9.912830e-01, -1.065877e-01
7000000000.0, 2692307692.307692, 0, 0, 1
10.8e9, 4.212e9, 0, 0, 2


** Use the reduced Young's Modulus E= 7 GPa
*Initial conditions, type=field, variable=1
Node-set-1, 1
Node-set-2, 1
Node-set-3, 1
....
Node-set-1034, 1
Node-set-1035, 1
**Imperfection using mode shape 4, factor -0.6 => D/500
*IMPERFECTION, FILE=LinearBuckling, STEP=2
4, -0.6
** STEP: Static egentyngd
**
*Step, name="Static egentyngd", NLGEOM=YES, INC=100
*Static
1.E-5, 1.0, 1.E-5, 0.1, 1.0
**
** LOADS
**
** Name: egentyngd   Type: Gravity
*Dload
, GRAV, 9.81, 0., -1., 0.
**
** OUTPUT REQUESTS
**
*Restart, write, frequency=0
**
** FIELD OUTPUT: F-Output-2
**
*Output, field, variable=all
**
** HISTORY OUTPUT: H-Output-1
**
*Output, history, variable=all
*End Step
*STEP, NAME="Variabel Riks", NLGEOM=YES, INC=150
*STATIC, RIKS
1.E-5, 1.0, 1.E-5, 0.01, 1.0
*Field,variable=1
** Use the actual Young's Modulus E = 10.8 GPa for imposed loads
Node-set-1, 2
Node-set-2, 2
....
Node-set-1035, 2
*DLOAD
```

```
Set-1, PY, -266387.4846
Set-2, PY, -267961.3362
....
*END STEP
```